Nanoanalytics for materials science

Edited by Thilo Glatzel

Imprint

Nanoanalytics for materials science

Thilo Glatzel[*1] and Tom Wirtz[*2]

Editorial

Address:
[1]Department of Physics, University of Basel, Klingelbergstrasse 82, 4056 Basel, Switzerland and [2]Advanced Instrumentation for Ion Nano-Analytics (AINA), MRT Department, Luxembourg Institute of Science and Technology (LIST), 41 rue du Brill, L-4422 Belvaux, Luxembourg

Email:
Thilo Glatzel[*] - thilo.glatzel@unibas.ch; Tom Wirtz[*] - tom.wirtz@list.lu

* Corresponding author

This article is part of the Thematic Series "Nanoanalytics for materials science".

Editor-in-Chief: T. Schimmel

With the progress in fabricating more energy efficient and sustainable devices, an increased need for advanced materials and processing techniques arises that becomes increasingly challenging and demands for new analysis techniques. In particular excellent spatial resolution together with high-sensitivity chemical information at the nanoscale are of utmost importance for future developments [1]. One of the possible approaches is based on bimodal or even multimodal nanoanalysis, which was increasingly developed during the last decade. Other important aspects that have to be considered are the impact of the applied measurement technique on the results, the time needed to get representative and repeatable results, and the possibility to apply the technique under relevant environmental conditions.

These nanoanalytical techniques need detailed understanding of the physical processes included in both the device structures and detection techniques. A typical setup includes a probe (such as tip, ion beam or electron beam), the condition of the sample and the interaction between them, which all need to be extensively investigated by simulations and modeling in order to obtain an in-depth and reliable understanding and accurate physical models. Furthermore, a reliable and easy way to extract a maximum of information out of the multimodal

datasets, efficient data visualization strategies, and methods for analysis, mining and modeling are of utmost importance.

This Thematic Series on "Nanoanalytics for materials science" groups six exciting articles around the aforementioned aspects of nanoanalytics, describing the development of both new instrumentation as well as new methodologies.

On the side of instrumental development, a ultra-high resolution multi-probe device based on tuning fork sensors for both nanoindentation and depth sensing is presented by Cinar and co-workers [2]. Furthermore, Fleming et al. present an in situ combination of atomic force microscopy (AFM) and secondary ion mass spectrometry (SIMS) [3]. By doing so, they obtain high-resolution 3D elemental/chemical maps. This approach delivers not only complementary information but furthermore allows for determining and minimizing artefacts occurring in standard SIMS 3D analysis, as for example disturbed height information induced by inhomogeneities of the sputter rates (caused by samples containing various materials, different phases or having a non-flat surface) and varying secondary ion extraction efficiencies due to local field distortions (caused by topography with high aspect ratios).

An ex situ multi-modal approach combining transmission electron microscopy (TEM) as well as X-ray and IR spectroscopies was successfully applied to investigate magnetite nanoparticles by Kalska-Szostka et al. [4]. TEM was also used in the work of Gutsch et al. who developed a novel energy-filtered transmission electron microscopy (EFTEM) approach using ultrathin TEM membranes [5]. With this method, they were able to accurately study the morphology of Si nanocrystal ensembles without the limitations imposed by standard cross sectional TEM investigations.

Advances in preparing high-performance probes for magnetic force microscopy (MFM), with a particular focus on controlling and tuning the tip stray field, are presented by Iglesias-Freire and co-workers [6]. Finally, Mirzaei and Kiani described the vibration behavior of carbon-nanotube-reinforced composite structures highlighting the importance but also the feasibility of theoretical approaches in complex nanoanalytical studies [7].

Finally, we want to express our thanks to all authors for contributing their excellent work to this Thematic Series. We are also very grateful to the reviewers for their support by examining the papers and providing helpful reports, and the efficient and professional support by the editorial and production team of the *Beilstein Journal of Nanotechnology*.

Thilo Glatzel and Tom Wirtz

Basel and Belvaux, September 2016

References

1. Wirtz, T.; Philipp, P.; Audinot, J.-N.; Dowsett, D.; Eswara, S. *Nanotechnology* **2015,** *26,* 434001. doi:10.1088/0957-4484/26/43/434001
2. Cinar, E.; Sahin, F.; Yablon, D. *Beilstein J. Nanotechnol.* **2015,** *6,* 2015–2027. doi:10.3762/bjnano.6.205
3. Fleming, Y.; Wirtz, T. *Beilstein J. Nanotechnol.* **2015,** *6,* 1091–1099. doi:10.3762/bjnano.6.110
4. Kalska-Szostko, B.; Wykowska, U.; Satula, D.; Nordblad, P. *Beilstein J. Nanotechnol.* **2015,** *6,* 1385–1396. doi:10.3762/bjnano.6.143
5. Gutsch, S.; Hiller, D.; Laube, J.; Zacharias, M.; Kübel, C. *Beilstein J. Nanotechnol.* **2015,** *6,* 964–970. doi:10.3762/bjnano.6.99
6. Iglesias-Freire, Ó.; Jaafar, M.; Berganza, E.; Asenjo, A. *Beilstein J. Nanotechnol.* **2016,** *7,* 1068–1074. doi:10.3762/bjnano.7.100
7. Mirzaei, M.; Kiani, Y. *Beilstein J. Nanotechnol.* **2016,** *7,* 511–523. doi:10.3762/bjnano.7.45

Observing the morphology of single-layered embedded silicon nanocrystals by using temperature-stable TEM membranes

Sebastian Gutsch[*1], Daniel Hiller[1], Jan Laube[1], Margit Zacharias[1] and Christian Kübel[2]

Full Research Paper

Address:
[1]IMTEK, Albert-Ludwigs-University of Freiburg, Georges-Köhler Allee 103, 79110 Freiburg, Germany and [2]Karlsruhe Nano and Micro Facility (KNMF) and Institute of Nanotechnology (INT), Karlsruhe Institute of Technology (KIT), Hermann-von-Helmholtz-Platz 1, 76344 Eggenstein-Leopoldshafen, Germany

Email:
Sebastian Gutsch[*] - sebastian.gutsch@imtek.de

* Corresponding author

Abstract

We use high-temperature-stable silicon nitride membranes to investigate single layers of silicon nanocrystal ensembles by energy filtered transmission electron microscopy. The silicon nanocrystals are prepared from the precipitation of a silicon-rich oxynitride layer sandwiched between two SiO_2 diffusion barriers and subjected to a high-temperature annealing. We find that such single layers are very sensitive to the annealing parameters and may lead to a significant loss of excess silicon. In addition, these ultrathin layers suffer from significant electron beam damage that needs to be minimized in order to image the pristine sample morphology. Finally we demonstrate how the silicon nanocrystal size distribution develops from a broad to a narrow log-normal distribution, when the initial precipitation layer thickness and stoichiometry are below a critical value.

Introduction

Si nanocrystals (Si NC) are interesting for applications in third generation photovoltaics [1,2], light emitting diodes [3,4], lasers [5], but are also envisioned to be used as non-volatile memories [6-10]. The optical and electrical properties of ensembles of Si NCs are strongly influenced by the structural properties such as size distribution, separation distance and density regardless of the application [11-13]. Moreover, there is compelling evidence of multiple exciton generation in adjacent Si NCs with almost ideal quantum efficiencies which is explained in terms of space-separated quantum cutting due to strong coupling between neighboring Si NCs [14-18]. However, clear structural insight on the Si NC size distribution, separation distance and shape is missing to date, largely due to the complexity of the measurement. The distribution of Si NC sizes is routinely obtained by conventional cross-section transmission electron microscopy (TEM) [19,20], but its evaluation is tedious and areal densities and Si NC position and distance to each other cannot be derived with reasonable confidence. Direct attempts

have been made to probe size and density of Si NCs by atomic force microscopy [21]. TEM tomography [22,23] and atomprobe tomography [24,25] were also applied, but these methods probe only a very small volume, may be affected by preparation artifacts and require highly sophisticated equipment, enormous computational effort and time. A faster and easier approach to measure the Si NC size, position and density is the use of in-plane energy-filtered TEM (EFTEM) as was demonstrated for Si NCs formed by low energy Si ion implantation [10,26], plasma-enhanced chemical vapor deposition (PE-CVD) [27] or evaporation [28] followed by a high temperature annealing. The bottleneck in such measurements is the low TEM plane view specimen preparation yield when ultrathin layers are concerned. We circumvent this issue in this work by using nanometer thin, free standing silicon nitride membranes to allow for plane view EFTEM analysis without further sample preparation. Thin layers of Si-rich silicon oxynitride (SRON) can be deposited directly on these membranes that also withstand the high temperature annealing that is needed to induce phase separation and crystallization of the Si NC layers. In contrast to the above mentioned ion implantation, deposition processes allow for sharp interfaces between two confining silicon oxide (SiO_2) layers. Here, we investigate ultrathin SRON layers by using plane view EFTEM and discuss possible pitfalls in both sample preparation and TEM imaging. Finally, we demonstrate how the thickness and stoichiometry of a SRON layer affects the Si NC size distribution, shape and areal density.

Experimental

We used 5 nm silicon nitride TEM support grids as a substrate (TEMwindows, SN100-A05Q33A). The layers were prepared by PE-CVD the details of which can be found elsewhere [29]. After layer deposition, the samples were postprocessed by high-temperature annealing. A list of all samples including the relevant processing parameters is available in Table 1. The layer stoichiometries were determined by X-ray photoelectron spec-

troscopy [29,30]. Please note that we sandwiched the SRON layer between two 2 nm SiO_2 films to mimic somewhat the SiO_2 barrier layer in our superlattice approach [19]. The SiO_2 film thickness is a trade-off between contrast quality during the EFTEM investigation and a reduction of the SiO surface loss during annealing [31] that is discussed later on in this paper in more detail. In fact, we do not observe significant Si surface loss when we use 10 nm thick embedding SiO_2 layers [32], but the plane view contrast to image Si nanoparticles is strongly reduced due to the largely overlapping plasmon loss peaks of Si and SiO_2 centered at 17 eV and 24 eV respectively. Please note that the deposition rates of all sublayers were determined in a separate preliminary experiment by using ellipsometry. The EFTEM has been carried out using an image aberration corrected FEI Titan 80-300 microscope operated at 300 kV, equipped with a Gatan 863 Tridiem Imaging Filter and a US1000 slow-scan CCD camera. EFTEM images were acquired with a 5 eV energy slit centered at an energy loss of 17 eV (i.e., the Si plasmon loss energy).
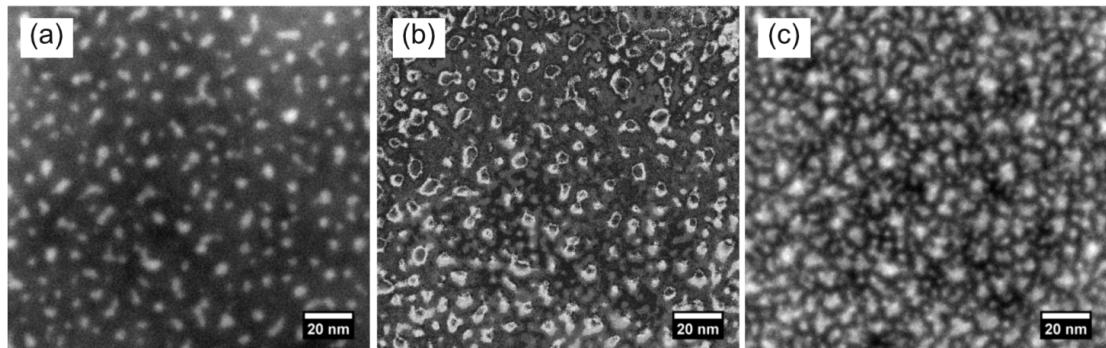
Results and Discussion
Electron irradiation damage

First of all, we focus on a more general observation which mainly concerns the thin film instability during the imaging process. In Figure 1a, a TEM micrograph of sample S1 is presented. In the energy-filtered imaging, the Si particles are clearly visible as white areas. The image has been obtained using low-dose conditions with a total dose of about 5.6 C/cm². In Figure 1c, the dose amounts to about 4.5×10^2 C/cm² in the same area. The particles have significantly grown and new particles appeared, which is clearly visualized in the XOR image of Figure 1b, where image changes are indicated by white. We therefore decided to investigate two plain SiO_2 films, a SiO_2 reference TEM membrane and a SiN membrane with PECVD SiO_2 on top (samples S2 and S3, cf. Table 1). As shown in Figure 2, the creation of Si particles also was observed to take place in pure SiO_2 and we estimated a threshold irradi-
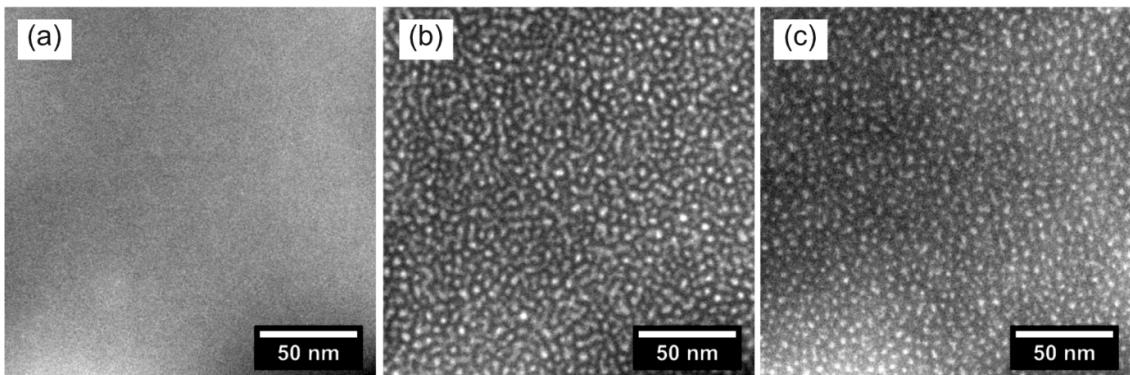
Table 1: List of TEM membrane samples fabricated within this work.

sample name	membrane type	active layer	annealing
S1	5 nm SiN	2 nm SiO_2/4.5 nm $SiO_{0.64}$/2 nm SiO_2	1150 °C, N_2, 1 h
S2	20 nm SiO_2	—	—
S3	5 nm SiN	10 nm SiO_2	1100 °C, N_2, 1 h
S4	5 nm SiN	2 nm SiO_2/10 nm $SiO_{0.93}$/2 nm SiO_2	1100 °C, Ar[a]
S5	5 nm SiN	2 nm SiO_2/10 nm $SiO_{0.93}$/2 nm SiO_2	1100 °C, N_2[a]
S6	5 nm SiN	2 nm SiO_2/4.5 nm $SiO_{0.93}$/2 nm SiO_2	1100 °C, N_2[a]
S7	5 nm SiN	2 nm SiO_2/3.5 nm $SiO_{0.93}$/2 nm SiO_2	1100 °C, N_2[a]
S8	5 nm SiN	2 nm SiO_2/3.5 nm $SiO_{0.85}$/2 nm SiO_2	1100 °C, N_2[a]
S9	5 nm SiN	2 nm SiO_2/3.5 nm $SiO_{0.64}$/2 nm SiO_2	1100 °C, N_2[a]

[a]annealing was carried in a ramp-up/ramp-down mode with no intentional temperature hold step (see main text for explanation).

Figure 1: EFTEM images of S1: (a) image in fresh area, (c) after about 10 min exposure to an intense electron beam and (b) XOR image of (a) and (c) highlighting the change between the two as denoted by white regions. Nanoparticles obviously grow and even new ones are created.


Figure 2: EFTEM images of references samples S2 and S3: (a) S2 irradiated with a low dose, (b) S2 irradiated with a high dose and (c) S3 irradiated with a high dose. After low dose irradiation no Si particles are observed (cf. panel (a)), whereas high doses lead to a dense formation of tiny Si nanoparticles (cf. panels (b) and (c)).

ation dose of about 16 C/cm². Please note that our calculated threshold dose is in close agreement with literature data [33]. The intense electron beam may cause the breaking of Si–O bonds accompanied by the creation of volatile O_2 molecules, which is supported by the observation of defect creation in SiO_2 after electron irradiation [34] and a SiO_2 thickness dependence on the hole drilling time when exposed to an intense electron probe [35]. Another possible explanation is certainly a preferential sputtering or knock-on of oxygen [36-38]. A common way to reduce the electron beam damage is to lower the operating voltage of the TEM. Hence, we reduced the operation voltage to 80 kV, but did not observe any significant differences in the beam irradiation damage. While the true beam damage mechanism is subject to further investigation, it can be concluded that it is important to take images below the threshold dose, when dielectric films containing Si NCs are investigated.

Silicon loss and out-diffusion during segregation annealing

Another issue that arises directly from inspection of Figure 1a is the low areal density of sample S1 of only 0.8×10^{12} NC/cm².

This is a reduction of more than 50% compared to the value of sample S5 treated with a much lower thermal budget (cf. Table 1 and below in Table 2). Lower Si excess concentrations and smaller SRON thicknesses resulted in even lower areal densities. The results suggest that the single Si NC layer is subject to a loss of excess Si during the annealing process. Oxidation of excess Si by some species in the annealing ambient is unlikely because of the highly purified inert gases used during the annealing process. This is further supported by a control experiment, in which we annealed an oxide free Si wafer under the same annealing conditions. An unintentional oxide growth below 1 nm SiO_2 thickness was estimated by ellipsometry. On the other hand, we need to consider Si diffusion towards the surface followed by a molecular desorption process [31]. The diffusion of Si in SiO_2 is known to be mediated by co-diffusion of SiO molecules and hence strongly depends on the nature of the Si/SiO_2 interface [39]. The diffusion length L_{Si} of Si can be calculated by $L_{Si} = 2\sqrt{D_{Si}t}$, where D_{Si} represents the diffusion constant of Si in SiO_2. Using the values from literature [39] for a 1 h annealing, L_{Si} is determined to be around 2.6 nm which is larger than the 2 nm capping SiO_2 even though the heating and

cooling ramps were not considered. Although the Si surface loss rate is not exactly known, Si out-diffusion and emanation may well explain the observed effects. The diffusion length can be reduced by shortening the annealing time and lowering the annealing temperature. Hence short furnace annealing processes with fast temperature ramps and a peak temperature of 1100 °C are used for all following samples.
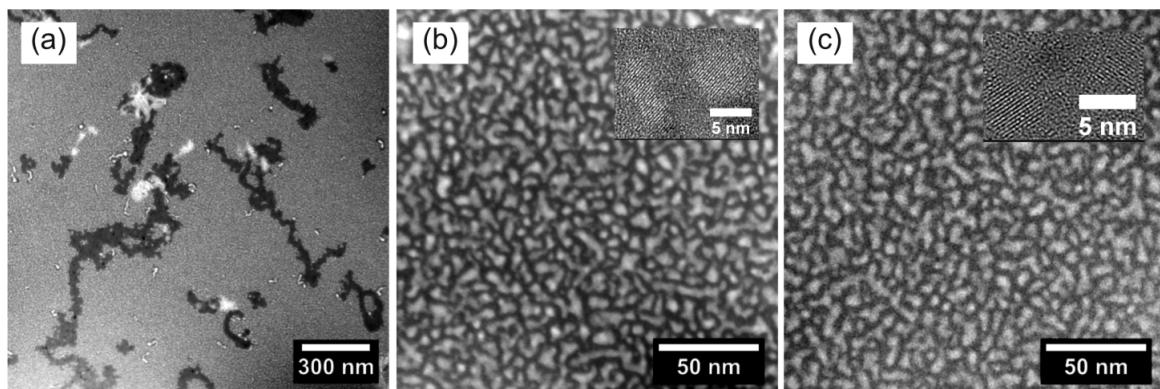
The role of annealing ambient

It is well known that N2 annealing is usually reducing interface defects and hence leads to higher photoluminescence intensities as compared to Ar annealing [40,41]. Therefore, 10 nm $SiO_{0.93}$ films were annealed in Ar and N_2 (samples S4 and S5) atmosphere and compared by plane-view EFTEM that is presented in Figure 3. As can be seen at lower magnification (Figure 3a), the Ar-annealed sample exhibits a high density of surface defects. It appears that part of the layer has been removed (darker regions). These surface damages are absent for the N_2-annealed sample, which is very homogeneous across the whole sample area. Similar effects have been reported for Ar-annealed SiO_2 thin films on Si and were ascribed to out-diffusion of SiO molecules [31]. Therefore, it can be concluded that annealing in N_2 hampers the Si out-diffusion. However, the undamaged microstructures (cf. Figure 3b and Figure 3c) are very similar for both annealings. From high resolution TEM (see insets of Figure 3b and Figure 3c) and electron diffraction, we found that both samples feature a high degree of crystallinity as is corrobated by detailed Raman studies [20,42]. However, the Si NC shape is not spherical at all. Due to the minimization of Gibbs free energy, a spherical shape is expected, which is limited by the possibility of atomic rearrangement. Since the phase separation is completed within a few seconds due to diffusion of oxygen [43], the nanoparticle growth and shaping can only be achieved through the diffusion of Si within SiO_2, which is extremely low at the used thermal budget. Longer and higher
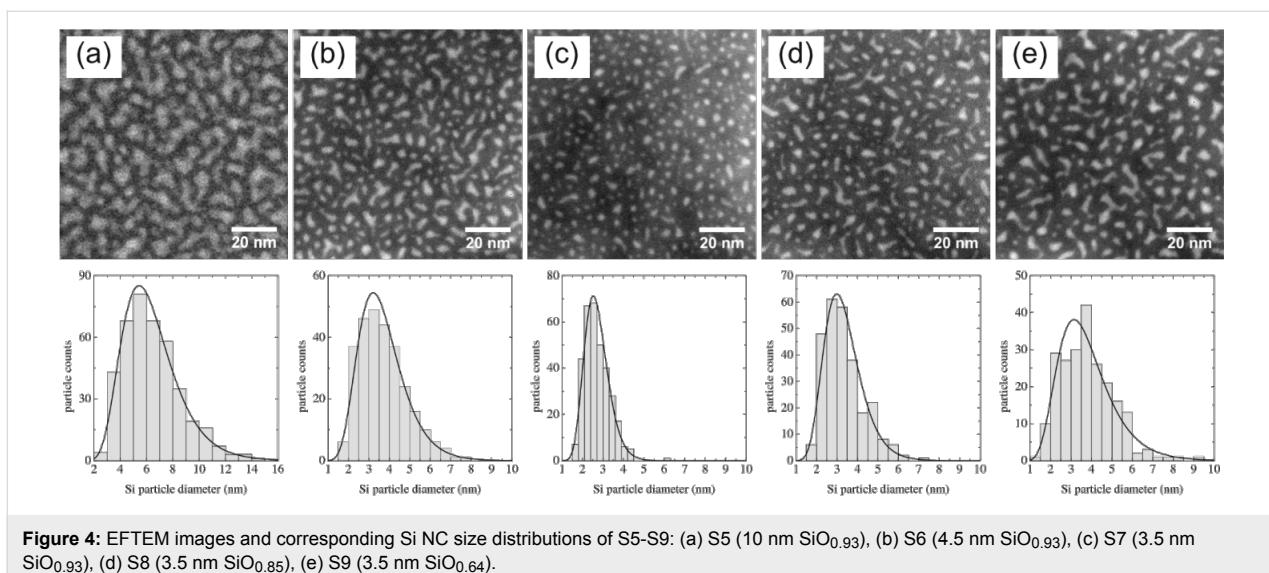
temperature annealings would certainly lead to larger amounts of spherical particles with a reduced density due to late-stage coarsening [27,44].

Silicon nanocrystal size distribution and areal density

Once the annealing conditions and TEM routines have been specified, it is straightforward to investigate the influence of the SRON layer thickness and stoichiometry on density, size and shape of the Si NCs. In Figure 4 a series of EFTEM images is presented for samples S5 to S9. We first consider Figure 4a–c in which the SRON thickness is reduced from 10 nm to 3.5 nm for a fixed layer stoichiometry of $SiO_{0.93}$. A transition from irregular and large towards spherical and smaller precipitates is clearly observed. Owing to the excellent contrast, the images can be evaluated by image processing software such as ImageJ [45] in order to analyze the particle distribution. The individual particle areas have been assigned to a circle of the same area which allows for the characterization of all particles through a single parameter. The diameter distributions are shown below the corresponding EFTEM images in Figure 4. All distributions can be fitted excellently by a log-normal distribution. The results strongly reflect the ability to control the Si NC size by geometrical one-dimensional confinement of the SRON layers. Furthermore, the influence of the SRON stoichiometry on Si nanoparticle formation is demonstrated in Figure 4c–e. Interestingly, increasing the Si excess exhibits a similar effect on the Si NC size and shape as the SRON thickness increase. The transition from clustering to spinodal-like decomposition [46-48] is obviously a sensitive function of the SRON thickness as well as of the stoichiometry. Due to the one dimensional geometrical confinement imposed by the SiO_2 barriers, the effective excess Si available for particle formation is reduced and hence spinodal growth sets in at higher SRON thicknesses [49]. As the Si excess in the SRON layer is increased, the SRON thickness


Figure 3: EFTEM images of S4 (a,b) and S5 (c): (a) overview image of S4 illustrating severe sample damage caused by Ar annealing, (b,c) smaller area to show that the morphology in the undamaged regions are fairly similar for both Ar and N_2 annealing.

Figure 4: EFTEM images and corresponding Si NC size distributions of S5–S9: (a) S5 (10 nm $SiO_{0.93}$), (b) S6 (4.5 nm $SiO_{0.93}$), (c) S7 (3.5 nm $SiO_{0.93}$), (d) S8 (3.5 nm $SiO_{0.85}$), (e) S9 (3.5 nm $SiO_{0.64}$).

threshold for spinodal decomposition is shifted to smaller values [49,50], a fact that is experimentally demonstrated in Figure 4.

The EFTEM studies are summarized in Table 2, where the maximum of the diameter distribution as well the particle areal density A_{NC} and the particle area fill fraction are given. Please note that such detailed information as provided by the plane-view method here, is not available in cross-section TEM imaging [19,20,29]. The areal particle density is increased and the Si NC diameter is decreased, when the SRON layer thickness is reduced as expected. However, increasing the Si excess reduces the areal density. The idea of the superlattice approach is to control the Si NC size and density independently by variation of the SRON thickness or stoichiometry respectively [19]. The results presented here are in contrast to the assumptions of this idealized superlattice approach. The reason is apparently that at high Si excess concentrations, larger Si regions form as is indicated by the increased average Si NC diameter. Finally, it must be noted that a certain amount of Si still appears to be lost by Si out-diffusion during the optimized annealing that effectively decreases the particle size.

Conclusion

In conclusion, we have demonstrated an approach using ultra-thin TEM membranes and EFTEM imaging as a very versatile tool to study the morphology of Si NC ensembles in contrast to the limitation imposed by cross sectional TEM investigations [19,20,29]. We proved that low electron doses have to be used in order to image the real Si NC structure since higher irradiation doses lead to undesired growth and expansion of the SiNCs. Furthermore, we have shown that for these samples, large surface damage occurs when annealing in Ar atmosphere, whereas this damage is minimized in N_2 atmosphere. SiNC size distributions and areal densities were measured for a variety of sample parameters such as initial SRON thickness and stoichiometry. It is demonstrated that SiNC size and density cannot be controlled individually by changing the thickness or stoichiometry of the SRON layer. On the one hand the average SiNC size is controllable by the SRON thickness, on the other hand an increase of the Si excess concentration results in a larger SiNC formation with a reduced areal density. Please note that the observed trends are certainly representative for the given sample parameters, but may still deviate from the individual layer structure in a superlattice.

Table 2: Extracted parameters from the EFTEM analysis, d_{NC} indicates the maximum of the log-normal distribution fit, whereas A_{NC} is the Si NC areal density.

sample name	SRON layer	d_{NC} (nm)	A_{NC} (NC/cm²)	area fill fraction
S5	10 nm $SiO_{0.93}$	5.4	$(1.13 \pm 0.02) \times 10^{12}$	40.8%
S6	4.5 nm $SiO_{0.93}$	3.2	$(2.43 \pm 0.05) \times 10^{12}$	28.8%
S7	3.5 nm $SiO_{0.93}$	2.6	$(2.88 \pm 0.06) \times 10^{12}$	17.7%
S8	3.5 nm $SiO_{0.85}$	3.0	$(2.32 \pm 0.05) \times 10^{12}$	22.3%
S9	3.5 nm $SiO_{0.64}$	3.2	$(1.95 \pm 0.04) \times 10^{12}$	24.6%

Acknowledgements

References

1. Conibeer, G.; Green, M.; Corkish, R.; Cho, Y.; Cho, E.-C.; Jiang, C.-W.; Fangsuwannarak, T.; Pink, E.; Huang, Y.; Puzzer, T.; Trupke, T.; Richards, B.; Shalav, A.; Lin, K.-l. *Thin Solid Films* **2006**, *511–512,* 654–662. doi:10.1016/j.tsf.2005.12.119
2. Perez-Wurfl, I.; Hao, X.; Gentle, A.; Kim, D.-H.; Conibeer, G.; Green, M. A. *Appl. Phys. Lett.* **2009**, *95,* 153506. doi:10.1063/1.3240882
3. Marconi, A.; Anopchenko, A.; Wang, M.; Pucker, G.; Bellutti, P.; Pavesi, L. *Appl. Phys. Lett.* **2009**, *94,* 221110. doi:10.1063/1.3147164
4. Walters, R. J.; Bourianoff, G. I.; Atwater, H. A. *Nat. Mater.* **2005**, *4,* 143–146. doi:10.1038/nmat1307
5. Pavesi, L.; Dal Negro, L.; Mazzoleni, C.; Franzò, G.; Priolo, F. *Nature* **2000**, *408,* 440–444. doi:10.1038/35044012
6. Tiwari, S.; Rana, F.; Hanafi, H.; Hartstein, A.; Crabbé, E. F.; Chan, K. *Appl. Phys. Lett.* **1996**, *68,* 1377–1379. doi:10.1063/1.116085
7. Walters, R. J.; Kik, P. G.; Casperson, J. D.; Atwater, H. A.; Lindstedt, R.; Giorgi, M.; Bourianoff, G. *Appl. Phys. Lett.* **2004**, *85,* 2622–2624. doi:10.1063/1.1795364
8. Lu, T. Z.; Alexe, M.; Scholz, R.; Talalaev, V.; Zhang, R. J.; Zacharias, M. *J. Appl. Phys.* **2006**, *100,* 014310. doi:10.1063/1.2214300
9. Lu, T. Z.; Alexe, M.; Scholz, R.; Talelaev, V.; Zacharias, M. *Appl. Phys. Lett.* **2005**, *87,* 202110. doi:10.1063/1.2132083
10. Müller, T.; Heinig, K.-H.; Möller, W.; Bonafos, C.; Coffin, H.; Cherkashin, N.; Assayag, G. B.; Schamm, S.; Zanchi, G.; Claverie, A.; Tencé, M.; Colliex, C. *Appl. Phys. Lett.* **2004**, *85,* 2373–2375. doi:10.1063/1.1794856
11. Hartel, A. M.; Gutsch, S.; Hiller, D.; Zacharias, M. *Phys. Rev. B* **2012**, *85,* 165306. doi:10.1103/PhysRevB.85.165306
12. Gutsch, S.; Laube, J.; Hartel, A. M.; Hiller, D.; Zakharov, N.; Werner, P.; Zacharias, M. *J. Appl. Phys.* **2013**, *113,* 133703. doi:10.1063/1.4798395
13. López-Vidrier, J.; Berencén, Y.; Hernández, S.; Blázquez, O.; Gutsch, S.; Laube, J.; Hiller, D.; Löper, P.; Schnabel, M.; Janz, S.; Zacharias, M.; Garrido, B. *J. Appl. Phys.* **2013**, *114,* 163701. doi:10.1063/1.4826898
14. Timmerman, D.; Izeddin, I.; Stallinga, P.; Yassievich, I. N.; Gregorkiewicz, T. *Nat. Photonics* **2008**, *2,* 105–109. doi:10.1038/nphoton.2007.279
15. Timmerman, D.; Valenta, J.; Dohnalova, K.; de Boer, W. D. A. M.; Gregorkiewicz, T. *Nat. Nanotechnol.* **2011**, *6,* 710–713. doi:10.1038/nnano.2011.167
16. Trinh, M. T.; Limpens, R.; de Boer, W. D. A. M.; Schins, J. M.; Siebbeles, L. D. A.; Gregorkiewicz, T. *Nat. Photonics* **2012**, *6,* 316–321. doi:10.1038/nphoton.2012.36
17. Govoni, M.; Marri, I.; Ossicini, S. *Nat. Photonics* **2012**, *6,* 672–679. doi:10.1038/nphoton.2012.206
18. Valenta, J.; Greben, M.; Gutsch, S.; Hiller, D.; Zacharias, M. *Appl. Phys. Lett.* **2014**, *105,* 243107. doi:10.1063/1.4904472
19. Zacharias, M.; Heitmann, J.; Scholz, R.; Kahler, U.; Schmidt, M.; Bläsing, J. *Appl. Phys. Lett.* **2002**, *80,* 661–663. doi:10.1063/1.1433906
20. López-Vidrier, J.; Hernández, S.; Hartel, A. M.; Hiller, D.; Gutsch, S.; Löper, P.; López-Conesa, L.; Estradé, S.; Peiró, F.; Zacharias, M.; Garrido, B. *Energy Procedia* **2011**, *10,* 43–48. doi:10.1016/j.egypro.2011.10.150
21. Feng, T.; Yu, H.; Dicken, M.; Heath, J. R.; Atwater, H. A. *Appl. Phys. Lett.* **2005**, *86,* 033103. doi:10.1063/1.1852078
22. Yurtsever, A.; Weyland, M.; Muller, D. A. *Appl. Phys. Lett.* **2006**, *89,* 151920. doi:10.1063/1.2360906
23. Kourkoutis, L. F.; Hao, X.; Huang, S.; Puthen-Veettil, B.; Conibeer, G.; Green, M. A.; Perez-Wurfl, I. *Nanoscale* **2013**, *5,* 7499–7504. doi:10.1039/C3NR01998E
24. Talbot, E.; Lardé, R.; Gourbilleau, F.; Dufour, C.; Pareige, P. *Europhys. Lett.* **2009**, *87,* 26004. doi:10.1209/0295-5075/87/26004
25. Gnaser, H.; Gutsch, S.; Wahl, M.; Schiller, R.; Kopnarski, M.; Hiller, D.; Zacharias, M. *J. Appl. Phys.* **2014**, *115,* 034304. doi:10.1063/1.4862174
26. Schamm, S.; Bonafos, C.; Coffin, H.; Cherkashin, N.; Carrada, M.; Assayag, G. B.; Claverie, A.; Tencé, M.; Colliex, C. *Ultramicroscopy* **2008**, *108,* 346–357. doi:10.1016/j.ultramic.2007.05.008
27. Boninelli, S.; Iacona, F.; Franzó, G.; Bongiorno, C.; Spinella, C.; Priolo, F. *J. Phys.: Condens. Matter* **2007**, *19,* 225003. doi:10.1088/0953-8984/19/22/225003
28. Hernández, S.; Miska, P.; Grün, M.; Estradé, S.; Peiró, F.; Garrido, B.; Vergnat, M.; Pellegrino, P. *J. Appl. Phys.* **2013**, *114,* 233101. doi:10.1063/1.4847536
29. Hartel, A. M.; Hiller, D.; Gutsch, S.; Löper, P.; Estradé, S.; Peiró, F.; Garrido, B.; Zacharias, M. *Thin Solid Films* **2011**, *520,* 121–125. doi:10.1016/j.tsf.2011.06.084
30. Laube, J.; Gutsch, S.; Hiller, D.; Bruns, M.; Kübel, C.; Weiss, C.; Zacharias, M. *J. Appl. Phys.* **2014**, *116,* 223501. doi:10.1063/1.4904053
31. Beyer, V.; von Borany, J.; Heinig, K.-H. *J. Appl. Phys.* **2007**, *101,* 053516. doi:10.1063/1.2436834
32. Hartel, A. M.; Gutsch, S.; Hiller, D.; Kübel, C.; Zakharov, N.; Werner, P.; Zacharias, M. *Appl. Phys. Lett.* **2012**, *101,* 193103. doi:10.1063/1.4766284
33. Chen, G. S.; Boothroyd, C. B.; Humphreys, C. J. *Philos. Mag. A* **1998**, *78,* 491–506. doi:10.1080/01418619808241915
34. Pfeffer, R. L. *J. Appl. Phys.* **1985**, *57,* 5176–5180. doi:10.1063/1.335252
35. Chen, G. S.; Humphreys, C. J. *J. Appl. Phys.* **1999**, *85,* 148–152. doi:10.1063/1.369461
36. Egerton, R. F.; Li, P.; Malac, M. *Micron* **2004**, *35,* 399–409. doi:10.1016/j.micron.2004.02.003
37. Egerton, R. F.; McLeod, R.; Wang, F.; Malac, M. *Ultramicroscopy* **2010**, *110,* 991–997. doi:10.1016/j.ultramic.2009.11.003
38. Egerton, R. F.; Wang, F.; Crozier, P. A. *Microsc. Microanal.* **2006**, *12,* 65–71. doi:10.1017/S1431927606060065
39. Uematsu, M.; Kageshima, H.; Takahashi, Y.; Fukatsu, S.; Itoh, K. M.; Shiraishi, K.; Gösele, U. *Appl. Phys. Lett.* **2004**, *84,* 876–878. doi:10.1063/1.1644623
40. Hiller, D.; Goetze, S.; Munnik, F.; Jivanescu, M.; Gerlach, J. W.; Vogt, J.; Pippel, E.; Zakharov, N.; Stesmans, A.; Zacharias, M. *Phys. Rev. B* **2010**, *82,* 195401. doi:10.1103/PhysRevB.82.195401
41. Wilkinson, A. R.; Elliman, R. G. *J. Appl. Phys.* **2004**, *96,* 4018–4020. doi:10.1063/1.1789265
42. Hernández, S.; López-Vidrier, J.; López-Conesa, L.; Hiller, D.; Gutsch, S.; Ibáñez, J.; Estradé, S.; Peiró, F.; Zacharias, M.; Garrido, B. *J. Appl. Phys.* **2014**, *115,* 203504. doi:10.1063/1.4878175

43. Sarikov, A.; Litovchenko, V.; Lisovskyy, I.; Maidanchuk, I.; Zlobin, S.
    Appl. Phys. Lett. **2007,** *91,* 133109. doi:10.1063/1.2790814
44. Rogers, T. M.; Desai, R. C. *Phys. Rev. B* **1989,** *39,* 11956–11964.
    doi:10.1103/PhysRevB.39.11956
45. ImageJ. http://imagej.nih.gov/ij/ (accessed March 9, 2015).
46. Cahn, J. W. *J. Chem. Phys.* **1965,** *42,* 93–99. doi:10.1063/1.1695731
47. Abyzov, A. S.; Schmelzer, J. W. P. *J. Chem. Phys.* **2007,** *127,* 114504.
    doi:10.1063/1.2774989
48. Brunini, V. E.; Schuh, C. A.; Carter, W. C. *Phys. Rev. E* **2011,** *83,*
    021119. doi:10.1103/PhysRevE.83.021119
49. Binder, K.; Puri, S.; Das, S. K.; Horbach, J. *J. Stat. Phys.* **2010,** *138,*
    51–84. doi:10.1007/s10955-010-9924-9
50. Müller, T.; Heinig, K.-H.; Möller, W. *Appl. Phys. Lett.* **2002,** *81,*
    3049–3051. doi:10.1063/1.1512952

High sensitivity and high resolution element 3D analysis by a combined SIMS–SPM instrument

Yves Fleming[*] and Tom Wirtz

Abstract

Using the recently developed SIMS–SPM prototype, secondary ion mass spectrometry (SIMS) data was combined with topographical data from the scanning probe microscopy (SPM) module for five test structures in order to obtain accurate chemical 3D maps: a polystyrene/polyvinylpyrrolidone (PS/PVP) polymer blend, a nickel-based super-alloy, a titanium carbonitride-based cermet, a reticle test structure and $Mg(OH)_2$ nanoclusters incorporated inside a polymer matrix. The examples illustrate the potential of this combined approach to track and eliminate artefacts related to inhomogeneities of the sputter rates (caused by samples containing various materials, different phases or having a non-flat surface) and inhomogeneities of the secondary ion extraction efficiencies due to local field distortions (caused by topography with high aspect ratios). In this respect, this paper presents the measured relative sputter rates between PVP and PS as well as in between the different phases of the TiCN cermet.

Introduction

With the progress of miniaturisation, driven by future needs in various fields in materials and life sciences, the 3D analysis of devices and material structures becomes increasingly challenging. As a consequence, the interest for performing bimodal or even multimodal nano-analysis has increased during the last decade [1]. In particular, nano-analytical techniques and instru-ments providing both excellent spatial resolution and high-sensitivity chemical information are of utmost importance for investigations at the nanoscale. Secondary ion mass spectrometry (SIMS) is a method of choice for high sensitivity analysis, including isotopic ratio measurements [2,3]. State-of-the-art SIMS imaging instruments can provide chemical 2D and

3D maps with a lateral resolution of around 50 nm [4,5]. However, several important artefacts result from the fact that conventional 3D image reconstructions do not consider the sample surface topography, because these protocols and the applied software assume a flat sample surface as well as a cube-like analysed volume [6]. In reality, samples exhibit a surface roughness, which is also changed during the ion bombardment, because parameters such as crystal orientation and the local angle of incidence of the ion beam influence local sputter yields [6]. In case the sample is constituted of different materials, the situation is worsened due to preferential sputtering phenomena. As a consequence, the produced 3D images are affected by uncertainties on the depth scale, which are more or less important. This then causes distortions in the reconstructed 3D maps of the sample. To achieve actual high-resolution SIMS 3D analyses without risking the artefacts mentioned above, we developed a scanning probe microscopy (SPM) module that we integrated into the Cameca NanoSIMS50 [6,7]. As the environment conditions are the same (i.e., the vacuum level does not change), this in situ combination of SIMS and SPM avoids artefacts such as topography changes due to surface diffusion and the interaction of the sample with reactive species used as primary ions in SIMS [8], which occur when an ex situ combination between these same techniques is used.

The aim of this paper is to illustrate the analytical potential of the combined SIMS–SPM approach by presenting several applications in the field of materials science.

Experimental

The integrated SIMS–SPM instrument based on a Cameca NanoSIMS 50 is presented in detail elsewhere [6,7]. The sample was sputtered with a Cs^+ primary ion beam at 16 keV impact energy, normal incidence and sample currents between 1.4 and 2.5 pA. The raster frame was set to 256 × 256 pixels. Depending on the analysis, the dwell time per pixel ranged from 5 to 10 ms/pixel.

The SPM module inside the SIMS instrument was used to perform atomic force microscopy (AFM) in non-contact mode also called nc-AFM [9]. When scanning the topography, an area four times larger than the SIMS raster image was scanned with 512 × 512 pixels, inclosing the sputtered area as well as the area surrounding the crater, such that a full 3D correlated image can be compiled. For performing the AFM measurements, typical Si tips with a backside reflex coating were used (Nanosensors PPP-NCLR, resonance frequency of 190 kHz, $C = 48$ N/m). One AFM acquisition took between 40 and 60 min. Using this mode under vacuum conditions retraces the sample topography accurately as the thin water film, which is present on the sample surface ex situ [10,11], has evaporated.
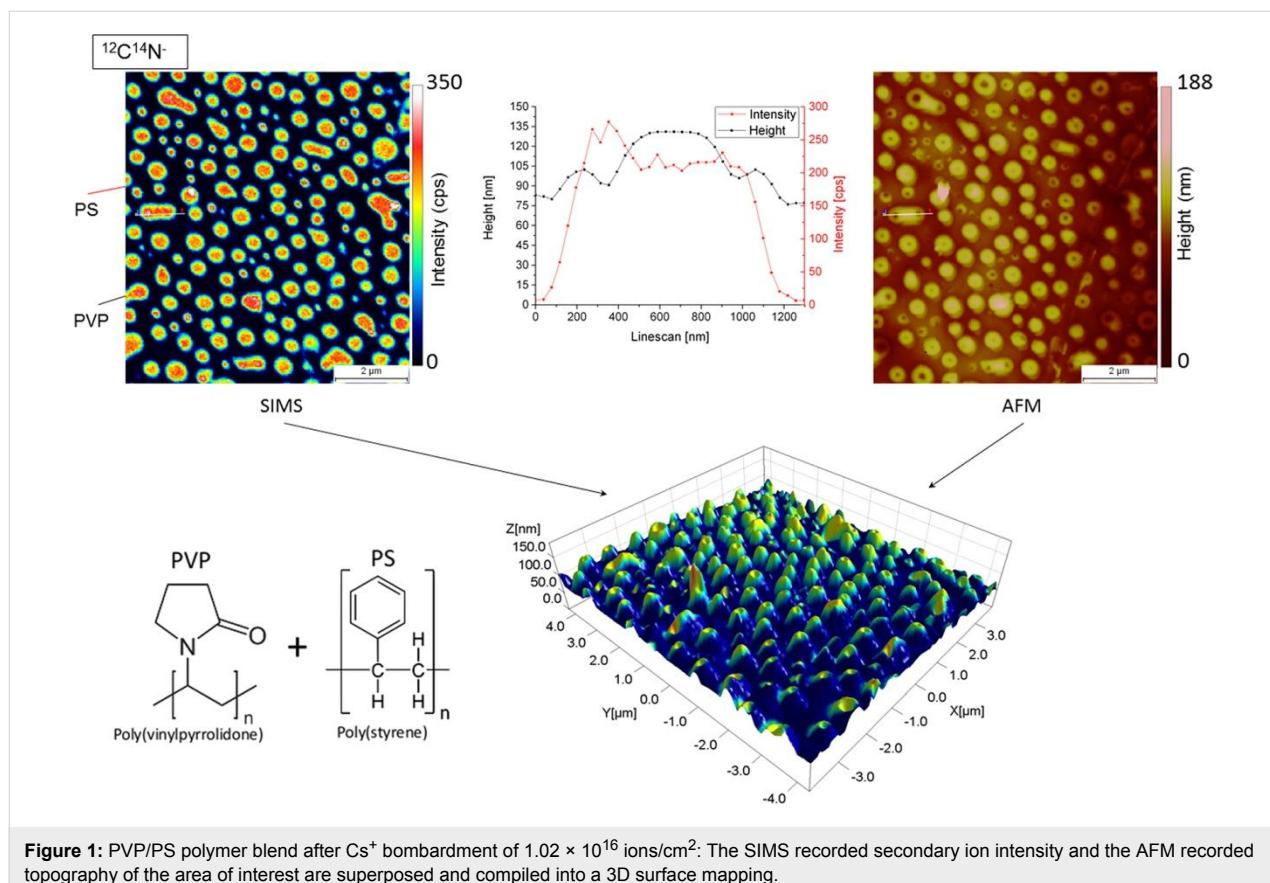
The processing of the SIMS and AFM data was performed with the in-house developed software SARINA [12]. This software allows for the accurate superposition of SIMS and AFM data based on mostly four reference points per mapping taking into account distortions in between the various AFM images and the correlation to the respective SIMS raster scans. For the 3D reconstructed volume, the recorded topographies are taken as reference maps for linearly extrapolating the z-position of each of the intermittent SIMS recorded voxels. SARINA was developed as a plugin for the ImageJ software [13]. The drift correction of the different recorded SIMS stacks were performed using the OpenMIMS software [14], which is widely used in the SIMS field. The 3D SIMS-AFM surface reconstructions are visualised using the SPIP™ software by Image Metrology [15], the ParaView software tool [16] as well as the MayaVI 2 software tool [17].

Results and Discussion
PS/PVP polymer blend

An annealed polystyrene (PS)/polyvinylpyrrolidone (PVP) polymer blend was prepared using a 75:25 (wt %) ratio of PS/PVP homopolymers. The homopolymers of PS with molecular mass $M_w = 350{,}000$ ($M_w/M_n = 2.05$) and PVP with molecular mass $M_n = 40{,}000$ ($M_w/M_n = 1.03$) were obtained from Sigma-Aldrich. Both polymers were diluted in chloroform. The polymer blend with a concentration of 5 mg/mL was spin-cast onto a cleaned silicon(111) wafer. The parameters for the spin-casting were 10,000 rpm/s spinning acceleration and 3000 rpm spinning speed for a time period of 60 s. The film thickness measured by AFM was found to be 150–200 nm. The film blends were subsequently annealed above the glass transition temperature of PS. They were heated up to 140 ± 5 °C and kept at this temperature in vacuum for a time period of 6 h. After this thermal treatment, the samples were allowed to cool down slowly to room temperature.

Figure 1 shows a standard 2D SIMS image, an AFM image, the combined 3D SIMS–AFM image of the PS/PVP sample and a linescan presenting the local sample surface topography of PVP as well as the corresponding CN^- secondary ion signal. Because PVP contains nitrogen (in contrast to PS) its spatial distribution can be easily imaged in SIMS by tracking the CN^- signal. The secondary ion signal corresponding to the CN^- cluster is much more intense than the signal of monatomic nitrogen. The obtained 3D map shows that the two polymer phases are well separated and that the sample under investigation is far from being flat. Prior to Cs^+ bombardment, the initial topography of the sample surface shows domes of PVP in a sea of PS. After Cs^+ sputtering, this initial topography flattens more and more due to preferential sputtering (not shown). From topography measurements before and after SIMS analysis, it was found that

Figure 1: PVP/PS polymer blend after Cs$^+$ bombardment of 1.02×10^{16} ions/cm^2: The SIMS recorded secondary ion intensity and the AFM recorded topography of the area of interest are superposed and compiled into a 3D surface mapping.

the erosion rate of PVP is considerably higher than that of PS. A calculation based on the combined SIMS–AFM map leads to a sputter yield of PVP that is 3.5 times higher than the one of PS. Considering the linescan plot, it can be noticed that the secondary ion signal originating from the PVP dome is not uniform. In fact, the signal intensity is slightly increased at the position where a dip is present on the PVP dome, which is most likely due to variations of the sputtering yield with the local angle of incidence.
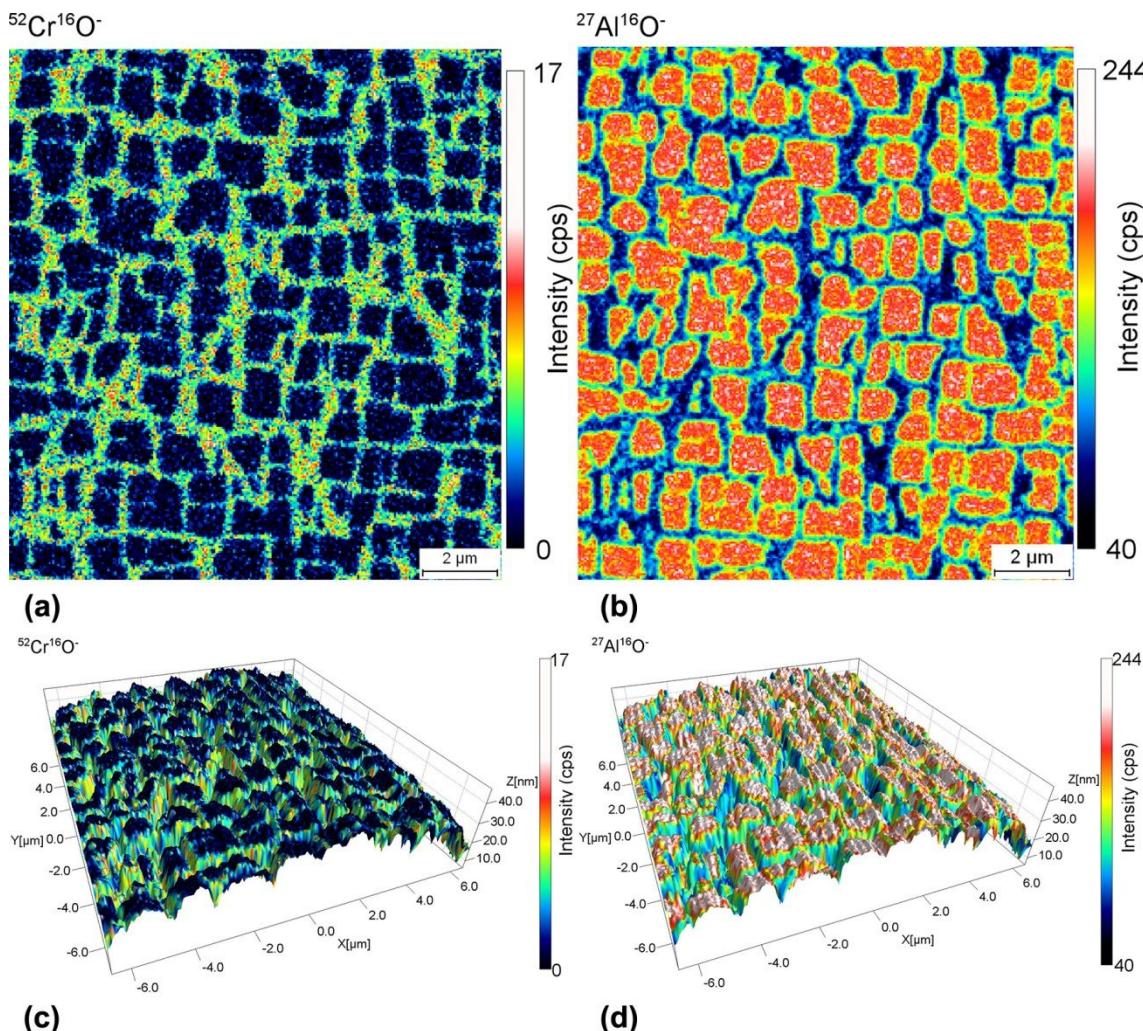
Nickel-based super-alloy

Differential sputtering can also be observed when analysing nickel-based super-alloys, which are used in aerospace industry due to their high robustness and resistivity even at high temperatures [18]. The different domains inside these alloys form during the annealing step [19]. Figure 2a and Figure 2b showing the 2D SIMS images obtained on this alloy highlight that a γ′-Ni$_3$Al precipitate phase is included inside the γ matrix. Figure 2c and Figure 2d show the overlay between the AFM and the SIMS mapping after sputtering a 15×15 μm^2 area for 16 h. Given that the initial sample surface was flat (root mean squared roughness of 1.1 nm), it can be noticed that the aluminium-containing γ′ phase sputters much more slowly than the chromium-containing areas. The ^{27}Al^{16}O$^-$ secondary ion

signal presents a dynamics of a factor of six between inside the γ′ phase (244 cps) and outside the γ′ phase (40 cps). The secondary ion signal does not drop down to zero, as some ^{27}Al^{16}O$^-$ ions that left the steep slopes created due to differential sputtering, are captured with an apparent pixel position outside the γ′ precipitate phase. This is a consequence of significant field inhomogeneities as a result of distortion of the local electric field arising from the surface topography. As already stated in [20], both the primary beam and the trajectories of secondary ions are perturbed by these field inhomogeneities. As a result, several artefacts, including shifts in apparent pixel position and changes in intensity, are possible. Figure 2c further shows that the ^{52}Cr^{16}O$^-$ secondary ion signal also seems to originate from the grain boundary walls of the γ′ precipitate phase. As we know from literature that ^{52}Cr is not present in the γ′ phase [19], a fraction of the ^{52}Cr^{16}O$^-$ ions originating from the faster sputtering γ matrix are first deposited at the boundary wall of the Ni$_3$Al precipitate phase before finally being re-sputtered and extracted by the secondary optics of the mass spectrometer.

Titanium carbonitride-based cermet
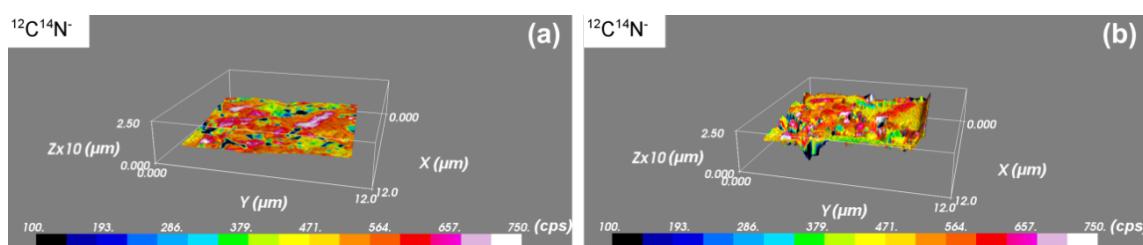
The titanium carbonitride-based cermet consists of Ti(C,N) grains with a cobalt binder percolating the ceramic grains [21].

**Figure 2:** $^{52}Cr^{16}O^-$ (a) and $^{27}Al^{16}O^-$ (b) secondary ion intensity recorded by the NanoSIMS instrument during the analysis of nickel-based super-alloy. The corresponding 3D SIMS-SPM reconstructions nicely show the correlations between the chemical composition and the topography (c) and (d).

Figure 3 shows two snapshots of a Ti(C,N) sample analysed by combined AFM and SIMS. From Figure 3a, we can see that the surface of the analysed area of interest is initially flat (root mean squared roughness of 5.1 nm). After sputtering for 9 h with the Cs^+ beam in SIMS mode, the sample holder was flipped into AFM mode again and a topography image was recorded (Figure 3b). From the combined SIMS–AFM image reconstruction, we determined that the phase containing the Co


Figure 3: Snapshot of SIMS-SPM reconstructed surface before (a) and during (b) SIMS analysis performed on Ti(C,N). The colour scale represents the $^{12}C^{14}N^-$ secondary ion intensity recorded by SIMS. The carbon containing phase sputters more slowly than the phase comprising the Co binder.

binder is sputtered at a rate of 0.28 nm·μm^2·pA^{-1}·s^{-1}, compared to a sputtering rate of 0.10 nm·μm^2·pA^{-1}·s^{-1} of the Ti domains. Thus, the Co binder material is sputtered 2.8 times faster than the Ti domains. The analysis was performed with a 1.4 pA Cs$^+$ primary beam.
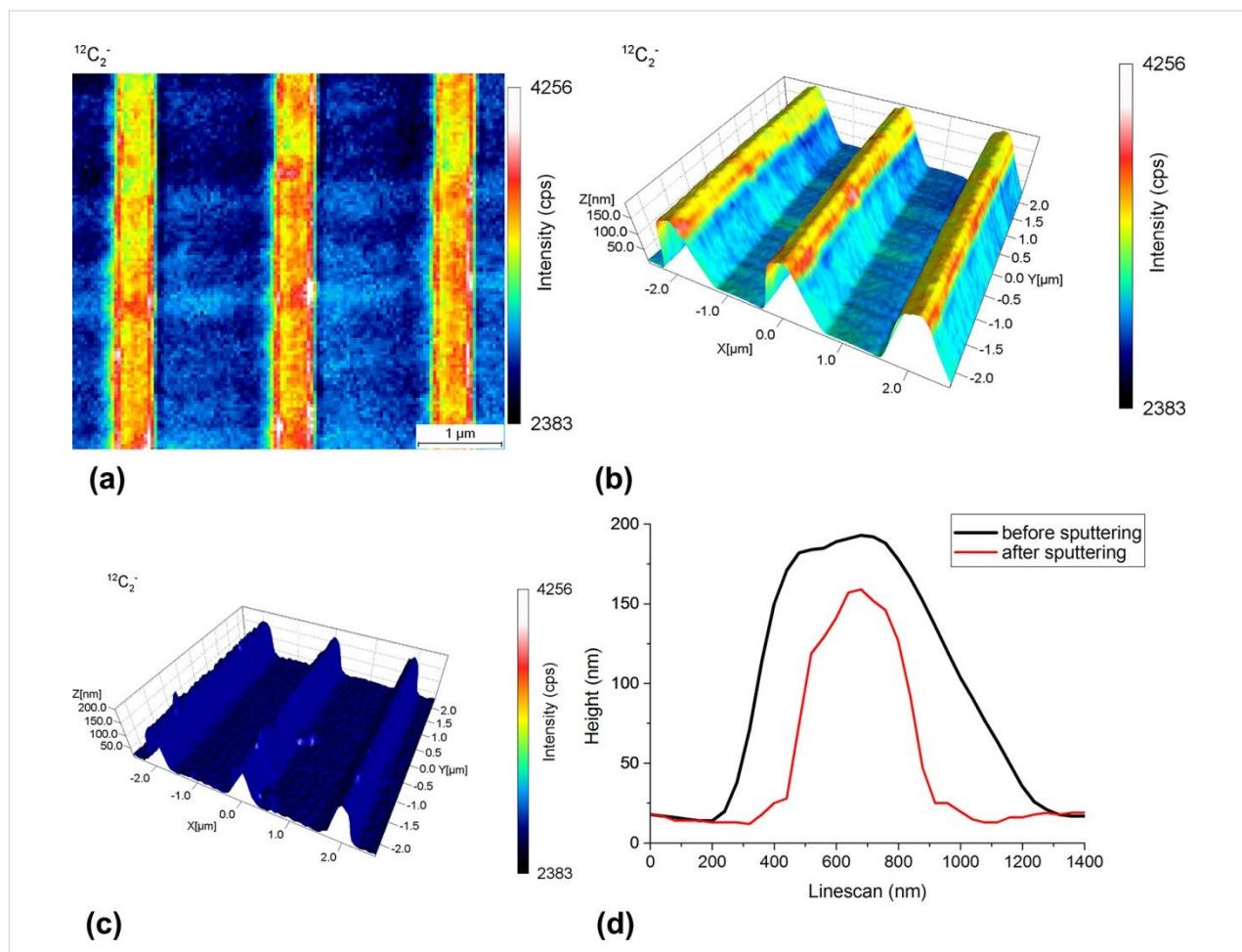
A video animation showing the differential sputtering of this sample slice by slice can be found in Supporting Information File 1. In this animation, the surface of the grains is taken as a reference surface. From the animation, it can be noticed that the surface roughness of the grains changes in a less pronounced way than the surface roughness at the zones corresponding to the Co binder.

EUV reticle test structures

In the field of lithography, various test structures that mimic large extreme ultra violet (EUV) reticules are commonly used.

For manufacturing the structures used in this example, a TaN layer was grown through atomic layer deposition (ALD) on a Si wafer. Subsequently, using e-beam patterning the trenches were etched into the TaN layer. After processing, the test structures were deliberately contaminated for test purposes with e-beam grown carbon, as described in [22].

In Figure 4a, a SIMS image of the TaN reticule sample is shown. Here, it can be noticed that the secondary ion intensity of $^{12}C_2^-$ varies regularly although a uniform capping layer of 10 nm was deposited on top of the sample surface. The variation of the $^{12}C_2^-$ signal amounts to a factor of 1.67 between the different observed stripes. Scanning the region of interest by AFM and combining both the SIMS and the AFM data, it becomes apparent that the increased ion intensity signal is due to the fact that the analysed sample is not flat. In fact, these topographical effects are due to the curvature of the electrical

Figure 4: Chemical image showing the $^{12}C_2^-$ secondary ion intensity recorded from the TaN reticule with a 10 nm carbon capping layer (a). 3D SIMS–SPM reconstruction combining the chemical information as well as the topographical information after a dose of 2.4 × 10^{16} ions/cm^2 (b) and after a dose of 1.2 × 10^{17} ions/cm^2 (c). AFM profiles before sputtering and after sputtering with a dose of 1.2 × 10^{17} ions/cm^2. As the trench was sputtered as well, it was preferred to plot the trench surface before and after sputtering to the same height. In this way, the change of the ridge shape is shown more clearly (d).

field on the sample surface, resulting in a reduced extraction efficiency of the secondary ions from the trenches. With the help of the AFM topography image, recorded at the exact spot of the SIMS analysis, this SIMS artefact can be explained and thus help the analyst with the interpretation of the SIMS analysis results. Looking more carefully at the results obtained, it can be noticed that the $^{12}C_2^-$ signal falls off very sharply at the ridge edges. This sharp drop in secondary ion intensity is somewhat astonishing considering that the carbon concentration was deposited homogeneously over the sample surface. In that specific case, one would expect that the change in signal would be more gradual. Hence, the conclusion must be that more carbon was deposited on the ridge than inside the trench. The presence of carbon inside the trench can be confirmed as the originating ion signal is about 2400 cps whereas after SIMS analysis this signal has decreased to 15 cps. Indeed, the 3D SIMS–SPM reconstruction shown in Figure 4b obtained after a primary ion dose of 2.4×10^{16} ions/cm^2 nicely correlates the changing SIMS $^{12}C_2^-$ signal with the changing angle of the surface of the structure.

Figure 4c shows the same sample after a SIMS analysis with a dose of 1.2×10^{17} ions/cm^2. The carbon layer was now completely removed by sputtering. As can be seen from the overlaid line scans taken before and after the end of the SIMS analysis and presented in Figure 4d, it is clearly noticeable that the topography of the TaN structure is changing. Due to the higher impact angle of the primary ion beam on the ridge's edge compared to the ridge's top surface or the trenches, the erosion rate is considerably higher in this area. The ridges therefore become narrower and the aspect ratio of the structure is not preserved during the SIMS analysis.

Mg(OH)$_2$ nanoclusters incorporated inside a polymer matrix
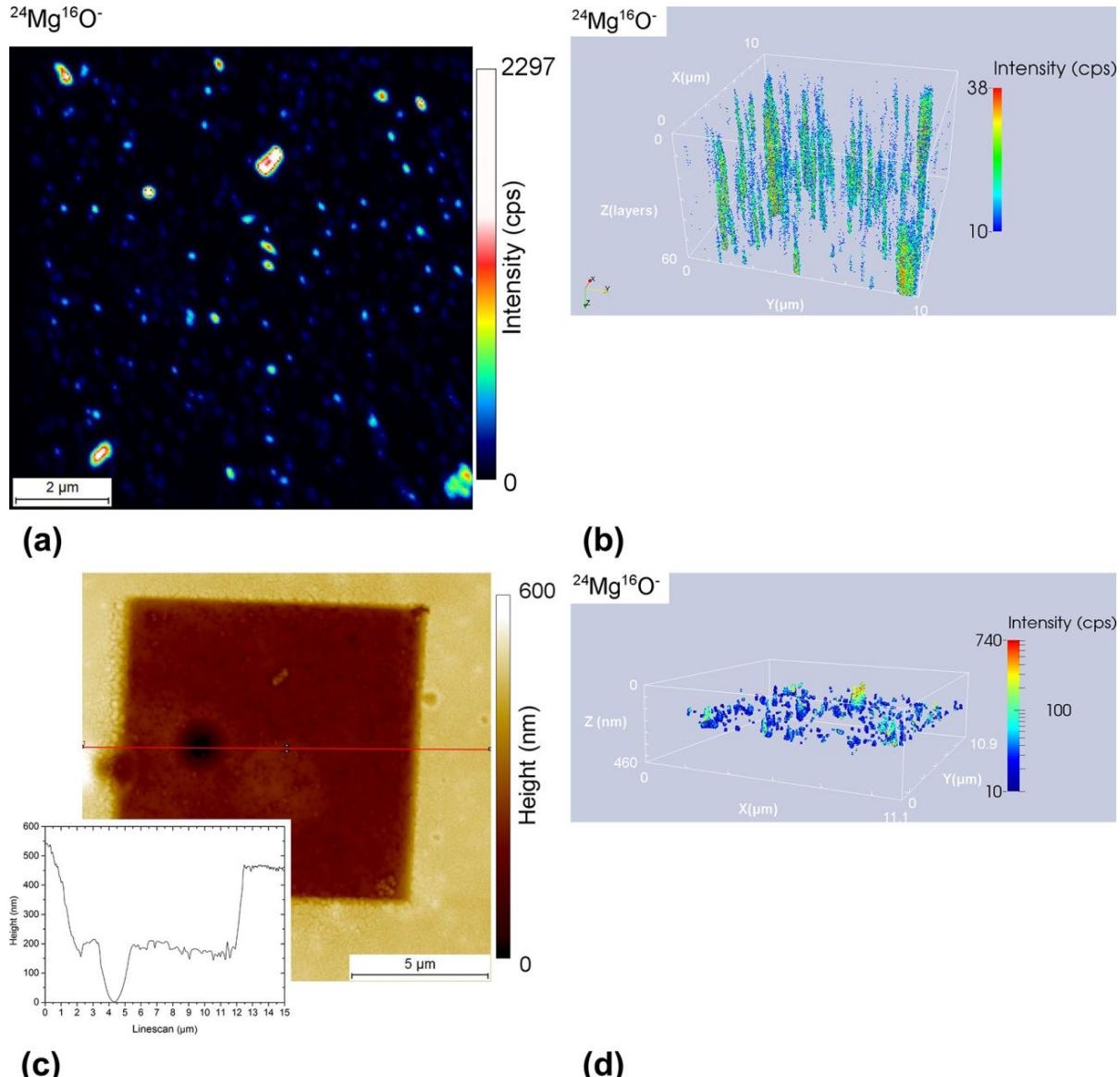
Due to the large differences in sputter rate from analysing various materials and material phases, the accurate co-localisation of nanoparticles inside a polymer matrix or inside biological tissue is very difficult. Combining SIMS with in situ AFM performed at different stages of the SIMS analysis helps to correct the depth scale and consequently gives a more accurate visualisation of the SIMS analysed volume as compared to the traditional SIMS reconstruction of the sputtered volume. Figure 5 shows the NanoSIMS 2D mapping of the $^{24}Mg^{16}O^-$ secondary ion signal summed over 60 layers (a), the traditional (b) and the combined SIMS–SPM (d) 3D reconstruction of the SIMS sputtered volume as well as the sample topography image after sputtering (c) of a polymer matrix incorporating 1 wt % of homogeneously distributed Mg nanoparticles in form of Mg(OH)$_2$ [23]. Similar samples produced by the same group are studied in [24]. In order to

visualize the nanoparticles, the secondary ion intensity of $^{24}Mg^{16}O^-$ was recorded on the NanoSIMS. Overall, the SIMS analysis of a $11.1 \times 10.9 \times 0.46$ μm^3 area took 5.5 h. The analysis was performed with a 2.5 pA Cs$^+$ primary beam.

From Figure 5a, it can be noticed that the Mg nanoparticles form clusters that range from 100 to 500 nm in diameter. Comparing Figure 5b and Figure 5d, the nanoparticles portrayed in Figure 5b seem to be strongly elongated in the z-direction whereas in Figure 5d, the nanoparticles look more compact, but mostly distributed in a much smaller depth range (the central third of the volume). All nanoparticles are located in the upper 327 nm deep volume section. In Figure 5b, the apparent distribution of the nanoparticles over most of the sample analysis depth (60 frames) is due to the lack of topography information in the traditional NanoSIMS 3D reconstruction. From Figure 5d it can be deduced, that due to the variation in sputtering rate between the embedded nanoparticles and the polymer matrix, the initially flat topography changes during Cs$^+$ bombardment and hillocks locally form at the locations of the nanoparticles. Thus, the maximum crater depth was only reached at x- and y-coordinates where no nanoparticles were found. This example and the previous examples show that the combined SIMS–AFM instrument could also help the user to analyse complicated structures such as multilayers comprising layers with different domains where differential sputtering occurs by simply flipping between the SIMS and AFM modes in a successive manner. Performing an analysis on such complicated structures would be very time consuming if not performed in situ. Knowing the sputter rates of each single layer (from measurement or literature), the analysis parameters could be programmed in a way that an AFM measurement is performed at each interface such that an accurate 3D map can be produced from the recorded SIMS and AFM data.

Conclusion

A correlative approach between secondary ion mass spectrometry and atomic force microscopy in a single instrument leads to 3D chemical maps with highest sensitivity and enhanced spatial accuracy. This combination of techniques is of particular interest to detect and eliminate artefacts due to inhomogeneous erosion rates caused by samples containing various materials, different phases or having a non-flat surface. Using the AFM information, the evolution of the topography as a result of the sputtering can be easily monitored and quantitatively accounted for when reconstructing 3D maps. As presented in this paper, the combined SIMS–AFM technique is particularly useful when the sample to be analysed is consisting of two very different materials, where the differential sputtering between the matrix and objects of interest is large. This is, for instance, the case when metallic nanoparticles in biological samples or

Figure 5: 2D mapping of $^{24}Mg^{16}O^-$ secondary ion signal summed over analysis depth (a). 3D volume reconstruction using the traditional method assuming a flat sample surface and a homogenous sample sputtering (b) Sample topography after SIMS sputtering including inset linescan plot illustrating the depth profile through the middle of the SIMS analysed area (c) 3D volume reconstruction making use of the combined information from SIMS and AFM (d). Panels b and d are shown at the same aspect angle.

polymer matrices are mapped. Hence, the example of the Mg nanoclusters embedded inside a polymer matrix nicely illustrates that the 3D reconstruction combining the chemical information from SIMS and the topography information from AFM is more accurate than the traditional SIMS 3D reconstruction.

Artefacts related to inhomogeneous secondary ion extraction efficiencies due to local field distortions caused by topography with high aspect ratios are also revealed by the combined

SIMS–AFM approach. This is nicely illustrated from the analysis of a nickel-based super-alloy. Thus, a fraction of $^{52}Cr^{16}O^-$ ions originating from the faster sputtering γ matrix are first deposited on the boundary walls of the Ni_3Al precipitate phase before finally being re-sputtered and extracted by the secondary optics of the mass spectrometer. While this type of artefact is much more difficult to be accounted for in a quantitative manner than artefacts related to differential sputtering, the SIMS–AFM data provides valuable additional information to the analyst for the interpretation of the SIMS results. Finally,

the SIMS–AFM solution is a way of measuring and comparing sputter rates more quickly. By locally measuring the topography at given stages of the SIMS analysis, the local change in topography could be mapped. In this way, we were able to measure the relative sputter rates between PS and PVP with the conclusion that PVP sputters 3.5 times faster than PS. Furthermore, with respect to the Ti(C,N) cermet, we found that the carbon-containing Ti grains sputter 2.8 times slower than the Co binding material. This same protocol could be used for the combined SIMS–AFM analysis of a multi-layered sample by recording the topography at each one of the interfaces. In the case where a number of layers presented multiple phases with large differences in sputter rate, the volume of sputtered material could be reconstructed more accurately.

Supporting Information

The archive in Supporting Information File 1 contains two videos (MPEG II) in which a sputtering experiment and a data reconstruction are shown. One video, TiCN_12C14N_16colors_mpeg2video.mpg, shows the "live sputtering" of Ti(C,N) cermet: The cermet's domains consisting of Ti and carbon containing grains on one hand and Co binder material on the other hand are sputtered at different rates during continued Cs^+ bombardment. During the analysis, consisting of 160 SIMS mappings, the $^{12}C^{14}N^-$ sputtered ion intensity is measured in cps. The field of view covers an area of $10 \times 10 \ \mu m^2$. The other video, Mg_nanoparticles_video_mpeg2video.mpg, shows a 3D reconstruction. This reconstruction makes use of the information from SIMS and SPM and shows the accurate distribution of $Mg(OH)_2$ nano-clusters located in the sputtered volume (field of view: $11.1 \times 10.9 \times 0.46 \ \mu m^3$). The recorded $^{24}Mg^{16}O^-$ intensity is shown in cps.

Supporting Information File 1

Animated videos of sputter experiment and data reconstruction.
[http://www.beilstein-journals.org/bjnano/content/supplementary/2190-4286-6-110-S1.zip]

Acknowledgements

References

1. Caplan, J.; Niethammer, M.; Taylor, R. M., II; Czymmek, K. J. *Curr. Opin. Struct. Biol.* **2011,** *21,* 686–693. doi:10.1016/j.sbi.2011.06.010
2. Williams, P. *Annu. Rev. Mater. Sci.* **1985,** *15,* 517–548. doi:10.1146/annurev.ms.15.080185.002505
3. McPhail, D.; Dowsett, M. Dynamic SIMS. In *Surface Analysis - The Principal Techniques;* Vickerman, J. C.; Gilmore, I., Eds.; John Wiley and Sons, 2009; pp 207–268.
4. Boxer, S. G.; Kraft, M. L.; Weber, P. K. *Annu. Rev. Biophys.* **2009,** *38,* 53–74. doi:10.1146/annurev.biophys.050708.133634
5. Cabin-Flaman, A.; Monnier, A.-F.; Coffinier, Y.; Audinot, J.-N.; Gibouin, D.; Wirtz, T.; Boukherroub, R.; Migeon, H.-N.; Bensimon, A.; Jannière, L.; Ripoll, C.; Norris, V. *Anal. Chem.* **2011,** *83,* 6940–6947. doi:10.1021/ac201685t
6. Wirtz, T.; Fleming, Y.; Gysin, U.; Glatzel, T.; Wegmann, U.; Meyer, E.; Maier, U.; Rychen, J. *Surf. Interface Anal.* **2013,** *45,* 513–516. doi:10.1002/sia.5010
7. Wirtz, T.; Fleming, Y.; Gerard, M.; Gysin, U.; Glatzel, T.; Meyer, E.; Wegmann, U.; Maier, U.; Odriozola, A. H.; Uehli, D. *Rev. Sci. Instrum.* **2012,** *83,* 063702–063709. doi:10.1063/1.4724308
8. Ngo, K. Q.; Philipp, P.; Kieffer, J.; Wirtz, T. *Surf. Sci.* **2012,** *606,* 1244–1251. doi:10.1016/j.susc.2012.04.003
9. García, R.; Pérez, R. *Surf. Sci. Rep.* **2002,** *47,* 197–301. doi:10.1016/S0167-5729(02)00077-8
10. Ewing, G. E. *Chem. Rev.* **2006,** *106,* 1511–1526. doi:10.1021/cr040369x
11. Thomson, N. H. *J. Microsc. (Oxford, U. K.)* **2005,** *217,* 193–199. doi:10.1111/j.1365-2818.2005.01399.x
12. Fleming, Y.; Wirtz, T.; Gysin, U.; Glatzel, T.; Wegmann, U.; Meyer, E.; Maier, U.; Rychen, J. *Appl. Surf. Sci.* **2011,** *258,* 1322–1327. doi:10.1016/j.apsusc.2011.09.029
13. Schneider, C. A.; Rasband, W. S.; Eliceiri, K. W. *Nat. Methods* **2012,** *9,* 671–675. doi:10.1038/nmeth.2089
14. *OpenMIMS,* Version 2.5 (rev 713); National Resource for Imaging Mass Spectrometry: Cambridge, MA, U.S., 2012.
15. *SPIP,* Version 6.0.13; Image Metrology A/S: Hørsholm, Denmark, 2013.
16. Henderson, A.; Ahrens, J.; Law, C. *The ParaView Guide;* Kitware Inc.: New York, U.S., 2004.
17. *MayaVi 2,* Version 4.2.1; Enthought, Inc.: Austin, TX, U.S., 2012.
18. Pollock, T. M.; Tin, S. *J. Propul. Power* **2006,** *22,* 361–374. doi:10.2514/1.18239
19. Reed, R. C. *The Superalloys: Fundamentals and Applications;* Cambridge University Press: Cambridge, U.K., 2008.
20. Fleming, Y.; Eswara Moorthy, S.; Wirtz, T.; Gerard, M.; Gysin, U.; Glatzel, T.; Meyer, E.; Maier, U. High-sensitivity high-resolution elemental 3D analysis by in-situ combination of SIMS and SPM. In *Proceedings of the Eighteenth International Microscopy Congress,* Prague, Czech Republic, Sept 7–12, 2014; Hozák, P., Ed.; Czechoslovak Microscopy Society, 2014; pp 1170 ff.
21. Morales-Rodríguez, A.; Gallardo-López, A.; Domínguez-Rodríguez, A.; Córdoba, J. M.; Avilés, M. A.; Gotor, F. J. *J. Eur. Ceram. Soc.* **2011,** *31,* 299–302. doi:10.1016/j.jeurceramsoc.2010.10.007

22. Koster, N. B.; Geluk, C. P. E. C.; Versloot, T. W.; Janssen, J. P. B.; Fleming, Y.; Wirtz, T. *Proc. SPIE* **2014,** *9235,* 923517. doi:10.1117/12.2066471

23. Dreyer, A., member of Prof. Dr. C. Vogt's group, Leibniz University of Hannover, Personal Communication, Nov 2014.

24. Schwartze, G. Polymere Ein-und Mehrschichtmaterialien für die Kalibrierung moderner festkörper-spektroskopischer Messsysteme. Ph.D. Thesis, Gottfried Wilhelm Leibniz University of Hannover, Hanover, Germany, 2013.

Thermal treatment of magnetite nanoparticles

Beata Kalska-Szostko[*1], Urszula Wykowska[1], Dariusz Satula[2] and Per Nordblad[3]

Full Research Paper

Open Access

Abstract

This paper presents the results of a thermal treatment process for magnetite nanoparticles in the temperature range of 50–500 °C. The tested magnetite nanoparticles were synthesized using three different methods that resulted in nanoparticles with different surface characteristics and crystallinity, which in turn, was reflected in their thermal durability. The particles were obtained by coprecipitation from Fe chlorides and decomposition of an Fe(acac)$_3$ complex with and without a core–shell structure. Three types of ferrite nanoparticles were produced and their thermal stability properties were compared. In this study, two sets of unmodified magnetite nanoparticles were used where crystallinity was as determinant of the series. For the third type of particles, a Ag shell was added. By comparing the coated and uncoated particles, the influence of the metallic layer on the thermal stability of the nanoparticles was tested. Before and after heat treatment, the nanoparticles were examined using transmission electron microscopy, IR spectroscopy, differential scanning calorimetry, X-ray diffraction and Mössbauer spectroscopy. Based on the obtained results, it was observed that the fabrication methods determine, to some extent, the sensitivity of the nanoparticles to external factors.

Introduction

Nanostructured magnetite has become one of the most investigated materials due to its unusual magnetic properties. In addition, it is recognized as an inert compound that is almost entirely nontoxic to living organisms [1]. Apart from that, iron and its oxides on the nanometer scale can possess superparamagnetic properties, allowing for their application in various fields. The list of possible applications encompasses biomedical engineering, MRI contrast agents, hyperthermia treatment, sensing and biosensing [2,3]. They are also very promising

candidates for electrical-related applications, for example, energy and magnetic storage materials, sensors and catalysts [4], or even environmental remediation or sieves [5]. For this reason, the study of the physical properties and the chemical and thermal stability of ferrite nanoparticles is of crucial importance [6]. Moreover, magnetite nanostructures can be relatively easy to obtain by a simple synthetic procedure [7]. All of the above-mentioned advantages promote the popularity of ferrite nanoparticles. Additionally, there is the possibility to fabricate

many different forms of iron oxides. During each step of the synthesis process, a structure transformation can be expected, resulting in various magnetic properties, and therefore, application potential. It has been observed that even at the synthesis level, due to the oxidation process, a structural transformation can be expected. This brings about new features of the magnetic properties which can be applied [8]. In addition, surface modification by the deposition of a chemically dissimilar layer (e.g., Ag) can be of particular importance, especially in the case of bio-related applications [9]. Another critical problem faced by researchers is that it is very difficult to obtain nanoparticles with exactly the same well-defined size, morphology and shape from different synthetic methods. As far as the applications are concerned, the production of a desired size and good characterization of the obtained magnetic nanoparticles are very important factors. To obtain a desired range of diameters, strict control of the reaction conditions, such as the synthesis time, temperature, concentration of the reactants and added surfactants, must be maintained. Furthermore, it has been observed that the size of the particles increases with extended synthesis time [8]. On the other hand, the particle size can be modified by using surfactants with various carbon chain lengths [10-12].

Few types of nanoparticles have been extensively studied over large temperature ranges. It has been shown that in some systems, at room temperature, the nanoparticles tend to exhibit spontaneous growth [13]. This phenomenon is called anomalous grain growth. On the other hand, it has been shown that for particular granular powders, the thermal stability increases with larger grain size [14]. These size-related effects are explained by enthalpy and stress, which influences the activation energy value [15]. Thermal sensitivity depends, in most cases, mainly on the type of nanomaterial and method of fabrication [16].

As for all nanomaterials, the properties of magnetite change on the nanoscale. At the bulk level, the oxidation of magnetite to hematite at room temperature is inhibited, and only by heating to 600 °C can changes in the crystalline structure be achieved [17]. At the nanoscale level, changes in the crystalline structure can be expected and observed at much lower temperatures, even very close to the room temperature. This is related to surface enthalpy and activation energy, which are size dependent [18]. It was found that Fe nanoparticles oxidize to a mixture of iron oxides (γ-Fe_2O_3 and α-Fe_2O_3) even at 200 °C [19]. However, this temperature can vary due to the high surface area and various activity of the nanoparticles, which results in a more exothermic heat process during oxidation at low temperature. In general, it can be assumed that phase transformation in nanogranular systems occurs from 200 to 600 °C with different

contribution from both oxides, γ-Fe_2O_3 and α-Fe_2O_3 [20]. It should also be underlined that the data regarding the behavior of nanosystems at elevated temperatures are very different and generalizations cannot be made [16].

In this paper, tests of three different kinds of magnetite nanoparticles and their behavior at higher temperatures starting from 50 °C up to 500 °C have been selected. Some changes in differential scanning calorimetry (DSC) cycles have been observed in our previous measurements [21] for short temperature cycles. However, these changes were not very specific. To observe possible particle phase transformations, heat treatment was performed for 24 h.

Experimental
Materials and apparatus
To obtain the various magnetite nanoparticles, the following chemicals were purchased from Aldrich and Fluka: $Fe(acac)_3$, 1,2-hexadecanediol, phenyl ether, $FeCl_3 \cdot 6H_2O$, $FeCl_2 \cdot 4H_2O$, $AgNO_3$, NH_3 solution and oleic acid; tetrabutylammonium hydroxide (TBAOH), 1-octadecanol and oleylamine, respectively. The cleaning and rough size separation of the nanoparticles were performed by the magnetic field separation method with the use of acetone, sonic bath treatment and a permanent magnet. The thermal treatment was performed in an air flow furnace.

FTIR spectra were collected in reflection mode at room temperature (RT) using a Nicolet 6700 Infrared spectrometer working in the spectral range between 500–4000 cm^{-1}. The quality of the nanopowders was observed using a Tecnai G2 X-TWIN transmission electron microscope (TEM). The analysis of the crystal structure was carried out using an Agilent Technologies SuperNova X-ray diffractometer (XRD) with a Mo microfocused source (Mo Kα = 0.713067 Å). The thermal analysis of the magnetite and core–shell nanoparticles was performed on a Mettler Toledo differential scanning calorimeter (DSC). A Quantum Design MPMS SQUID magnetometer was used for the magnetization measurements. Mössbauer spectra (MS) were obtained using a conventional spectrometer working in constant acceleration mode at RT with a CoCr radioactive source.

Preparation of magnetite nanoparticles
As was previously mentioned, the tested magnetite nanoparticles (MNP-1, MNP-2, MNP-3) were obtained by three different synthetic methods. The first one is based on coprecipitation of iron(II) and iron(III) chlorides in aqueous ammonia solution (MNP-1). This is a low temperature reaction that was conducted at 80 °C under Ar atmosphere. The procedure was adopted from the Massart method [7,22,23].

The second (MNP-2) and third (MNP-3) type of nanoparticles were based on the layer-by-layer synthetic procedure, where thermal decomposition of iron(III) acetylacetone salts in a phenyl ether solution was provided. This reaction was prepared using the following conditions: −230 °C, oxygen-free environment, and Ar flow. The main points of the described synthesis were first proposed by Sun et al. and further details can be found there [24,25].

The nanoparticles obtained from the Fe(acac)$_3$ complex were also modified with a silver shell (third synthetic procedure, MNP-3). In this case, magnetite nanoparticles in the reaction solution were mixed with the following reactants: AgNO$_3$ (2 mmol), 1,2-hexadecanediol (1 mmol), phenyl ether (20 mL) and oleylamine (2.5 mmol). The solution was mixed for 15 min at RT, then for 2 h at 30 °C, and at the end for 30 min at 140 °C [26,27]. When the solution was cooled down, the nanoparticles were separated from the solution with a permanent magnet, washed in deoxygenated acetone and dried to powder form with a vacuum evaporator.

Results and Discussion
Gravimetric results
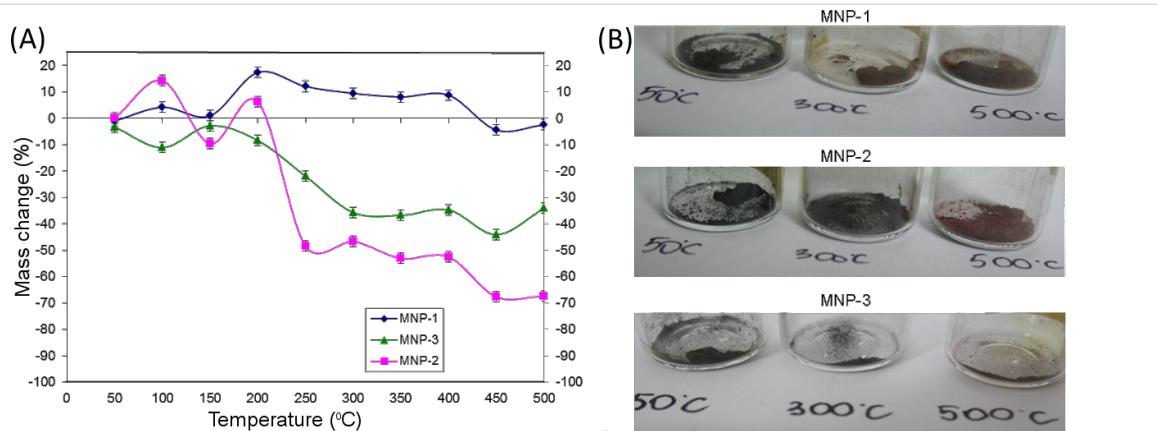
The resulting precipitates were dried to powder form in a vacuum evaporator. The obtained nanoparticles were thermally treated in an oven in the temperature range 50–500 °C for 24 h with a temperature step of 50 °C. The as-prepared nanoparticles were pretested using the techniques presented in this paper. Starting from 50 °C, before and after heating, the powder mass was checked and the weight change is plotted in Figure 1A. A gradual color change of the powder upon heating was simultaneously observed, which is depicted in Figure 1B.

For all of the nanoparticles, a gradual transition from black to reddish brown was observed (see Figure 1B). However, this did not occur at the same temperature for all samples. A much more rapid color transformation was noticed in the case of the MNP-2 particles in comparison to MNP-1. The coating of the magnetite nanoparticles with a silver shell (MNP-3) shows that the color change is less pronounced and not as intense as in the case of the uncoated particles. This implies that an additional metallic layer changes the thermal stability, and therefore, partial protection from the oxidation process is achieved.

This observation was also confirmed by the mass change, where it can be seen that MNP-3 particles show less pronounced changes in mass in comparison to MNP-2 and the mass loss is shifted toward higher temperatures. The MNP-1 sample had almost no mass change over the studied temperature range. In Table 1, the details of the mass changes of the nanoparticles before and after heating are collected.

First of all, it can be seen that the MNP-1 nanoparticle system is much more stable over the studied temperature range. An observed difference in mass is smaller than 20%. Over the temperature range 50–425 °C, a slight increase in the particle weight is observed. This could be due to the adsorption of oxygen on the particle surface, which penetrates to the core of the nanoparticle. At higher temperatures the release of these gases from the surface is possible. For this series of particles, only a slight modification of the powder color is observed. For the MNP-2 particles, a more rapid change in color was observed, accompanied by a drastic decrease of the powder weight in the temperature range 200–300 °C. The difference in temperature stability for both types of particle cores can be connected with a difference in the morphology of individual particles. Precipitation from chlorides (MNP-1) leads to the formation of a well-defined monocrystalline structure [28], while thermal decomposition of Fe(acac)$_3$ (MNP-2 and MNP-3) causes the growth of rather polycrystalline particles. This was


Figure 1: (A) Mass change of the nanoparticle powders (%) with respect to the temperature variation. (B) Color change of the nanoparticles after heating.
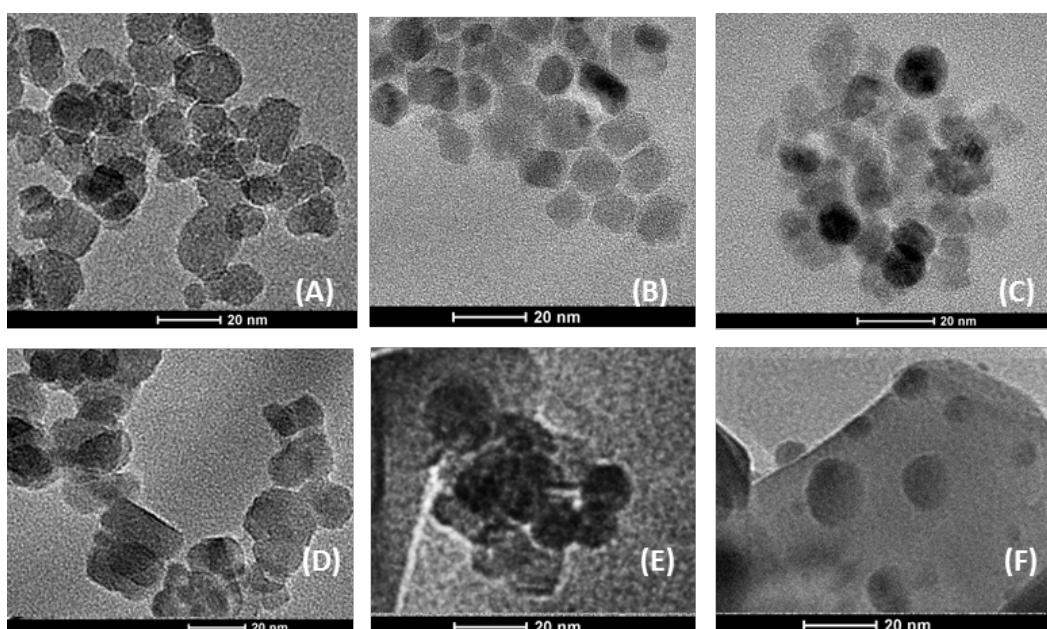
Table 1: Mass change of nanoparticles before and after heat treatment.

Temperature [°C]	MNP-1			MNP-2			MNP-3		
	Before [g] ±0.005	After [g] ±0.005	Mass difference [%][a] ±0.5	Before [g] ±0.005	After [g] ±0.005	Mass difference [%][a] ±0.5	Before [g] ±0.005	After [g] ±0.005	Mass difference [%][a] ±0.5
50	0.098	0.097	−1.0	0.091	0.091	0.0	0.095	0.092	−3.3
100	0.095	0.099	+4.2	0.084	0.096	+14.3	0.097	0.087	−11.1
150	0.101	0.102	+1.0	0.094	0.085	−9.6	0.098	0.095	−2.8
200	0.092	0.108	+17.4	0.095	0.101	+6.3	0.099	0.091	−8.4
250	0.091	0.102	+12.1	0.091	0.067	−48.4	0.098	0.077	−21.9
300	0.095	0.104	+9.5	0.090	0.048	−46.7	0.099	0.063	−35.7
350	0.099	0.107	+8.1	0.096	0.045	−53.1	0.099	0.063	−36.8
400	0.091	0.099	+8.8	0.099	0.035	−52.5	0.099	0.065	−34.7
450	0.098	0.094	−4.4	0.099	0.032	−67.7	0.100	0.065	−44.1
500	0.099	0.097	−2.4	0.101	0.033	−67.3	0.098	0.065	−34.1

[a]+ mass increase; − mass decrease.

especially clearly observed when larger particles were grown and can be expected from the synthesis. The existence of interfaces between separate crystallites inside each particle can be the reason for a faster oxidation process. Such a scenario is in good agreement with the speculation that polycrystallinity causes the presence of grain boundaries, which significantly influences the stability/susceptibility to the oxide. On the other hand, in the case of polycrystalline particles, their structure is also less dense and oxygen can penetrate more easily inside the particle along the edges of structural discontin-

uation. Also, the surface chemistry is different from the previous case and it can behave differently at elevated temperature where partial evaporation could occur. The comparison of MNP-3 with MNP-2 particles shows that the mass loss is much smaller, only up to 44% (450 °C for MNP-2), in comparison to 67% for MNP-3. For MNP-3 nanoparticles, we have not observed any mass increase during heating. This also proves that metallic shell strengthens the thermal stability of the nanoparticles by sealing the surface, which prevents oxygen penetration.

Figure 2: TEM images of magnetite nanoparticles before (as-prepared) (A, B, C) and after the heating process at 500 °C (D, E, F), for MNP-1, MNP-2, and MNP-3, respectively.

TEM microscopy

The morphology of magnetite nanopowders before (as prepared) and after heating at 500 °C was observed by TEM on the powdered sample supported on a 400 mesh Cu grid covered by amorphous carbon. The obtained images are depicted in series in Figure 2.

In Figure 2, six images of nanoparticles are depicted. Figure 2A shows MNP-1 before heating and Figure 2D after heat treatment at 500 °C for 24 h. The comparison of these images leads to the conclusion that there is not much difference in shape between the particles before and after heating. The crystalline structure, the shape and the size of the nanoparticles has been preserved. Figure 2B shows the as-prepared MNP-2 nanoparticles in Figure 2E, where these nanoparticles are presented after heating under the same conditions as in the previous case. The comparison of these two images allows for the observation that the morphology of the nanoparticles also does not change after heat treatment. Only the lateral distribution is much worse. For the MNP-3 series, the appearance of the particles after heating is the most different from the as-prepared case but the size and shape of the structures are maintained.

X-ray diffraction

All thermally tested nanoparticles were measured by XRD to observe the evolution in their crystalline structure in the studied temperature range. The obtained results in the series are depicted in Figures 3–5.


Figure 4: X-ray pattern of MNP-2 nanoparticles after the heating process.
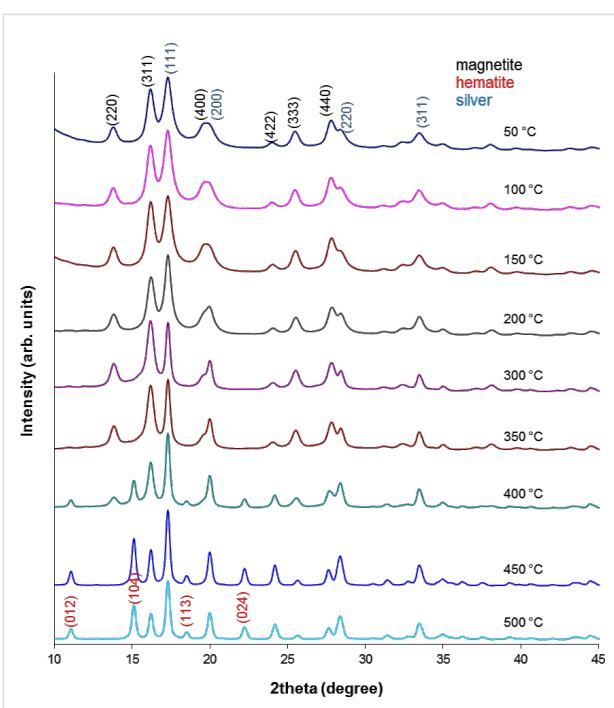
Figure 5: X-ray pattern of MNP-3 nanoparticles after the heating process.

Figure 3: X-ray pattern of MNP-1 nanoparticles after the heating process.

Here, in each set of XRD patterns, the well-defined crystalline structure of magnetite and/or maghemite with indexes (*hkl*) ascribed to (220), (311), (400), (422), (333) and (440) [12,29] are observable. MNP-1 nanoparticles do not show any significant amount of additional structure up to 400 °C and therefore no additional patterns are presented. At 450 °C and 500 °C a

small amount of hematite develops. Nevertheless, the intensity of the respective peaks is relatively low. However, MNP-2 nanoparticles develop strong signals even at 400 °C, which are typical for the hematite structure and are indexed as (012), (104), (113), (024) and (214) [30]. Their intensity is as high as that observed at 500 °C for the previous series. The MNP-3 particles are also stable only up to 400 °C, and above this temperature the hematite structure can be seen together with the magnetite/maghemite phase and metallic Ag (111), (200), (220) and (311) [31]. This proves that the MNP-2 nanoparticles are less stable with respect to temperature, especially at highest tested temperatures, in comparison to MNP-1. A lower sensitivity to external factors for the MNP-2 particles was also observed with regards to aqueous solution stability [20].

To determine the average grain size of the nanoparticles before and after heating, a quantitative analysis was performed using Scherrer's equation [32]:

$$D = \frac{0.9 \cdot \lambda}{B_{1/2} \cdot \cos\theta}, \qquad (1)$$

where D is the grain size (Å), λ is the wavelength (Mo source, 0.7136 Å), $B_{1/2}$ is the full width at half maximum intensity of the peak (rad), and θ is the diffraction angle (rad). The calculated results for these particles are compiled in Table 2.

Table 2: Estimated grain sizes of thermally treated nanoparticles, determined by X-ray diffraction.

Temperature	MNP-1 grain size [nm] ±2	MNP-2 grain size [nm] ±2	MNP-3 grain size [nm] ±2
As-prepared	16	11	11
50 °C	18	12	10
100 °C	17	13	11
150 °C	18	13	11
200 °C	19	12	10
250 °C	20	12	11
300 °C	16	13	13
350 °C	18	13	12
400 °C	17	13	14
450 °C	17	18	18
500 °C	15	24	25
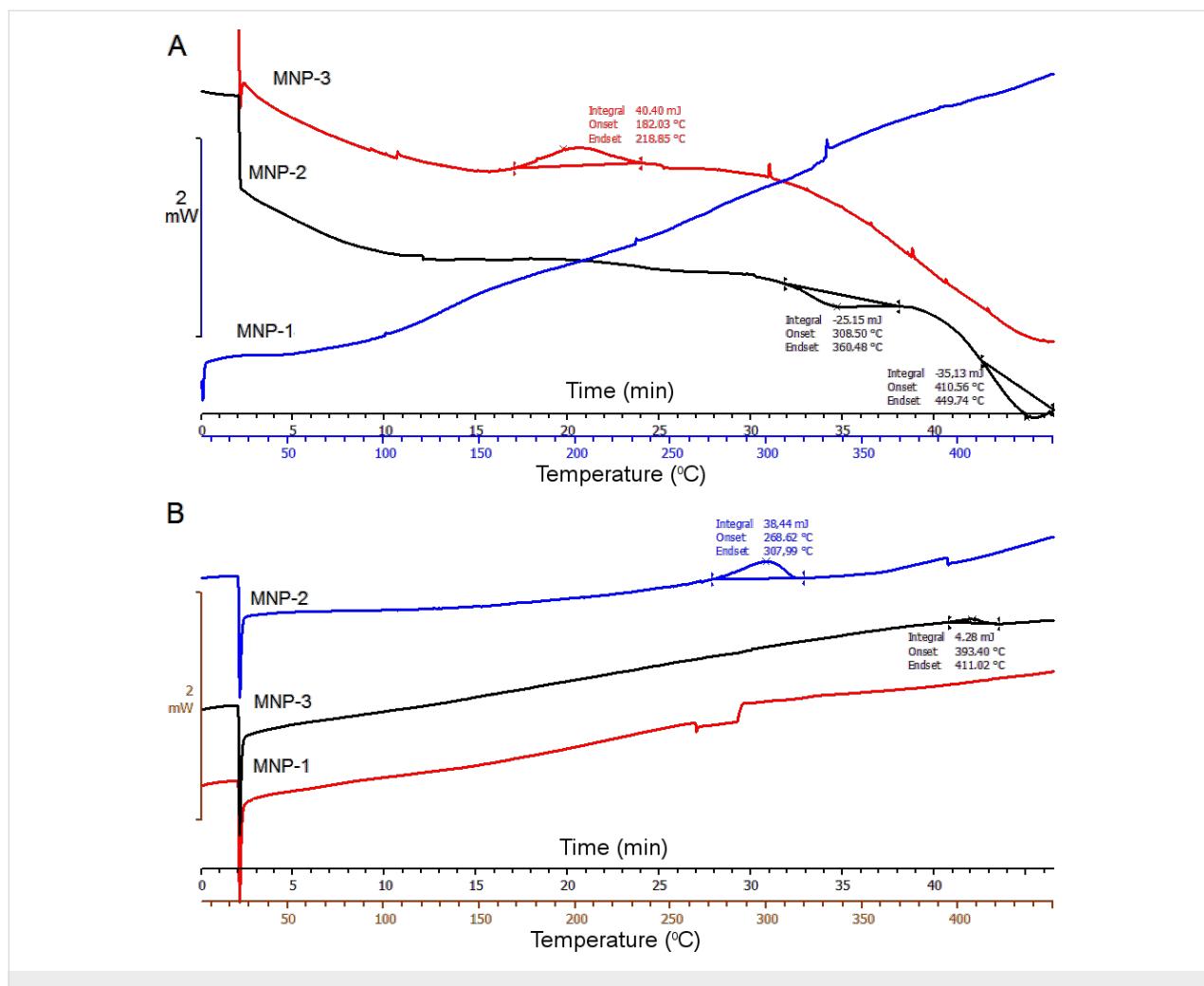
The results presented in Table 2 show that MNP-1 particles preserve their average particle size regardless of temperature treatment, while MNP-2 and MNP-3 particles tend to increase the average diffracting zone above 400 °C (which can be suggested by the aggregation of the particles). This observation again proves that the two proposed synthetic procedures result in differing quality of the particle core. The discrepancy

between the TEM average particle size and that calculated from Equation 1 originates from the fact that different factors (e.g., nonlinear detector parameters, structural defects, tension, composition variation, crystal imperfections, etc.) significantly contribute to the broadening of the line width of the XRD patterns [33]. Therefore, the average particle size calculated this way is only a rough estimation. The temperature dependence of the line width also shows that heat tends to relax the imperfection of the particle core, and therefore, the average particle size appears much larger than it actually is [34]. The temperature treatment also relaxes some imperfection of the crystals, which at lower temperature cause line broadening.

Differential scanning calorimetry

A quick (1 hour) heating and cooling cycle in the temperature range 2–450 °C with a scan rate of 10 °C/min was conducted for extreme samples. As a reference, an empty pan was heated at the same time. For each DSC measurement, a quantity of about 2 mg of the nanoparticle powder was sealed in an Al crucible. The collected temperature scan curves are depicted in Figure 6.

Figure 6 presents the DSC curves of the three studied types of nanoparticles. In Figure 6A we can see reference thermal cycles of nanoparticles before the heating process. In Figure 6B nanoparticles heated up to 500 °C for 24 h in each case are collected. As can be seen, the reference curves show few thermal changes. MNP-3 nanoparticles show one exothermic process over the temperature range 182–218 °C with 40.4 MJ of energy. For the MNP-2 nanoparticles, two endothermic processes appear above 300 °C: the first at 306–360 °C and the second at 410–449 °C, with −25 and −35 MJ of energy, respectively. MNP-1 nanoparticles do not present any thermal changes, which implies that they are not modified in the studied temperature range and that they have better thermal stability in comparison to the other particles. The temperature cycles of nanoparticles after the heating process are a bit different compared to the unheated ones. At first, MNP-3 shows only very small exothermic process at 393–411 °C, while MNP-2 exhibits an exothermic process at 266–307 °C with 38 MJ of energy (in contrast to the reference curve). The MNP-1 curve also does not show any thermal changes. The described results are in good agreement with XRD studies, which showed that thermal changes and oxidation of MNP-2 and MNP-3 particles start much faster than in case of MNP-1. The DSC data also confirm the gravimetric results where for MNP-1 nanoparticles the weight change with temperature remains almost constant, while MNP-2 and MNP-3 exhibit changes. Therefore, the DSC curve slopes before heat treatment are different for MNP-1, MNP-2 and MNP-3. The observed behavior suggests the opposite curve slope trend between those samples, which is in agreement with

Figure 6: DSC curves of reference nanoparticles before heating (A) and after heating at 500 °C (B).

the gravimetric results. The comparison of the DSC curves between the samples after heating for 24 h at 500 °C suggests that the surface and/or core modification no longer takes place – the slope of each line is the same. This result explains the gravimetric results and supports the scenario that for MNP-1, surface ligands are rigidly fixed to the sample and do not contain any weakly adsorbed solvents. However, MNP-2 and MNP-3 most likely contain residuals of solvents that gradually evaporate, which is not observed for the samples measured after heat treatment.

IR spectroscopy

Magnetite nanoparticles were further tested by IR spectroscopy to observe changes taking place on the nanoparticles surface due to temperature treatment. The representative spectra are collected in Figure 7.

Figure 7 shows the selected IR spectra of the nanoparticles after heat treatment in an oven in the temperature range from 50 to 500 °C. In Figure 7A we observe the IR spectra of MNP-1 nanoparticles, in Figure 7B for the MNP-2 sample, and in Figure 7C for MNP-3. Heating resulted in oxidation of magnetite firstly to maghemite then to hematite for all types of nanoparticles. When the particles are heated to temperatures up to 150 °C, Fe–O bonds typical for Fe_3O_4 are still preserved (560–580 cm^{-1}) [6]. Nevertheless, in almost every spectrum, oxidation to hematite (540 cm^{-1}), maghemite (647–679 cm^{-1}) [35], lepidocrocite (730 and 1060 cm^{-1}) [36], goethite (860 cm^{-1}) [37] and ferrihydrite (964 cm^{-1}) [35] is well observed, which suggests a slow surface oxidation process. The other bands reported in Figure 7A belong to N–H bonds originating from TBAOH used during the synthesis procedure (1515 cm^{-1} and 2164–2654 cm^{-1}). For the as-prepared sample, there are C=O bonds present typical for acetone (1710 cm^{-1}) and those present in the carbon chain in the TBAOH solution (2900–2974 cm^{-1}) [38]. In Figure 7B we can also observe bands connected with the presence of Ar–O–Ar bonds (1233 cm^{-1}), acetylacetonate groups (1455–1558 cm^{-1}),
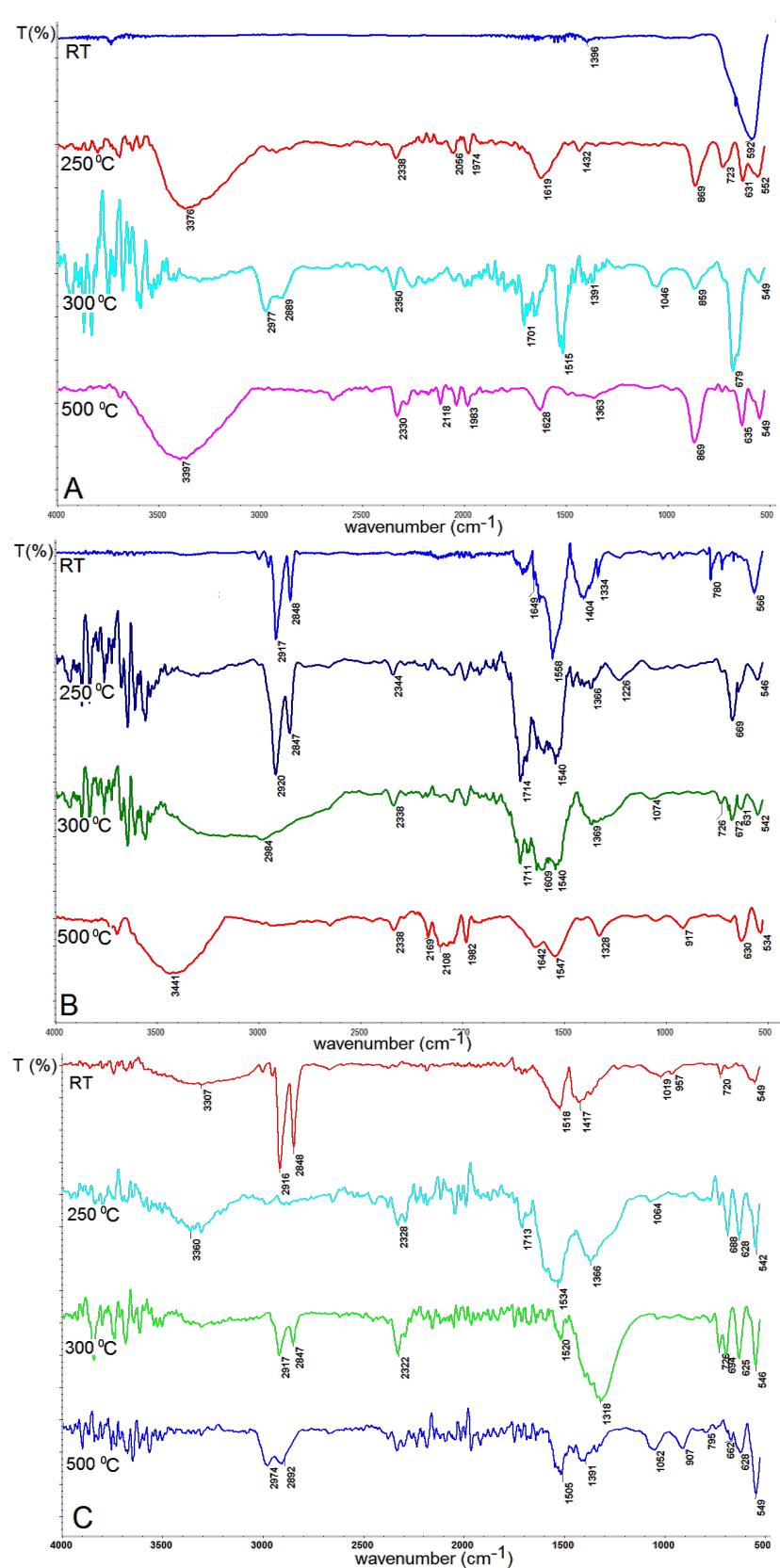
Figure 7: IR spectra of magnetite nanoparticles (A) MNP-1, (B) MNP-2, (C) MNP-3 before and during the heating process.

Figure 9: Mössbauer spectra of nanoparticles tested under different temperatures: (A) MNP-1, (B) MNP-2, (C) MNP-3 along with (D) examples of respective fits.

spectra consist of a sextet with a relatively wide line at half maximum, which is connected with the overlapping of the magnetite, maghemite and hematite subspectra. The quantitative analysis suggests that the relative intensity ratio of Fe in these two phases is roughly equal to 4:78:18, respectively, at 500 °C (see Figure 9D).

In Figure 9B, the RT spectra of MNP-2 nanoparticles are depicted. There, the spectra transform much more significantly in comparison to the other series. The spectra of the as-prepared and low temperature heated particles are in the singlet form and only one broad line is seen. These types of magnetite particles are above the superaparamagnetic blocking temperature. With an increase in temperature during the heat treatment, the

observed MS spectra become broader and finally, above 150 °C, they start to split into the sextet typical for the mixture of magnetite/maghemite [43]. After further temperature treatment above 400 °C, the hematite sharp lines start to appear as well. At 450 °C the coexistence of both phases is clearly seen. Finally, the simple sextet with very sharp lines is observed at 500 °C (with hyperfine parameters typical for hematite magnetic hyperfine field ≈52 T, quadruple splitting ≈0.2 mm/s, which is in good agreement with the bulk values (Figure 9D) [44-48].

Figure 9C presents the spectra of MNP-3 nanoparticles. The results show that the Ag shell does not significantly influence the thermal core stability because the oxidation process is as

effective as it was observed for the uncoated particles. Therefore, the Ag shell extends the properties of magnetite nanoparticles, but the thermal stability of the core is not significantly protected. This suggests that the amount of oxide that is trapped in the particle volume is large enough for thermal oxidation maintenance, but no additional oxide can access the core.

It can be seen from the qualitative analysis that the MNP-2 particles are much more sensitive to the oxidation process in comparison to other particles. A possible explanation of the observed scenario is that the nanoparticles have different inherent structures that significantly influence the superparamagnetic blocking temperature. One argument is that the MNP-1 particles, which can be treated as single crystals, have been obtained. This can be seen in HRTEM studies [49]. Therefore, oxide penetration is hampered and becomes much slower. The stepwise decomposition of the Fe(acac)$_3$ complex causes the presence of grain-like growth of each subsequent layer. This introduces many more grain boundaries and dislocations, and therefore, more room for oxide penetration, which significantly facilitates the oxidation process.

Conclusion

The performed experiments show that thermal stability of magnetite nanoparticles is dependent on the fabrication procedure. The temperature scans, combined with structural and magnetic measurements, depict that nanoparticles of the same size but different oxidation state are not in the same magnetic state at RT. This is extremely important with regards to their application. A slow heat treatment allows modification of the oxidation state, but not of the particle size. The variations between magnetite, maghemite and hematite can lead to the fabrication of particles with desired and well-defined magnetic properties. It is shown that the magnetic state can be tuned after the fabrication process by post-treatment, which is in a good agreement previous studies. The lack of temperature treatment stability and the evolution of different oxides show the complexity behind the science regarding the nanostructure study. The development of various magnetic particles originates from the same compound, which makes the nanoscience more unpredictable but, at the same time, very interesting to study. Taking into account the different nature of the oxides present in the nanosized particles, further investigation of the nanoparticles in an external magnetic field is planned.

Acknowledgement

References

1. Das, M.; Mishra, D.; Maiti, T. K.; Basak, A.; Pramanik, P. *Nanotechnology* **2008,** *19,* 415101. doi:10.1088/0957-4484/19/41/415101
2. Akbarzadeh, A.; Samiei, M.; Davaran, S. *Nanoscale Res. Lett.* **2012,** *7,* 144. doi:10.1186/1556-276X-7-144
3. Vatta, L. L.; Sanderson, R. D.; Koch, K. R. *Pure Appl. Chem.* **2006,** *78,* 1793–1801.
4. Issa, B.; Obaidat, I. M.; Albiss, B. A.; Haik, Y. *Int. J. Mol. Sci.* **2013,** *14,* 21266. doi:10.3390/ijms141121266
5. Tang, S. C. N.; Lo, I. M. C. *Water Res.* **2013,** *47,* 2613–2632. doi:10.1016/j.watres.2013.02.039
6. Kalska-Szostko, B.; Wykowska, U.; Piekut, K.; Satuła, D. *Colloids Surf., A* **2014,** *450,* 15. doi:10.1016/j.colsurfa.2014.03.002
7. Kalska-Szostko, B.; Rogowska, M.; Dubis, A.; Szymański, K. *Appl. Surf. Sci.* **2012,** *258,* 2783. doi:10.1016/j.apsusc.2011.10.132
8. Kalska-Szostko, B.; Zubowska, M.; Satula, D. *Acta Phys. Pol., A* **2006,** *109,* 365.
9. Kalska-Szostko, B.; Rogowska, M.; Dubis, A.; Basa, A. *J. Surf. Interfaces Mater.* **2014,** *2,* 69–73. doi:10.1166/jsim.2014.1036
10. Wu, W.; He, Q.; Jiang, C. *Nanoscale Res. Lett.* **2008,** *3,* 397. doi:10.1007/s11671-008-9174-9
11. Hyeon, T. *Chem. Commun.* **2003,** 927. doi:10.1039/B207789B
12. Kalska-Szostko, B.; Rogowska, M.; Satuła, D. *Colloids Surf., B* **2013,** *111,* 656. doi:10.1016/j.colsurfb.2013.07.004
13. Andrievskii, R. A. *Russ. Chem. Rev.* **2002,** *71,* 853.
14. Low, I. M.; Oo, Z. *AIP Conf. Proc.* **2010,** *1202,* 27. doi:10.1063/1.3295604
15. Li, W.; Ni, C.; Lin, H.; Huang, C. P.; Ismat, S. M. *J. Appl. Phys.* **2004,** *96,* 6663. doi:10.1063/1.1807520
16. Kaisersberger, E. *Thermoanalytical characterization of nanomaterials;* New Research trends in materials science, ARM-5, Sibiu, Romania, 2007.
17. Lepp, H. *Am. Mineral.* **1957,** *42,* 679.
18. Guisbiers, G.; Abudukelimu, G.; Hourlier, D. *Nanoscale Res. Lett.* **2011,** *6,* 396. doi:10.1186/1556-276X-6-396
19. Li, X. G.; Chiba, A.; Takahashi, S.; Sato, M. *J. Appl. Phys.* **1998,** *83,* 3871. doi:10.1063/1.366619
20. Liu, T.; Shao, H.; Li, X. *Nanotechnology* **2003,** *14,* 542. doi:10.1088/0957-4484/14/5/311
21. Kalska-Szostko, B.; Wykowska, U.; Satuła, D.; Zambrzycka, E. *Colloids Surf., B* **2014,** *113,* 295. doi:10.1016/j.colsurfb.2013.09.032
22. Massart, R.; Cabuil, V. *J. Chim. Phys. Phys.-Chim. Biol.* **1987,** *84,* 967.
23. Kalska-Szostko, B.; Rogowska, M. *J. Nanosci. Nanotechnol.* **2012,** *12,* 6907. doi:10.1166/jnn.2012.6563
24. Sun, J.; Zhou, S.; Hou, P.; Yang, Y.; Weng, J.; Li, X.; Li, M. *J. Biomed. Mater. Res., Part A* **2007,** *80A,* 333–341. doi:10.1002/jbm.a.30909
25. Kalska-Szostko, B.; Wykowska, U.; Basa, A.; Szymański, K. *Nukleonika* **2013,** *58,* 35.
26. Lu, L.; Zhang, W.; Wang, D.; Xu, X.; Miao, J.; Jiang, Y. *Mater. Lett.* **2010,** *64,* 1732. doi:10.1016/j.matlet.2010.04.025
27. al din Haratifar, E.; Shahverdi, H. R.; Shakibaie, M.; Moghaddam, K. M.; Amini, M.; Montazeri, H.; Shahvedi, A. R. *J. Nanomater.* **2009,** *2009,* No. 962021. doi:10.1155/2009/962021
28. Tombácz, E.; Illés, E.; Majzik, A.; Hajdú, A.; Rideg, N.; Szekeres, M. *Croat. Chem. Acta* **2007,** *80,* 503.
29. Mahadevan, S.; Gnanaprakash, G.; Philip, J.; Rao, B. P. C.; Jayakumar, T. *Physica E* **2007,** *39,* 20. doi:10.1016/j.physe.2006.12.041

30. Souza, F. L.; Lopes, K. P.; Nascente, P. A. P.; Leite, E. R. *Sol. Energy Mater. Sol. Cells* **2009,** *93,* 362–368. doi:10.1016/j.solmat.2008.11.049

31. Sinha, A.; Sharma, B. P. *Bull. Mater. Sci.* **2005,** *28,* 213. doi:10.1007/BF02711250

32. El Ghandoor, H.; Zidan, H. M.; Khalil, M. H. M.; Ismail, M. I. M. *Int. J. Electrochem. Sci.* **2012,** *7,* 5734–5745.

33. Tomaszewski, P. E. *Phase Transitions* **2013,** *86,* 260–266. doi:10.1080/01411594.2012.715301

34. Köse, H.; Aydin, A. O.; Akbulut, H. *Acta Phys. Pol., A* **2014,** *125,* 345. doi:10.12693/APhysPolA.125.345

35. Nasrazadani, S.; Raman, A. *Corros. Sci.* **1993,** *34,* 1335. doi:10.1016/0010-938X(93)90092-U

36. Balasubramaniama, R.; Ramesh, K. A. V. *Corros. Sci.* **2000,** *42,* 2085. doi:10.1016/S0010-938X(00)00045-7

37. Namduri, H.; Nasrazadani, S. *Corros. Sci.* **2008,** *50,* 2493. doi:10.1016/j.corsci.2008.06.034

38. Coates, J. Interpretation of Infrared Spectra, A Practical Approach. In *Encyclopedia of Analytical Chemistry;* Meyers, R. A., Ed.; John Wiley & Sons: Chichester, United Kingdom, 2000; pp 10815–10837. doi:10.1002/9780470027318.a5606

39. Kalska-Szostko, B.; Cydzik, M.; Satuła, D.; Giersig, M. *Acta Phys. Pol., A* **2011,** *119,* 15–17.

40. Goya, G. F.; Veith, M.; Rapalavicuite, R.; Shen, H.; Mathur, S. *Appl. Phys. A* **2005,** *80,* 1523. doi:10.1007/s00339-003-2381-4

41. Kalska, B.; Paggel, J. J.; Fumagalli, P.; Rybczyński, J.; Satula, D. *J. Appl. Phys.* **2004,** *95,* 1343. doi:10.1063/1.1637134

42. Kamali-M., S.; Ericsson, T.; Wäppling, R. *Thin Solid Films* **2006,** *515,* 721. doi:10.1016/j.tsf.2005.12.180

43. Satula, D.; Kalska-Szostko, B.; Szymanski, K.; Dobrzynski, L.; Kozubowski, J. *Acta Phys. Pol., A* **2008,** *114,* 1615.

44. Van Cromphaut, C.; de Resende, V. G.; De Grave, E.; Vandenberghe, R. E. *Hyperfine Interact.* **2009,** *190,* 143–148. doi:10.1007/s10751-009-9976-x

45. André-Filho, J.; León-Félix, L.; Coaquira, J. A. H.; Garg, V. K.; Oliveira, A. C. *Hyperfine Interact.* **2014,** *224,* 189. doi:10.1007/s10751-013-0850-5

46. Bødker, F.; Mørup, S. *Europhys. Lett.* **2000,** *52,* 217. doi:10.1209/epl/i2000-00426-2

47. Häggström, L.; Kamali, S.; Ericsson, T.; Nordblad, P.; Ahniyaz, A.; Bergström, L. *Hyperfine Interact.* **2008,** *183,* 49. doi:10.1007/s10751-008-9750-5

48. Mørup, S. *J. Magn. Magn. Mater.* **1983,** *37,* 39. doi:10.1016/0304-8853(83)90350-5

49. Kalska-Szostko, B.; Satuła, D.; Olszewski, W. *Curr. Appl. Phys.* **2015,** *15,* 226. doi:10.1016/j.cap.2014.12.011

Development of a novel nanoindentation technique by utilizing a dual-probe AFM system

Eyup Cinar[*1], Ferat Sahin[2] and Dalia Yablon[3]

Full Research Paper

Address:
[1]Microsystems Engineering, Rochester Institute of Technology, USA, [2]Electrical and Microelectronic Engineering, Rochester Institute of Technology, USA and [3]SurfaceChar LLC., Sharon, MA, USA

Email:
Eyup Cinar[*] - exc8020@rit.edu

* Corresponding author

Abstract

A novel instrumentation approach to nanoindentation is described that exhibits improved resolution and depth sensing. The approach is based on a multi-probe scanning probe microscopy (SPM) tool that utilizes tuning-fork based probes for both indentation and depth sensing. Unlike nanoindentation experiments performed with conventional AFM systems using beam-bounce technology, this technique incorporates a second probe system with an ultra-high resolution for depth sensing. The additional second probe measures only the vertical movement of the straight indenter attached to a tuning-fork probe with a high spring constant and it can also be used for AFM scanning to obtain an accurate profiling. Nanoindentation results are demonstrated on silicon, fused silica, and Corning Eagle Glass. The results show that this new approach is viable in terms of accurately characterizing mechanical properties of materials through nanoindentation with high accuracy, and it opens doors to many other exciting applications in the field of nanomechanical characterization.

Introduction

Nanoindentation is a commonly used technique to estimate mechanical properties of materials. An indenter probe fabricated with a known tip geometry is used to penetrate into the sample. By utilizing the force and small amount of depth information measured during indentation, material properties such as elastic (Young's) modulus of the sample can be estimated. For example, a growing application of nanoindentation is to determine the mechanical properties of cells which may be of critical importance for progressive diseases such as cancer or vascular diseases [1]. A recently published work by Guz et al.

also investigates nanoindentation experiments on cell mechanics and proposes new models for determining the elastic modulus of cells [2]. In addition to the biomedical engineering field, nanoindentation has been widely used in many other disciplines where accurate mechanical characterization is of high importance [3,4].

The improvement of sensor technology has enabled the integration of higher resolution depth and force measurement techniques for nanoindentation tools. Although this helped in increasing the accuracy of the experimental data, the current research demonstrates that there are still limitations on the commercially available tools and various problems still need to be tackled [5-8].

Nanoindentation experiments requiring very low force values and high resolution usually use a standard AFM system. With this setup, an AFM cantilever probe is used for indenting the material and the probe displacement is monitored by laser beam bounce technology also known as optical lever method. With this methodology, a laser beam is reflected off the back end of the cantilever and directed towards a quadrant photodiode detector that monitors both vertical and lateral motion [9]. Force–distance (FD) curves can be generated based on displacement data and the spring constant value of the cantilever. Depending on the type of the material, various models can be applied in order to interpret and extract the elastic modulus of materials.

One of the problems with this AFM-based approach is cantilever bending. Most of the conventional AFM nanoindentation probes have spring constants below 500 N/m. Depending on the material hardness, the applied load could result in bending of the cantilever. With optical lever method, the displacement is measured by laser deflection, which includes laser deflection caused by both the indentation depth (motion in Z) and the cantilever bending (motion in X and Y). The convolution of X and Y motion into the measurement cause overestimation errors in the interpretation of material properties using FD curves.

Instrumented nanoindentation (INI) tools can be used for a large dynamic force range. However, the displacement and force sensitivity are significantly low as compared to AFM-based nanoindentation. Cohen et al. compare the two techniques and present the drawbacks of INI tools in terms of load and displacement sensitivity [10]. While typical INI tools have a load sensitivity on the order of 10 nN, AFM-based nanoindentation can have sensitivities of 0.05 nN or better [10]. Similarly, displacement sensitivity of INI tools is significantly lower than the AFM-based tools. Especially when an INI tool is used, due to

the hardware limitations on both displacement and load sensing, the indenter probe might already have penetrated into the sample by the time surface contact is detected. This also yields critical errors in estimating the mechanical properties of materials as it was addressed in the literature by [6,8]. A final limitation in current AFM-based nanoindentation experiments is the use of lasers to monitor displacement data since there are various environments such as high vacuum or low temperature environments where the laser operation is complicated.

Considering the above mentioned problems, significant research has been devoted to the design and the development of tools that will improve the accuracy of the obtained experimental data and yield a more accurate estimation of material properties by nanoindentation. Evan et al. report the development of a tool specifically designed for nanoindentation on compliant materials considering the surface detection problems of commercially available nanoindentation devices [11]. Nowakowski et al. demonstrate a nanoindentation system with high precision where capacitive gauges are used for displacement measurement in the system [12]. The proximity of the indenter to the surface is sensed by tuning forks through their frequency response shift, showing the capabilities of accurate point of contact detection measurement of tuning forks. Oiko et al. recently demonstrated the development of nanoindentation probes that can be manipulated inside a scanning electron microscope (SEM) [13]. This system also utilizes tuning-fork technology, which can be used as an ultra-sensitive force sensor owing to the very high quality factors of tuning forks. They perform in situ nanoindentation experiments on multi-walled carbon nanotube bundles, however, the displacement data is only obtained from the SEM images limiting the high accuracy of displacement reading and the true depth sensing during nanoindentation. Zhao et al. present a nanoindentation device that is designed to operate inside an SEM chamber in order to perform in situ indentation tests of indium phosphide [14].

We report a novel approach using a multi-probe scanning probe microscopy (SPM) system with tuning-fork probe technology in an effort to overcome the limitations and problems of current high resolution nanoindentation systems such as AFM-based systems. Different than cantilever displacement measured by optical means, our approach uses a secondary AFM probe that is kept in closed-loop feedback contact with the indenter probe. This gives ultra-sensitive and high resolution capability in terms of true depth sensing during nanoindentation. With this approach, only the Z axis motion of the straight indenter is monitored, independent of any possible tuning fork bending that may occur in spite of the very large spring constant of tuning forks (above 4000 N/m). During nanoindentation of the specimen, the point of contact can be determined with great accuracy as

compared to other nanoindentation tools since the positioning of the tuning forks is controlled with phase feedback. This is also an advantage for the experimentally obtained data and overcomes the major problem as discussed in [6,8].

In our previous work [15], we have presented the initial results of our approach by employing dynamic force determination techniques only. In this study, we extend our work on multi-probe and apply it to estimation of elastic properties for different types of materials by measuring the bending of the indenter tuning fork with an another AFM probe.

The rest of the paper is organized as follows. Firstly, a theoretical background of nanoindentation is introduced to the reader. Then, an overview of the proposed system is demonstrated with a detailed component descriptions of the whole multi-probe system. In addition, the overall system calibration data and procedures are introduced. In the fourth section, the results of nanoindentation experiments obtained on multiple calibration materials are introduced and compared with other references in the literature. The last section is devoted to the conclusions.

Theoretical background on nanoindentation

A widely used mechanical model in nanoindentation experiments is the Oliver–Pharr (OP) model [16]. Properties such as elastic modulus or hardness of materials can be extracted from force–distance curves using the OP model. Figure 1a shows a typical force–distance curve when nanoindentation includes a plastic deformation. In this curve, the loading part includes both elastic and plastic deformation. However, during the unloading
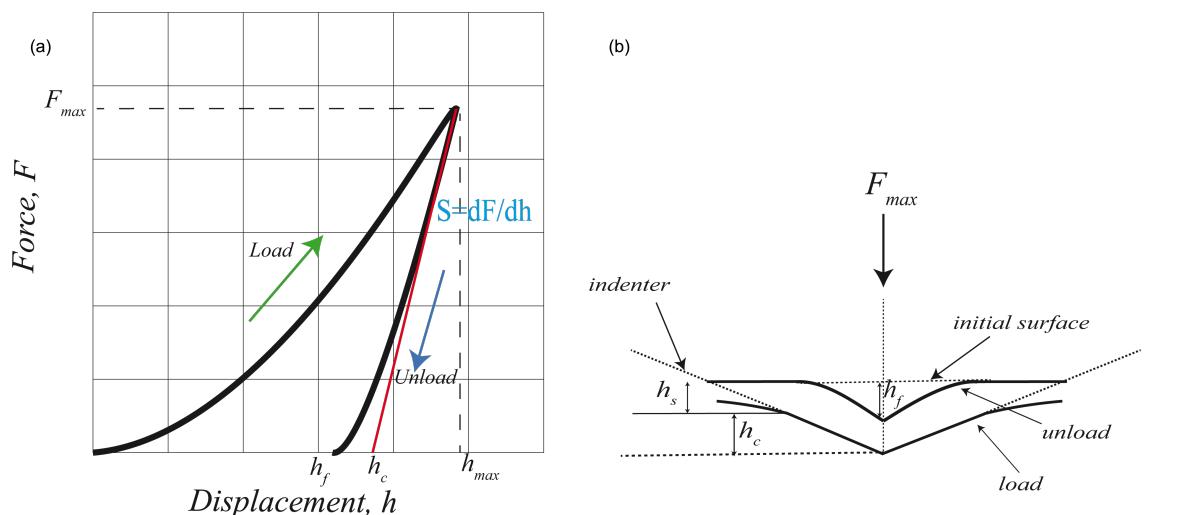
portion, it is assumed that only elastic deformation occurs. Therefore, stiffness can be approximated with the slope of unloading curve as shown in Figure 1a. If the unloading curve is fit to a power law such as $F = \alpha(h - h_f)^m$ where α and m are power-law fitting constants then the unloading stiffness S can be approximated as in Equation 1 by the slope of the fitting.

$$S = \frac{dF}{dh}\bigg|_{h=h_{max}} \tag{1}$$

Figure 1b shows the important parameters during the nanoindentation process. The depth at contact between indenter and substrate is h_c, h_s is the sink-in of the material during indentation and h_f is the final depth of penetration that is left on the surface after nanoindentation is completed. Once a force curve such as that in Figure 1a is obtained, one can calculate elastic unloading stiffness through Equation 2 defined as the slope of the upper part on the unloading curve as shown in Figure 1a:

$$S = \beta \frac{2E_{eff}\sqrt{A_c}}{\sqrt{\pi}}, \tag{2}$$

where E_{eff} is effective elastic modulus including both the elastic modulus of the indenter (E_1) and of the sample elastic modulus (E_2). It can be expressed as given in Equation 3. β is a correction factor that accounts for lack of axial symmetries for the indenter. It has been shown by Oliver and Pharr that $\beta \approx 1.07$ worked for most of the materials.

Figure 1: Schematic representation of the OP model. (a) A representative force–distance curve for the OP model; (b) Schematic illustrating loading and unloading process.

$$\frac{1}{E_{\text{eff}}} = \left(\frac{1 - \left(\nu_1 \right)^2}{E_1} + \frac{1 - \left(\nu_2 \right)^2}{E_2} \right) \qquad (3)$$
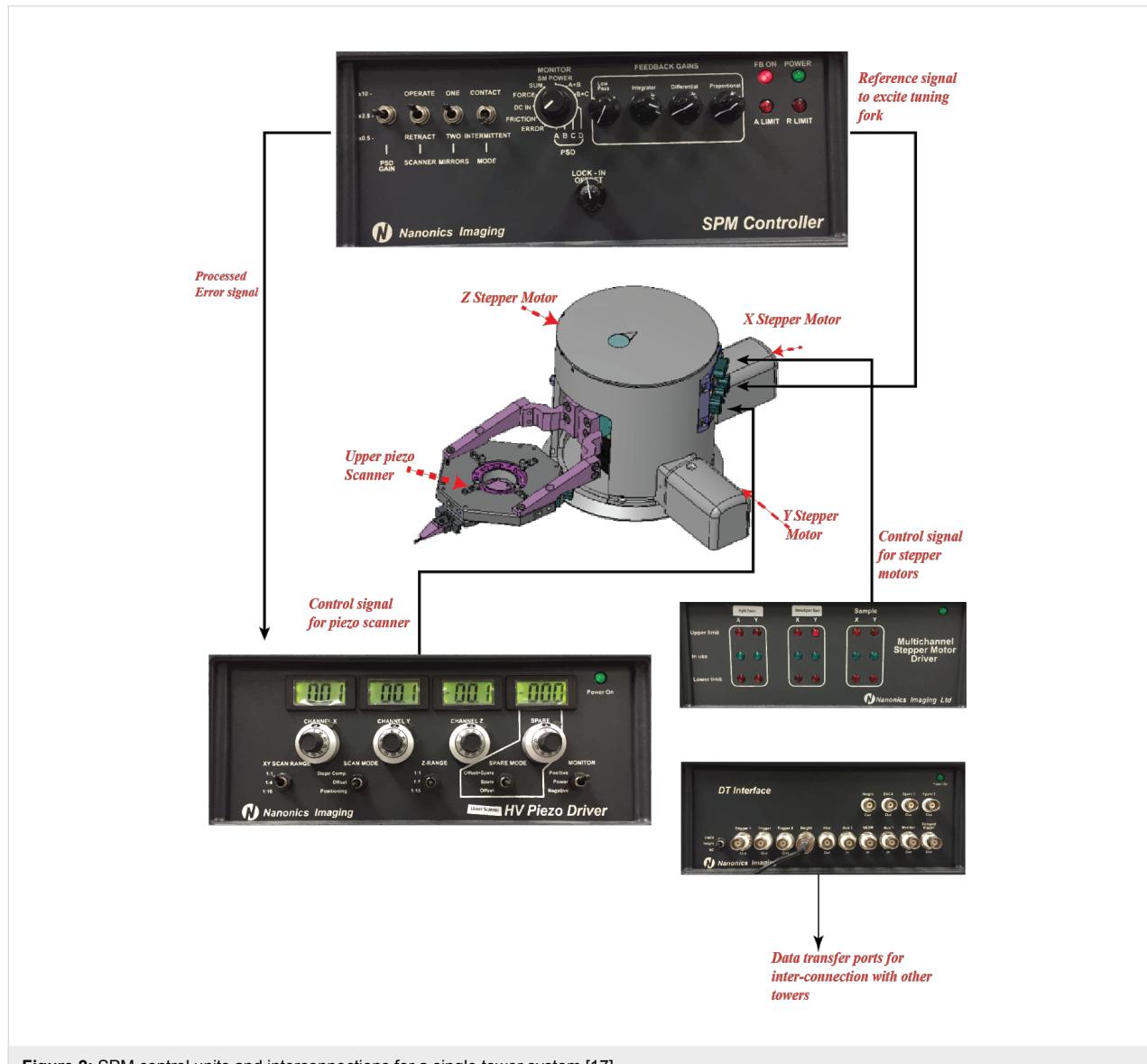
The projected contact area of elastic contact, A_c in Equation 2 depends on both indenter's tip geometry and the depth of contact, h_c. It is possible to establish a mathematical form for the area function such as $A_c(h_c)$ based on the specific tip geometry of the indenter.

Once a force–distance curve is obtained such as shown schematically in Figure 1a, one can calculate the stiffness parameter S from the slope of the unloading part and use Equation 2 and Equation 3 to extract the unknown elastic modulus of the sample (E_2).

In the next section we introduce an overview of the proposed system and its components in detail. We also present the calibration data and the parameters that have been used for the rest of the experimental results.

Overview of the novel multi-probe nanoindentation system

The proposed system uses a multi-probe SPM instrument (Nanonics MultiView-4000) based on normal force tuning fork technology. The tuning forks have a resonance frequency of approximately 34 kHz and a high Q factor in air that is over 1000. The instrument consists of four towers where each tower has lateral stepper motors for *XYZ* motion as shown in Figure 2 with a resolution of 21 nm. Each tower has also an upper piezo scanner integrated together with a pre-amplifier block, which

Figure 2: SPM control units and interconnections for a single tower system [17].
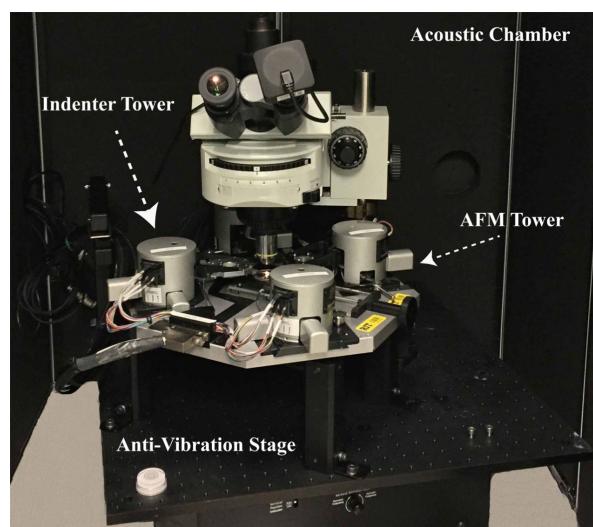
amplifies the signal received from the tuning fork. The upper piezo scanners are used for probe scanning and have a range of 80 μm (*XYZ*) and a resolution <0.05 nm in *Z* direction and <0.15 nm in the *XY* directions. In addition to the upper piezo scanners, there is also an independent lower piezo scanner that holds the sample holder and has a range of 80 μm in all directions.

The tuning fork is tuned to its resonance frequency, and either the oscillation amplitude or phase can be used for feedback. Based on the amplitude or phase feedback error, each tower can be independently controlled in a closed-loop feedback. The SPM controller box, shown in Figure 2, controls the feedback mechanism during a scan based on its lock-in amplifiers and PID controllers. Tuning forks are oscillated with 5 V amplitude signal and piezo scanners are controlled with high voltage signals (±145 V) generated by the high voltage (HV) piezo driver box shown in Figure 2. The oscillation frequency is based on the resonance frequency of each tuning fork. Based on the error signal obtained either through phase or amplitude feedback, the tip is moved so that a constant error signal is established that keeps the probe tip in continuous contact with the sample.

Data exchange between two towers can be established by using data transfer (DT) interface boxes shown in Figure 2 and BNC cables. These data transfer interface boxes provide the user interface for signal exchange (input/output) between data transfer digital acquisition (DAQ) cards of each tower. For example, the height information that is read from one tower can be transferred to the other tower through auxiliary input ports of the destination tower data transfer interface box. Each tower is connected to a separate PC that runs the proprietary control and
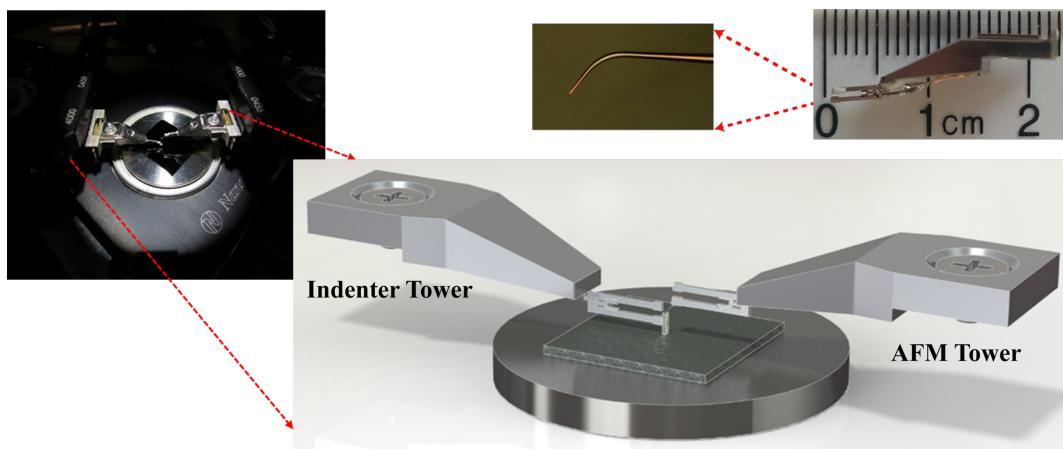
scanning software for the multi-probe AFM system. A detailed system analysis of the multi-probe SPM system is given in [17].

Figure 3 shows the positioning of multi-probe system. There are four towers and a sample piezo scanner stage which is positioned in the middle. Each tower can be operated independently. The towers and the scanners sit on an anti-vibration table and the entire setup is enclosed within an acoustic chamber to eliminate acoustic noise.

Figure 3: Positioning of the multi-probe system inside the acoustic chamber.

Figure 4 includes the details of the experimental setup demonstrating the multi-probe nanoindentation technique. For nanoin-

Figure 4: Experimental setup demonstrating the proposed two probe nanoindentation technique.
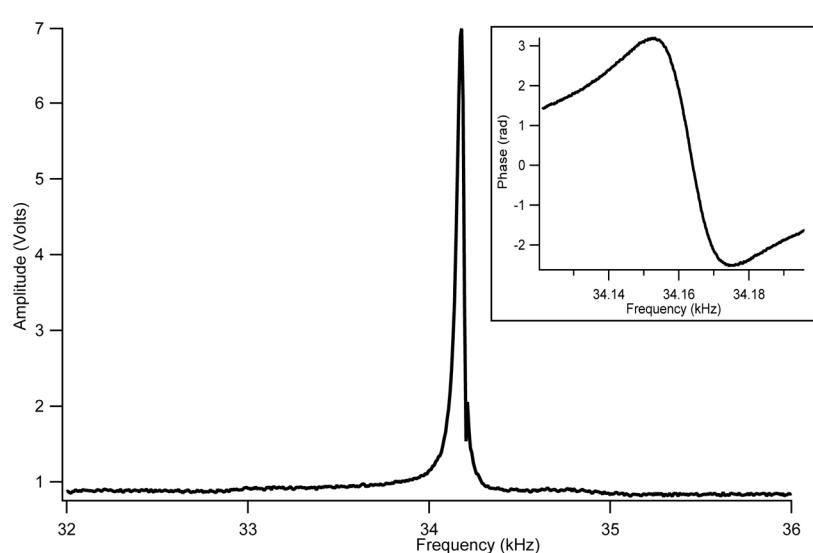
dentation experiments, a diamond probe with a cube-corner geometry (MicroStar Technologies) is mounted by Nanonics Imaging Ltd. (Jerusalem, Israel) so that there is no tilt of the indenter probe tip relative to the surface. During the mounting process of the indenter tip, a special mounting tool is used to mount the tip normal to the surface and accordingly guarantee the angle of the tip relative to the fork and the angle of the fork relative to the mount. Penetration depth is measured by the second tower with a specifically fabricated cantilevered AFM glass probe tips coated with Cr. These probes have a cantilever length of 300 μm and 20 nm tip radius, and they are mounted onto the lower tine of the tuning forks.

An example image of cantilevered AFM tips is also shown in Figure 4. The material under investigation is placed on a flat sample holder on the lower piezo scanner. Initially, the left hand side probe (indenter tower probe) is moved down towards the sample by the *Z* stepper motors while phase feedback error signal is monitored continuously. This means that the feedback is based on the change of the phase signal from the tuning fork. Contact of the tip with the sample is observed immediately with a change in error signal, at which point the stepper motion stops. Subsequently, the lower scanner is retracted by a safe distance amount (≈3 μm). After this, with the help of the fine movement capability of the piezo scanner, the sample is brought up automatically to ensure a very accurate contact positioning and a safe approach. Once the indenter probe is in feedback with the sample surface, the probe is held in that state and the second probe on the right hand side (AFM tower probe) is placed on top of the diamond probe. The positioning of the two probes is shown schematically in Figure 4. Once the contact is

established for both probes, the nanoindentation experiment is started.

For nanoindentation experiments, the indenter probe oscillation is disabled and the desired sample displacement value is set. For example, for a target of 100 nm displacement, the programmed sample scanner first retracts the sample 100 nm and then pushes toward the indenter probe for 200 nm. The displacement of the indenter is monitored with the AFM probe, which is oscillating and kept in phase-feedback. In our proposed system, the depth sensing is performed with an AFM probe which is in phase-feedback with the top of the diamond indenter probe. The height of the AFM probe is controlled with a piezo scanner head which has a very high resolution (<0.05 nm) due to highly oriented piezo materials used in the folded-piezo flexure scanner design. This also brings the ultimate resolution to our nanoindentation experiments in terms of depth sensing. In addition, since the AFM probe continuously monitors the Z-axis displacement of the indenter probe, only changes in Z motion are sensed with a very high accuracy of point of contact while the X and Y motion are ignored.

Figure 5 shows a representative AFM probe frequency–amplitude response curve with an inset including the change of phase over frequency. As the plots indicate, the tuning fork probes have a very sharp resonance curve enabling a sensitive error signal with accurate closed-loop feedback control. Depending on the application, it is possible to configure the system to be able to work in either amplitude or phase feedback error based on the oscillation of the tuning fork. Considering the rapid change of phase as shown in Figure 5, a phase feedback is more

Figure 5: An example resonance response of AFM probes used in the experiments.

sensitive compared to the amplitude feedback. With the help of a built-in lock-in amplifier system, it is possible to monitor both the amplitude and the phase of oscillations. When the phase feedback is used, the amplitude of oscillation can be independently monitored.

Calibration of the height signal is performed with a calibration grid (BudgetSensors) that includes both 115 nm micropillar and microwell arrays on a silicon chip. The step height of the features on the chip is measured and verified by using both contact profilometer and SEM measurements.

Figure 6 shows the data collected during a multi-probe indentation experiment on a fused silica sample. Initially, the diamond probe approaches the surface in phase feedback. When the contact is detected based on phase error signal, the approach is stopped automatically. The PID gains are then re-adjusted so that the error signal stays at zero with minimum deviation when the probe is in contact. After this, the approach of the AFM probe is initiated to the top of the indenter. Similarly to the indenter probe, the AFM probe is operated in phase-feedback mode. When contact is established with the indenter probe, the approach is stopped automatically and PID settings are adjusted so that the AFM probe will remain in contact at all times and will just follow the movement of the indenter. After the contact for both probes is established, the configuration of the stage movement in the software is performed. In Figure 6, the stage is programmed to move ±400 nm. When the indentation process is started, the stage retracts 400 nm first and then moves towards to the indenter. During the motion of the sample stage towards
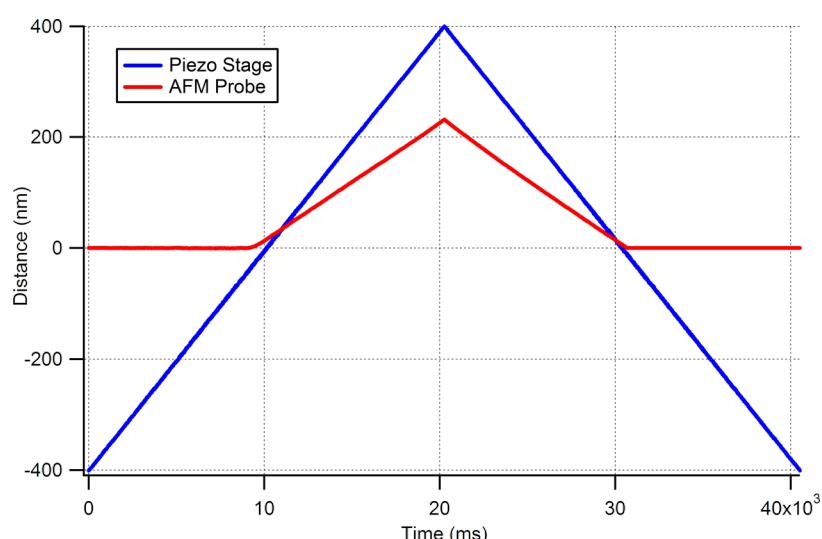
the indenter, the indenter probe oscillations are turned off and the indenter probe is no longer in feedback. The second set of data in red shown in Figure 6 is the displacement data read from the AFM probe during the indentation process. Note that the AFM probe reflects only the true Z axis movement of the indenter probe unlike the conventional AFM systems where the measurement relies on laser deflection of the cantilever itself which includes a convolution of X and Y motion into the laser deflection reading.

As it can be seen from Figure 6, as the piezo stage starts pushing up the sample towards the diamond indenter, the reading of the AFM probe starts to go up as well and when the sample starts moving away from the diamond tip, the AFM probe reading starts going down and settles at position zero when the sample and the indenter are totaly dissociated.

For the force level calculations, the spring constant of the tuning fork can be calculated from the beam formula as given in Equation 4:

$$k_{\text{beam}} = E_{\text{quartz}} \frac{w}{4} \left(\frac{t}{L} \right)^3 , \qquad (4)$$

where w and t are the width and the thickness of the free prong, respectively and L is the length of the prong. E_{quartz} is elastic modulus of the quartz material of which the tuning forks are fabricated. Several studies have found this formula to be inaccurate and underestimate the spring constant of the tuning forks by

Figure 6: Experimental data showing AFM probe measurements on top of the diamond indenter for a fused silica sample.

a significant amount, even up to an order of magnitude [18,19]. One reason for this is that the tip (diamond indenter in our case) is rigidly fixed at the end by epoxy glue and this might alter the effective dimensions of the free beam. Therefore, further investigation of the spring constant calculation based on this model is necessary.

We derive the effective spring constant of the indenter tuning fork by calibrating against a sample with known modulus. Based on the formula given in Equation 4 and the dimensions of a bare tuning fork, the spring constant is calculated as 2600 N/m. Firstly, an indentation experiment is performed on fused silica by using $k_{fork} = 2600$ N/m. Then, Oliver–Pharr (OP) model is utilized to match the experimental data to the known elastic modulus of fused-silica sample 69.3 GPa [16,20]. Fitting of the data over 10 different force-curve measurements with an average modulus of 69.38 GPa yields a spring constant $k_{fork} = 4992 \pm 264.11$ N/m. One of the force–distance curves used in OP model fitting is given in Figure 7.

Table 1 tabulates the results of the calibration experiment on the fused silica sample. Where h_{max} represents the maximum depth of penetration and $K_{calibration}$ is the spring constant value of the indenter tuning fork.
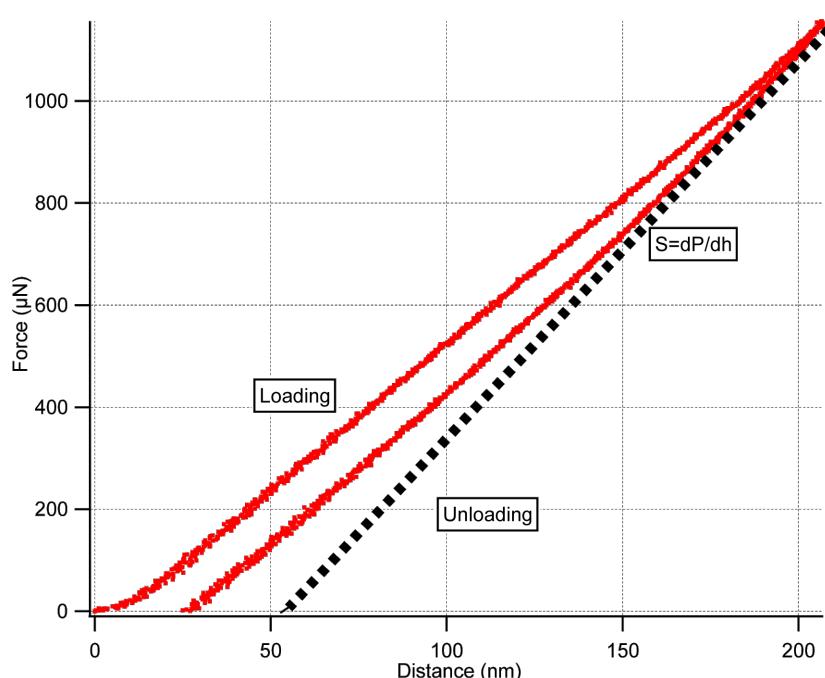
Figure 8 demonstrates the distribution of spring constant values with respect to depth of penetration during fused silica calibra-

Table 1: Experimental data obtained during calibration of k_{fork} on the fused silica calibration sample.
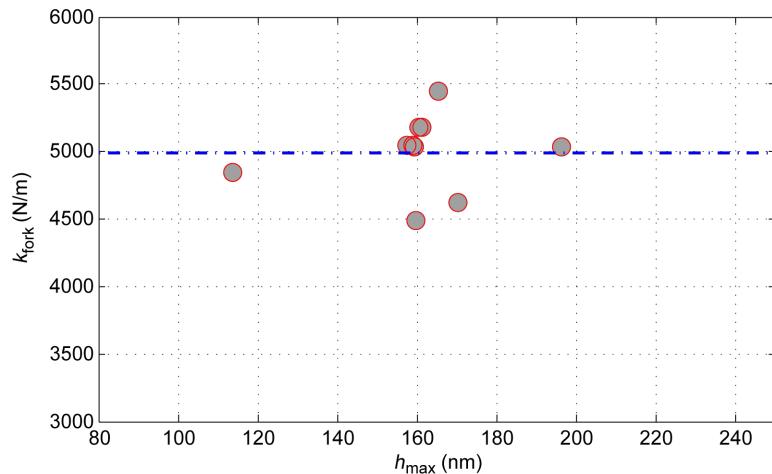
h_{max} (nm)	$K_{calibration}$ (N/m)	estimated modulus (GPa)
113.8	4850	69.6
157.6	5041	69.32
159	5041	69.47
159.4	5034	69.32
159.9	4490	69.38
160.6	5180	69.31
161.3	5175	69.29
165.5	5450	69.35
170.3	4620	69.4
206.98	5035	69.35
mean (std)	4992 (±264.11)	69.38 (±0.09)

tion experiments. The mean value of the spring constant is shown with a dotted line at 4992 N/m.
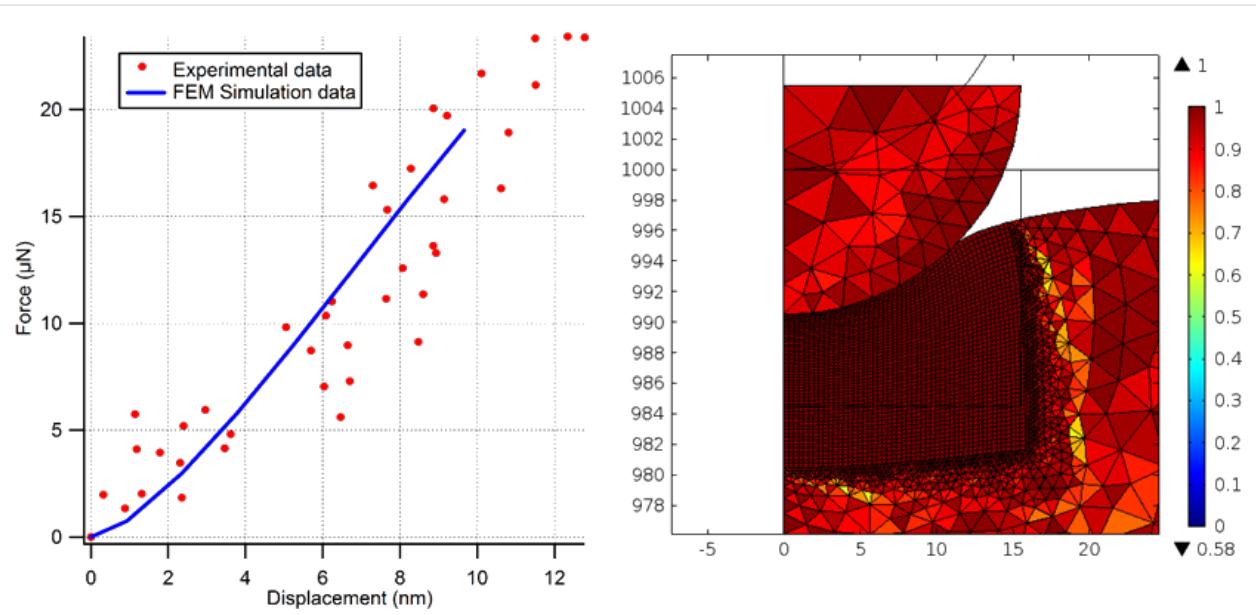
To further verify the spring constant calibration and the force values for the rest of the experiments, finite element (FE) simulations have been performed as shown in Figure 9. In the simulations, the diamond indenter is pressed into the fused silica reference sample incrementally up to 10 nm depth of penetration in order to ensure that the results stay within the elastic

Figure 7: Fused silica force–distance curve.

Figure 8: Spring constant vs maximum depth of penetration.

Figure 9: Finite element analysis data as compared to experimental data.
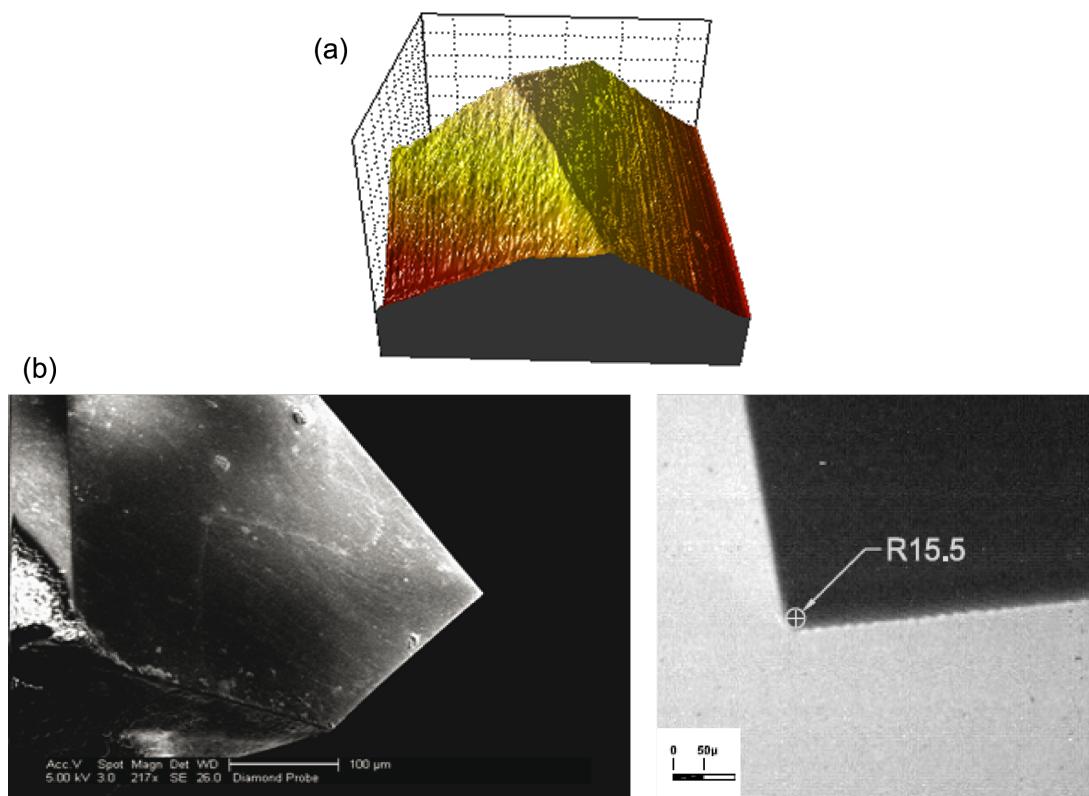
regime. During the simulation, reaction forces on the surface of the indenter tip are evaluated showing that force levels for both experimental and simulation data are in excellent agreement when k_{fork} is 4992 N/m.

Figure 10a shows the characteristics of the cube-corner geometry diamond indenter tip used in our nanoindentation experiments. Figure 10a is obtained from an AFM scanning with the AFM tower and shows the cube-corner shape of the tip. Figure 10b is an TEM image of the tip showing the radius of curvature in nanometers.

In the next section, we present the results obtained with other types of materials and our analysis of elastic modulus estimations showing the viability and the reproducibility of the proposed technique.

Results and Discussion
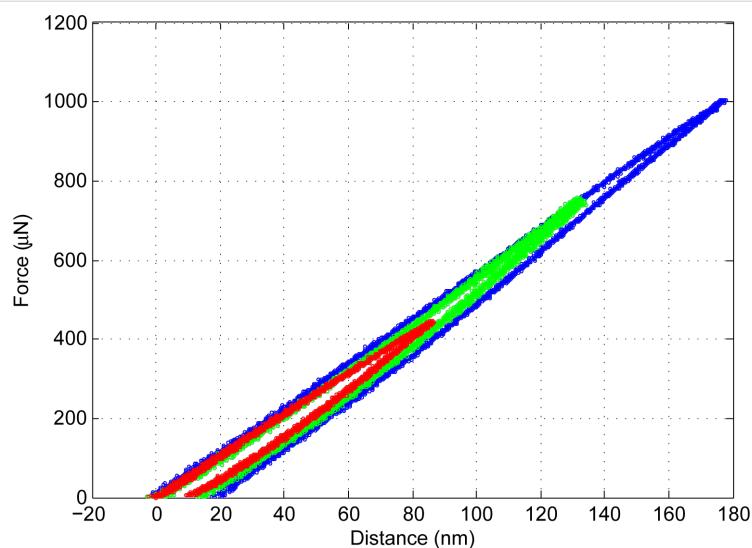
In the previous section, we have introduced the overall system components and the details of our proposed technique together with the calibration results. In this section, we present the nanoindentation results on different materials and our estimations based on the experimentally obtained data.

Figure 10: Images of cube-corner diamond tip used in nanoindentation experiments. (a) A 3D representation of AFM scan for the cube-corner diamond tip used in nanoindentation experiments. (b) SEM and TEM images of the diamond tip. The tip radius is measured as 15.5 nm.

Figure 11 includes the force–distance curves with varying loads measured on silicon (100). The varying loads correspond to the programmed stage movements from 100 to 300 nm. Within these experiments, the stage moves with a speed of 0.04 nm/ms. The maximum force increases from 445 to 1004 µN.

An AFM topographical image of indentation on silicon substrate is shown in Figure 12 together with its height profile. It shows quantitatively a residual indentation mark of the cube-corner indenter tip at a depth of 27.5 nm. The overlapping pattern of force–distance curves together with the residual cube-

Figure 11: Force–distance curves on silicon substrate.

corner tip indentation mark normal to the surface show the effectiveness of our technique with negligible probe twisting artifacts.

Table 2 shows the properties of the materials used in nanoindentation experiments in our study and their corresponding material properties reported in the literature.
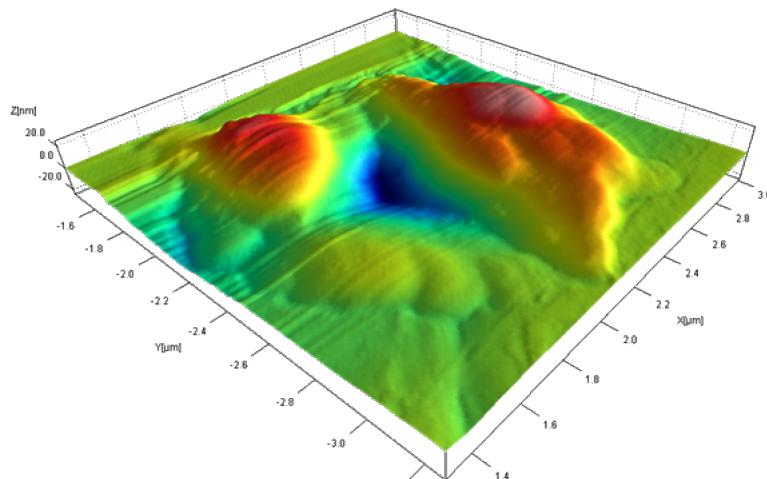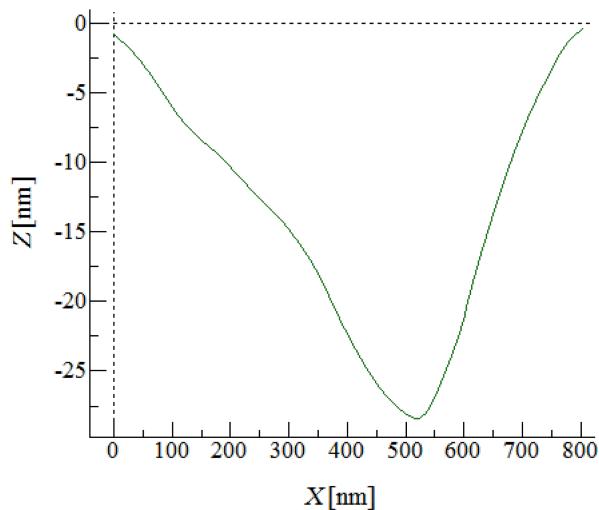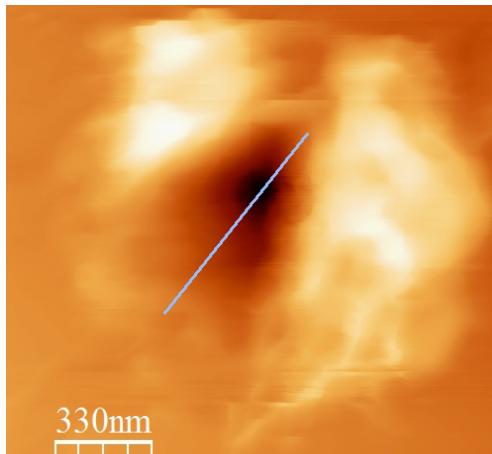
Table 2: Reported properties of the materials used in nanoindentation experiments.

material	E (GPa)	Poisson ratio	reference
Si(100)	169	0.22	[21]
fused silica	69.3	0.17	[20]
Eagle Glass™	70.9	0.23	[22]
diamond (tip)	1150	0.07	[16]

Figure 13 shows the nanoindentation results on a glass substrate (Corning® Eagle Glass 2000™) with an elastic modulus of 70.9 GPa and varying load conditions similar to silicon nanoindentation experiments.

Figure 14 shows an example of a power-law fitting of the unloading data from a experimentally obtained silicon force–distance curve. The fitting parameters $\alpha = 0.6668$ and $m = 1.4668$ fall within the expected ranges as listed in the OP model [16].

In our calculations, the area function is taken as $A(h_c) = 2.598001h_c^2$. This is based on considerations about physical measurements on the tip and the geometric calculations of the cube-corner indenter as suggested by the manufacturer's data sheet of the diamond-tip.

Figure 12: Topography and cross-sectional profile of indent on silicon.
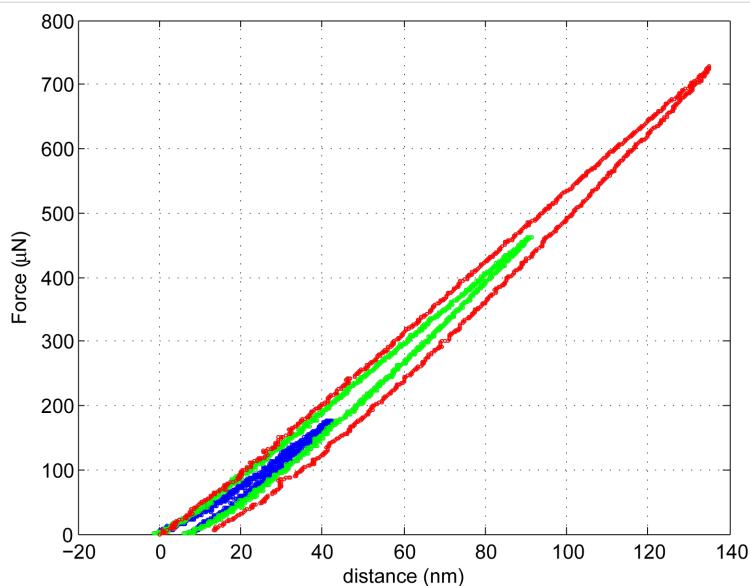
Figure 13: Force–distance curves on Corning Eagle Glass substrate.
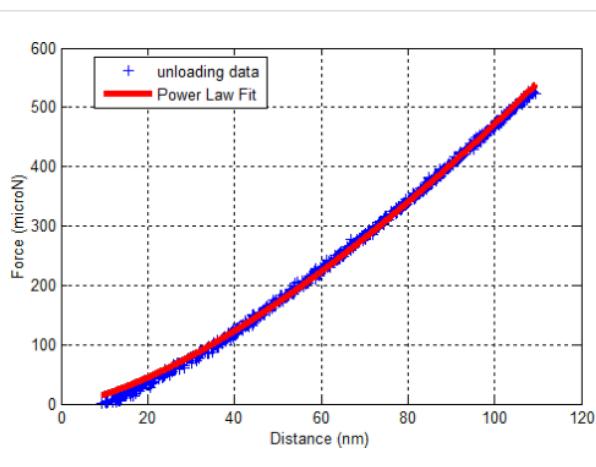
Figure 14: Power-law fitting to the unloading part of a silicon force–distance curve.

The results in Table 3 present the experimentally obtained elastic modulus estimations of the materials used in this study. Mean values are taken over ten different set of experiments for each sample at varying load levels. Compared to reported moduli values in the literature, the values shown in Table 3 are in a good agreement.

Conclusion

We present the development of a novel approach to nanoindentation by using a multi-probe SPM system. The new approach brings ultra-high resolution to nanoindentation experiments in terms of both the force and depth sensing. The second AFM probe monitors only the true *Z* axis motion as the straight indenter probe is lifted in the *Z* direction. This is a significant improvement over conventional AFM-based nanoindentation experiments that convolute *XY* motion into *Z* motion with laser-based detection of cantilever motion. Additionally, the use of a tuning fork gives excellent force sensitivity due to its significantly higher spring constant, quality factor, and ability to track motion through phase feedback. Our experimental results show that this system measures the material properties, accurately.

In addition to an indenter probe and an AFM probe, with the current system up to four probes can be operated and could work in tandem. This opportunity brings other exciting novel applications to our nanoindentation approach. For example, while the two probes are performing a nanoindentation experiment, the third and the forth probe can be used in identifying changes in other material properties on-line. By attaching a conductive Pt nanowire probe tips, the third probe can be used

Table 3: Estimation of elastic modulus by Oliver–Pharr fitting and the parameters used.

materials	estimated modulus (GPa)	reported modulus (GPa)	Oliver–Pharr β parameter
Si (100)	166.87 ± 27.42	169	1.04
fused Silica	69.38 ± 0.09	69.3	1.04
Eagle Glass	67.83 ± 7.68	70.9	1.04

as a voltage source and the fourth probe can be used to measure the current. In this way, electrical nano-characterization of the sample can be performed on-line during nanoindentation. Furthermore, thermoresistive probes can be integrated into the approach to monitor the thermal properties of the material on-line during nanoindentation. Lastly, this novel approach can be integrated into environments where the usage of lasers is not possible such as the case in conventional AFM nanoindentation experiments.

Acknowledgements

References

1. Cross, S. E.; Jin, Y.-S.; Rao, J.; Gimzewski, J. K. *Nat. Nanotechnol.* **2007,** *2,* 780–783. doi:10.1038/nnano.2007.388
2. Guz, N.; Dokukin, M.; Kalaparthi, V.; Sokolov, I. *Biophys. J.* **2014,** *107,* 564–575. doi:10.1016/j.bpj.2014.06.033
3. Díez-Pascual, A. M.; Gómez-Fatou, M. A.; Ania, F.; Flores, A. *Prog. Mater. Sci.* **2015,** *67,* 1–94. doi:10.1016/j.pmatsci.2014.06.002
4. Paul, W.; Oliver, D.; Miyahara, Y.; Grütter, P. H. *Phys. Rev. Lett.* **2013,** *110,* 135506. doi:10.1103/PhysRevLett.110.135506
5. Dokukin, M. E.; Sokolov, I. *Macromolecules* **2012,** *45,* 4277–4288. doi:10.1021/ma202600b
6. Kaufman, J. D.; Klapperich, C. M. *J. Mech. Behav. Biomed. Mater.* **2009,** *2,* 312–317. doi:10.1016/j.jmbbm.2008.08.004
7. Ren, J.; Zou, Q. *IEEE Trans. Nanotechnol.* **2014,** *13,* 46–54. doi:10.1109/TNANO.2013.2287505
8. Crick, S. L.; Yin, F. C.-P. *Biomech. Model. Mechanobiol.* **2006,** *6,* 199–210. doi:10.1007/s10237-006-0046-x
9. Meyer, G.; Amer, N. M. *Appl. Phys. Lett.* **1988,** *53,* 1045–1047. doi:10.1063/1.100061
10. Cohen, S. R.; Kalfon-Cohen, E. *Beilstein J. Nanotechnol.* **2013,** *4,* 815–833. doi:10.3762/bjnano.4.93
11. Evans, D. W.; Vavalle, N. A.; DeVita, R.; Rajagopalan, P.; Sparks, J. L. *Exp. Mech.* **2012,** *53,* 217–229. doi:10.1007/s11340-012-9618-0
12. Nowakowski, B. K.; Smith, D. T.; Smith, S. T.; Correa, L. F.; Cook, R. F. *Rev. Sci. Instrum.* **2013,** *84,* 075110. doi:10.1063/1.4811195
13. Oiko, V. T. A.; Martins, B. V. C.; Silva, P. C.; Rodrigues, V.; Ugarte, D. *Rev. Sci. Instrum.* **2014,** *85,* 035003. doi:10.1063/1.4868236
14. Huang, H.; Zhao, H.; Mi, J.; Yang, J.; Wan, S.; Xu, L.; Ma, Z. *AIP Adv.* **2012,** *2,* 012104. doi:10.1063/1.3676691
15. Cinar, E.; Sahin, F. New approach for nanoindentation using multiprobe AFM system. In *Nanotechnology (IEEE-NANO), Proc. of 2014 IEEE 14th International Conference on,* 2014; pp 49–53.
16. Oliver, W. C.; Pharr, G. M. *J. Mater. Res.* **2004,** *19,* 3–20. doi:10.1557/jmr.2004.19.1.3
17. Cinar, E.; Sahin, F. A system of systems analysis of a multi-probe SPM system. In *System of Systems Engineering Conference (SoSE), 2015 10th,* 2015; pp 117–121.
18. Qin, Y.; Reifenberger, R. *Rev. Sci. Instrum.* **2007,** *78,* 063704. doi:10.1063/1.2743166
19. Falter, J.; Stiefermann, M.; Langewisch, G.; Schurig, P.; Hölscher, H.; Fuchs, H.; Schirmeisen, A. *Beilstein J. Nanotechnol.* **2014,** *5,* 507–516. doi:10.3762/bjnano.5.59
20. Sansoz, F.; Gang, T. *Ultramicroscopy* **2010,** *111,* 11–19. doi:10.1016/j.ultramic.2010.09.012
21. Hopcroft, M. A.; Nix, W. D.; Kenny, T. W. *J. Microelectromech. Syst.* **2010,** *19,* 229–238. doi:10.1109/JMEMS.2009.2039697
22. Corning Ltd Eagle Glass 2000 Material Information. http://www.corning.com (accessed Feb 3, 2015).

Free vibration of functionally graded carbon-nanotube-reinforced composite plates with cutout

Mostafa Mirzaei[1] and Yaser Kiani[*2,§]

Abstract

During the past five years, it has been shown that carbon nanotubes act as an exceptional reinforcement for composites. For this reason, a large number of investigations have been devoted to analysis of fundamental, structural behavior of solid structures made of carbon-nanotube-reinforced composites (CNTRC). The present research, as an extension of the available works on the vibration analysis of CNTRC structures, examines the free vibration characteristics of plates containing a cutout that are reinforced with uniform or nonuniform distribution of carbon nanotubes. The first-order shear deformation plate theory is used to estimate the kinematics of the plate. The solution method is based on the Ritz method with Chebyshev basis polynomials. Such a solution method is suitable for arbitrary in-plane and out-of-plane boundary conditions of the plate. It is shown that through a functionally graded distribution of carbon nanotubes across the thickness of the plate, the fundamental frequency of a rectangular plate with or without a cutout may be enhanced. Furthermore, the frequencies are highly dependent on the volume fraction of carbon nanotubes and may be increased upon using more carbon nanotubes as reinforcement.

Introduction

Plates with cutouts are extensively used in automotive and aircraft structures. Cutouts may be of rectangular, circular, elliptical, super elliptical or polygonal shape. Due to the complicated configuration of a plate with a cutout, there is significantly less research on plates with cutouts in comparison to those without cut-out. Depending on the application, homogeneous isotropic, composite or functionally graded plates may be perforated to fulfill a desired application.

Representing a type of novel material with fascinating electro-thermo-mechanical properties, carbon nanotubes (CNTs) have attracted increasing attention in the past decades. CNTs are a

promising candidate for the reinforcement of the matrix phase in a composite. Kwon et al. [1] reported that using a powder metallurgy fabrication process, carbon-nanotube-reinforced composites (CNTRCs) may be achieved with a nonuniform distribution of CNTs through the media. This type of reinforced composite media is known as functionally graded carbon-nanotube-reinforced composite (FG-CNTRC). An overview on the properties, modeling and characteristics of FG-CNTRC beams, plates and shells is provided by Liew et al. [2]

It has been shown that the bending moment may be significantly alleviated through a functionally graded distribution of CNTs in a polymeric matrix [3]. In the five years following the discovery of this interesting feature, various investigations were reported on the mechanics of FG-CNTRC structures.

Zhu et al. [4] investigated the free vibration and static response of FG-CNTRC plates using finite element method [4]. Zhang et al. investigated the free vibration characteristics of FG-CNTRC skew plates [5], triangular plates [6] and cylindrical panels [7] using element free methods. In these works it is shown that the natural frequencies of plates and panels are affected by the distribution and volume fraction of CNTs. Zhang et al. [8] investigated the free vibration characteristics of FG-CNTRC plates resting on an elastic foundation. Lei et al. [9] investigated the free vibration of composite, laminated FG-CNTRC plates with general boundary conditions. Malekzadeh and Zarei [10] examined the free vibration characteristics of laminated plates containing FG-CNTRC layers in an arbitrary straight-sided quadrilateral shape. Malekzadeh and Heydarpour [11] investigated the free vibration and static response of laminated plates with FG-CNTRC layers using a mixed Navier-layerwise differential quadrature method. In this research, plates with all edges simply supported are considered. Natarajan et al. [12] applied a higher order shear and normal deformable plate formulation to study the static and free vibrations of single layer FG-CNTRC plates and also sandwich plates with FG-CNTRC face sheets. Wang and Shen investigated the linear and nonlinear free vibrations of a single layer FG-CNTRC plate [13] and also sandwich plates with stiff core and FG-CNTRC face sheets [14]. In this analysis, the interaction of the plate with a two parameter elastic foundation is also taken into account. Wang and Shen [15] investigated the dynamic response of FG-CNTRC plates according to the von Kármán formulation. In this research, the interaction of a two parameter elastic foundation and a thermal environment are also included. The solution method of this research is based on a two-step perturbation technique and is suitable for plates with all edges simply supported. Using a mesh-free formulation proper for arbitrary edge supports, Lei et al. [16] investigated the elasto-dynamic response of FG-CNTRC plates subjected to sudden lateral pressure. For more investigations on vibration,
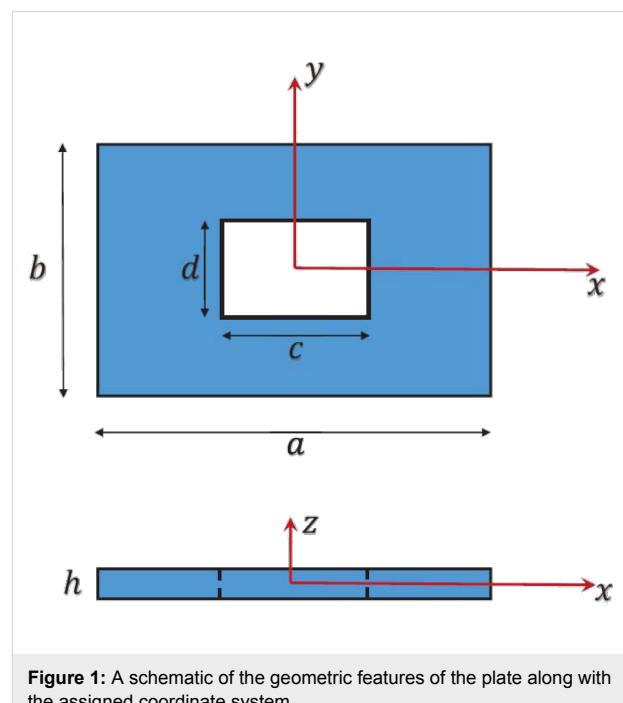
buckling, postbuckling, stress analysis, and nonlinear bending of FG-CNTRC plates, one may refer to [17-25].

The present research aims to investigate the free vibration characteristics of an FG-CNTRC rectangular plate containing a central, rectangular cutout. The distribution of CNTs across the plate thickness are assumed to be either uniform or nonuniform. A modified rule of mixtures approach is used to obtain the properties of the composite media. Chebyshev polynomials are used as the basic shape functions of the Ritz formulation to construct an eigenvalue problem. The solution method may be used for perforated FG-CNTRC rectangular plates with arbitrary boundary conditions on the outer edges, while the inner edges are unconstrained. The numerical results allow for the study of the volume fraction and distribution pattern of CNTs, plate boundary conditions and hole size.

Modeling
Basic formulation
A rectangular-shaped plate, made of a polymeric matrix, reinforced by CNTs whose distribution may be nonuniform, is considered in the present research. The plate contains a centered hole, which is assumed to be rectangular-shaped. The cartesian coordinate system is assigned to the center of the mid-surface of the plate. In this system, the plate occupies the domain $[-0.5a\ 0.5a] \times [-0.5b\ 0.5b] \times [-0.5h\ 0.5h]$. The hole occupies the domain $[-0.5c\ 0.5c] \times [-0.5d\ 0.5d] \times [-0.5h\ 0.5h]$. The dimensions of the plate with the assigned coordinate system are demonstrated in Figure 1.

Figure 1: A schematic of the geometric features of the plate along with the assigned coordinate system.

Motivated by the fundamental research of Shen [3], many investigators take into account the functionally graded distribution of the volume fraction of reinforcements through the matrix. Consistent with the possible fabrication processes for plates, three different functionally graded types of CNT dispersion profiles may be assumed and are considered in the present research: FG-V, FG-O and FG-X [5-7]. A schematic of these functionally graded types along with the uniformly distributed (UD) type are shown in Figure 2.
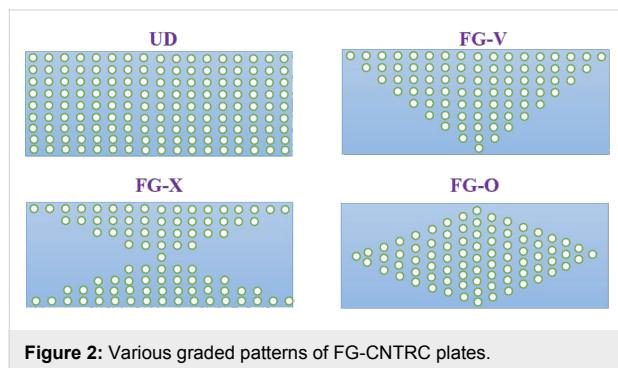
Figure 2: Various graded patterns of FG-CNTRC plates.

The properties of a composite media (i.e., a matrix reinforced with CNTs) may be obtained according to various homogenization techniques. The two commonly used schemes that are extensively used for composites and FGMs are the Mori–Tanaka scheme [26] and the rule of mixtures [27]. The conventional rule of mixtures has the advantage of simplicity; however, when using CNTRCs, this approach does not provide an accurate estimation of the mechanical properties of the media. Meanwhile, as explained by Shen [3] and used extensively by other researchers [28-32], the conventional rule of mixtures approach may be modified with the introduction of the efficiency parameters. Under such modification, Young's modulus and the shear modulus of the composite media take the form:

$$
\begin{aligned}
E_{11} &= \eta_1 V_{CN} E_{11}^{CN} + V_m E^m \\
\frac{\eta_2}{E_{22}} &= \frac{V_{CN}}{E_{22}^{CN}} + \frac{V_m}{E^m} \\
\frac{\eta_3}{G_{12}} &= \frac{V_{CN}}{G_{12}^{CN}} + \frac{V_m}{G^m}.
\end{aligned}
\tag{1}
$$

In this formula, the properties of the CNT are denoted by a superscript CN and that those belong to matrix are denoted by a superscript m. Following the classical solid mechanics notation, E and G are the elastic modulus and shear modulus of the constituents, respectively. In comparison to the conventional rule of mixtures approach, three unknown constants, η_1, η_2 and η_3, are introduced in Equation 1; these are known as efficiency

parameters. These parameters compensate for the errors generated due to the conventional rule of mixtures approach for a CNTRC. The values of these constants are obtained by matching the data obtained according to the above formula with those obtained based on the molecular dynamics simulation.

It is worth noting that the volume fraction of CNTs and polymeric matrix are denoted by V_{CN} and V_m, respectively. According to the partition of unity property, the following condition should be satisfied at each point of the composite media: $V_{CN} + V_m = 1$.

The volume fraction of CNTs is assumed to be either nonuniform or uniform across the plate thickness. According to the above rule, the volume fraction of matrix may also be achieved and the overall properties of the media may be calculated according to Equation 1. Table 1 presents the dispersion profile of V_{CN} as a function of the thickness coordinate for each of the UD CNTRC or FG-CNTRC rectangular plates.

Table 1: Volume fraction of CNTs as a function of the thickness coordinate for various CNT distributions [28-34].

CNT Distribution	V_{CN}
UD CNTRC	V_{CN}^*
FG-V CNTRC	$V_{CN}^*\left(1+2\dfrac{z}{h}\right)$
FG-O CNTRC	$2V_{CN}^*\left(1-2\dfrac{\lvert z\rvert}{h}\right)$
FG-X CNTRC	$4V_{CN}^*\dfrac{\lvert z\rvert}{h}$

Upon evaluation of the total volume fraction of CNTs across the plate thickness, it is revealed that all types have the same total volume fraction of CNTs, that is, V_{CN}^*. Consequently, the vibrational characteristics of FG-CNTRC and UD-CNTRC rectangular plates may be compared with respect to each other. As previously shown in Figure 2 and the information in Table 1, given an FG-X pattern of CNT dispersion, the mid-surface of the plate is free of CNTs while the top and bottom surfaces have the maximum volume fraction of CNTs. The volume fraction of CNTs increases linearly from the mid-plane to the free surfaces of the plate. The FG-O type of distribution pattern is the inverse of the FG-X case. In the FG-O distribution, the top and bottom surfaces are free of CNTs and the mid-surface has the maximum volume fraction of CNTs. In FG-V type, the bottom surface is free of CNTs and the top has the maximum volume fraction of CNTs. Unlike these three types, in the UD case, each surface of the plate has the same volume fraction of CNTs.

Similar to the shear modulus and Young's modulus, Poisson's ratio and the mass density of the composite media may be written in terms of belongings to the CNT and matrix. As claimed by Shen [28], and as used also by other researchers [29], Poisson's ratio depends weakly on position and consequently may be obtained as

$$\nu_{12} = V_{CN}^{*} \nu_{12}^{CN} + V_{m} \nu^{m}. \tag{2}$$

The mass density of a CNTRC media may be obtained according to the conventional rule of mixtures approach [13,14]. Therefore, as a function of volume fraction and mass density of constituents, ρ^{CN} and ρ^{m}, one may write

$$\rho = V_{CN} \rho^{CN} + V_{m} \rho^{m}. \tag{3}$$

Upon evaluation of the mass fraction for each of the graded patterns of CNTs, it is concluded that each type has the same mass fraction of CNTs.

Flexural theories propose an approximate function for the in-plane and out-of-plane displacement components of the plate. The most simple flexural theory is the classical plate theory, which eliminates the transverse shear strain components as well as the normal strain component. These assumptions are exaggerated for moderately thick composites and therefore classical plate theory results in erroneous results for the structural response of a CNTRC rectangular plate. On the other hand, first order shear deformation plate theory (FSDT), which takes into account the constant transverse shear strain, results in accurate results for the global properties of moderately thick CNTRC plates. This is because it takes into account both the rotary inertias and through-the-thickness shear strains [35]. This research is also developed based on FSDT, which estimates the displacements of the plate in terms of those of the mid-surface and the cross-section rotations as

$$
\begin{aligned}
u(x, y, z, t) &= u_0(x, y, t) + z\varphi_x(x, y, t) \\
v(x, y, z, t) &= v_0(x, y, t) + z\varphi_y(x, y, t) \\
w(x, y, z, t) &= w_0(x, y, t).
\end{aligned}
\tag{4}
$$

In Equation 4, the subscript zero indicates the characteristics of the mid-plane. Rotations of the cross-sectional elements about the *x* and *y* axes are denoted by φ_y and φ_x. Additionally, displacements along the *x*, *y* and *z* directions are shown by *u*, *v* and *w*.

The substitution of Equation 4 into the strain–displacement relations results in the components of strain on an arbitrary point of the plate in terms of mid-surface strain components and change in curvature as

$$
\begin{Bmatrix}
\varepsilon_{xx} \\
\varepsilon_{yy} \\
\gamma_{xy} \\
\gamma_{xz} \\
\gamma_{yz}
\end{Bmatrix}
=
\begin{Bmatrix}
\varepsilon_{xx0} \\
\varepsilon_{yy0} \\
\gamma_{xy0} \\
\gamma_{xz0} \\
\gamma_{yz0}
\end{Bmatrix}
+ z
\begin{Bmatrix}
\kappa_{xx} \\
\kappa_{yy} \\
\kappa_{xy} \\
\kappa_{xz} \\
\kappa_{yz}
\end{Bmatrix}.
\tag{5}
$$

The strain field on the midsurface of the plate may be obtained according to the midsurface displacements as

$$
\begin{Bmatrix}
\varepsilon_{xx0} \\
\varepsilon_{yy0} \\
\gamma_{xy0} \\
\gamma_{xz0} \\
\gamma_{yz0}
\end{Bmatrix}
=
\begin{Bmatrix}
u_{0,x} \\
v_{0,y} \\
u_{0,y} + v_{0,x} \\
\varphi_x + w_{0,x} \\
\varphi_y + w_{0,y}
\end{Bmatrix},
\tag{6}
$$

and the change of curvatures may be obtained in terms of cross-section rotations as

$$
\begin{Bmatrix}
\kappa_{xx} \\
\kappa_{yy} \\
\kappa_{xy} \\
\kappa_{xz} \\
\kappa_{yz}
\end{Bmatrix}
=
\begin{Bmatrix}
\varphi_{x,x} \\
\varphi_{y,y} \\
\varphi_{x,y} + \varphi_{y,x} \\
0 \\
0
\end{Bmatrix},
\tag{7}
$$

where in Equation 6 and Equation 7 (and hereafter), the comma in the subscript indicates the derivative with respect to the variable following the comma.

Under linear elastic behavior of the composite media, the strain components may be obtained in terms of strain components according to the following generalized Hook law as

$$
\begin{Bmatrix}
\sigma_{xx} \\
\sigma_{yy} \\
\tau_{yz} \\
\tau_{xz} \\
\tau_{xy}
\end{Bmatrix}
=
\begin{bmatrix}
Q_{11} & Q_{12} & 0 & 0 & 0 \\
Q_{12} & Q_{22} & 0 & 0 & 0 \\
0 & 0 & Q_{44} & 0 & 0 \\
0 & 0 & 0 & Q_{55} & 0 \\
0 & 0 & 0 & 0 & Q_{66}
\end{bmatrix}
\begin{Bmatrix}
\varepsilon_{xx} \\
\varepsilon_{yy} \\
\gamma_{yz} \\
\gamma_{xz} \\
\gamma_{xy}
\end{Bmatrix},
\tag{8}
$$

where the plane-stress stiffnesses of the plate are denote by Q_{ij} components (i,j = 1,2,4,5,6). These constants may be obtained in terms of the Poisson's ratio, shear modulus and Young's modulus of the composite plate as [29]

$$Q_{11} = \frac{E_{11}}{1-\nu_{12}\nu_{21}}, \quad Q_{22} = \frac{E_{22}}{1-\nu_{12}\nu_{21}}, \quad Q_{12} = \frac{\nu_{21}E_{11}}{1-\nu_{12}\nu_{21}} \quad (9)$$

$$Q_{44} = G_{23}, \quad Q_{55} = G_{13}, \quad Q_{66} = G_{12}.$$

To construct the motion equations of the plate, the Hamilton principle may be used [35]. For free vibration analysis where external forces/moments are absent, Hamilton's principle may be written as

$$\int_{t_1}^{t_2} \delta(U-T)dt = 0$$
$$t = t_1, t_2 : \delta u_0 = \delta v_0 = \delta w_0 = \delta\varphi_x = \delta\varphi_y = 0, \quad (10)$$

where δU is the virtual strain energy of the perforated plate which may be calculated as

$$\delta U = \delta U_1 - \delta U_2. \quad (11)$$

In the above equation and in the rest of this work, the subscripts 1 and 2 denote a solid rectangle (i.e., a solid rectangle without a cutout) and the cutout segment, respectively. The strain energies may be obtained upon integration of the density of the strain energy over the suitable volume.

$$\delta U_i = \int_{A_i}\int_z \left(\sigma_{xx}\delta\varepsilon_{xx} + \sigma_{yy}\delta\varepsilon_{yy} + \tau_{xy}\delta\gamma_{xy} \right.$$
$$\left. + \kappa\tau_{xz}\delta\gamma_{xz} + \kappa\tau_{yz}\delta\gamma_{yz}\right)dz\,dA_i, \quad i = 1,2 \quad (12)$$

where the shear correction factor is denoted by κ. This parameter is used to compensate for the errors due to the assumption of constant shear strains across the thickness. The exact value of this factor is not straightforward and may be obtained under evaluation of complicated integrals. Since the exact value of this factor depends on the boundary conditions, geometry of the media, material and loading, the approximate value of κ = 5/6 is used in the present research.

Similarly, δT is the variation of the kinetic energy of the plate which also may be written as

$$\delta T = \delta T_1 - \delta T_2, \quad (13)$$

where the kinetic energy may be obtained as

$$\delta T_i = \int_{A_i}\int_z \rho(z)\left(\dot{u}\,\delta\dot{u} + \dot{v}\,\delta\dot{v}\right.$$
$$\left. + \dot{w}\,\delta\dot{w}\right)dz\,dA_i, \quad i = 1,2. \quad (14)$$

Solution procedure

It is known that the equations of motion for a plate with three translational motion and two rotational motion components may be achieved using the process of virtual displacements with the aid of the Green–Gauss theorem. On the other hand, the matrix representation of the equations of motion may be established using the application of energy methods to Equation 10. As one of the most widely known energy-based methods, the Ritz method is used in the present research. The effectiveness and efficiency of various types of Ritz methods has been the subject of many studies [36-39]. In this study, the approximation of the displacement field is carried out using the Ritz method whose shape functions are written in terms of the Chebyshev polynomials. As a result, the essential variables may be written as

$$u_0(x,y,t) = R^u(x,y)\sum_{i=1}^{N_x}\sum_{j=1}^{N_y} U_{ij}(t)P_i(x)P_j(y)$$

$$v_0(x,y,t) = R^v(x,y)\sum_{i=1}^{N_x}\sum_{j=1}^{N_y} V_{ij}(t)P_i(x)P_j(y)$$

$$w_0(x,y,t) = R^w(x,y)\sum_{i=1}^{N_x}\sum_{j=1}^{N_y} W_{ij}(t)P_i(x)P_j(y) \quad (15)$$

$$\varphi_x(x,y,t) = R^x(x,y)\sum_{i=1}^{N_x}\sum_{j=1}^{N_y} X_{ij}(t)P_i(x)P_j(y)$$

$$\varphi_y(x,y) = R^y(x,y)\sum_{i=1}^{N_x}\sum_{j=1}^{N_y} Y_{ij}(t)P_i(x)P_j(y).$$

In Equation 15, the *i*-th Chebyshev polynomial of the first kind is denoted by P_i. These functions in a closed-form expression may be written as

$$P_i(x) = \cos((i-1)\arccos(2x/a))$$
$$P_j(y) = \cos((j-1)\arccos(2y/b)). \quad (16)$$

Additionally, in Equation 15, the auxiliary functions ($R^\alpha(x,y)$, where α = *u,v,w,x,y*) are called the boundary functions, which are associated with the essential boundary conditions. It is known that in the Ritz method, the shape functions should at least satisfy the essential boundary conditions.

Three types of mechanical boundary conditions are widely used for each of the edges of the plate: clamped (C), simply supported (S) and free (F) edges are the assumed types of boundary conditions in the present study. For a clamped edge, three components of the displacement field and two components of the rotation should be zero at the edge. For a simply supported one, the tangential displacement, tangential rotation and lateral displacement should be zero. Finally, for a free edge, none of the boundary conditions are applied, and therefore, none of the displacements and rotations are restrained at the edge. On each exterior edge of the plate, various boundary conditions may be defined; however, the interior edges are all assumed to be free and none of the boundary conditions around the hole are applied.

Since the Chebyshev polynomials of the fist kind are nonzero on both ends of the interval (i.e., $P_i(\pm 1) \neq 0$), the auxiliary functions R^α, $\alpha = u,v,w,x,y$ should be chosen to satisfy the essential boundary conditions on the edge when necessary. Each of the auxiliary functions R^α, $\alpha = u,v,w,x,y$ may be written generally as

$$R^\alpha(x,y) = \left(1 + \frac{2x}{a}\right)^p \left(1 - \frac{2x}{a}\right)^q \left(1 + \frac{2y}{b}\right)^r \left(1 - \frac{2y}{b}\right)^s. \quad (17)$$

The newly introduced parameters, p, q, r and s, are equal to zero or one and their magnitude depends on the essential boundary conditions at the edge. As an example, consider a perforated plate with clamped boundary conditions at $x = -0.5a$ and $x = +0.5a$, free at $y = -0.5b$, and simply supported at $y = +0.5b$. For such a case, the auxiliary functions (R^α, where $\alpha = u,v,w,x,y$) are given as

$$R^u(x,y) = \left(1 + \frac{2x}{a}\right)\left(1 - \frac{2x}{a}\right)\left(1 - \frac{2y}{b}\right)$$

$$R^v(x,y) = \left(1 + \frac{2x}{a}\right)\left(1 - \frac{2x}{a}\right)$$

$$R^w(x,y) = \left(1 + \frac{2x}{a}\right)\left(1 - \frac{2x}{a}\right)\left(1 - \frac{2y}{b}\right) \quad (18)$$

$$R^x(x,y) = \left(1 + \frac{2x}{a}\right)\left(1 - \frac{2x}{a}\right)\left(1 - \frac{2y}{b}\right)$$

$$R^y(x,y) = \left(1 + \frac{2x}{a}\right)\left(1 - \frac{2x}{a}\right).$$

Finally, the substitution of the series expansion of Equation 15 into Equation 12 and Equation 14, and inserting the results into the Hamilton principle of Equation 10 results in the motion equations given as

$$\mathbf{M\ddot{X}} + \mathbf{KX} = 0. \quad (19)$$

In the above equation, $\mathbf{M}$ is the mass matrix and, $\mathbf{K}$ is the stiffness matrix. Additionally, the mechanical displacement vector is denoted by $\mathbf{X}$, which consists of the unknown displacements U_{ij}, V_{ij}, W_{ij}, X_{ij} and Y_{ij}.

Since the free vibration response is under investigation, $\mathbf{X} = \hat{\mathbf{X}}$ $\sin(\omega t + \varphi)$ may be considered, where ω is the natural frequency. The substitution of this equation into Equation 19 results in an eigenvalue problem as

$$\left(\mathbf{K} - \omega^2 \mathbf{M}\right)\hat{\mathbf{X}} = 0. \quad (20)$$

This eigenvalue problem can be solved using the standard eigenvalue algorithms provided in a Matlab code. It is worth noting that trapezoidal numerical integration is used to evaluate the elements of the mass and stiffness matrices. In numerical integration, the interval is divided into 100 segments.

Results and Discussion

The free vibration characteristics of FG-CNTRC rectangular plates with a centric rectangular hole were formulated in the previous sections. In the following, to assure the effectiveness and accuracy of the presented solution method, convergence and comparison studies are carried out. Next, parametric studies are provided to explore the effects of carbon nanotube characteristics on the frequencies of the perforated plate. The following convention is established for boundary conditions herein and is used in the rest of this work. For instance, an SCFS plate indicates a plate which is simply supported at $x = -0.5a$ and $y = +0.5b$, clamped at $y = -0.5b$, and free at $x = +0.5b$.

In the numerical results of the present research, isotropic poly(methyl methacrylate), referred to as PMMA, is selected as the polymeric matrix. The mechanical properties of the PMMA are $E^m = 2.5$ GPa, $\nu^m = 0.34$ and $\rho^m = 1150$ kg/m^3. Reinforcement of the matrix is chosen as (10,10)-armchair SWCNT. For this kind of reinforcement, which is orthotropic, the material properties are given as $E_{11}^{CN} = 5.6466$ TPa, $E_{22}^{CN} = 7.0800$ TPa, $G_{12} = 1.9445$ TPa, $\nu = 0.175$ and $\rho = 1400$ kg/m^3 [40].

Finally, the efficiency parameters should be known to obtain the overall properties of the composite media, which are the stretching, coupling and bending stiffnesses. As mentioned before, these parameters are obtained by matching the data obtained by the present modified rule of mixtures approach and the molecular dynamics simulations of other researchers. A mo-

lecular dynamics simulation was performed by Han and Elliott [41]; however, since the condition of maximum thickness for CNTs was not satisfied in this research, their simulations were re-examined by Shen [28]. In the simulations of Han and Elliott [41], the effective thickness of the CNTs is set equal to at least 0.34 nm, which is open to criticism since it violates the criteria proposed by Wang and Zhang [42]. The molecular dynamics simulations of Shen [28] result in the following efficiency parameters for the CNTRC media that depend on the volume fraction of CNTs: $\eta_1 = 0.137$ and $\eta_2 = 1.022$ for $V_{CN}^* = 0.12$; $\eta_1 = 0.142$ and $\eta_2 = 1.626$ for $V_{CN}^* = 0.17$; and $\eta_1 = 0.141$ and $\eta_2 = 1.585$ for $V_{CN}^* = 0.28$. For each case, the efficiency parameter η_3 is equal to $0.7\eta_2$. The shear modulus G_{13} is taken equal to G_{12}, whereas G_{23} is taken equal to $1.2G_{12}$ [28].

Convergence and comparison studies

Convergence and comparison studies are presented in this section. First, the convergence study allows for the necessary shape functions to be obtained with the series expansion of the Ritz method, with results shown in Table 2. In this study, the first three frequency parameters of a square plate with a square cutout at the center are evaluated in terms of the number of shape functions. Two different cutout sizes are considered. The results are also compared with those of Liew et al. [43] and Lam et al. [44]. In the solution method of Liew et al. [43], the basic L-shaped element, which is divided into appropriate subdomains that are dependent upon the location of the cutout, is used as the basic building element. Lam et al. [44], on the other hand, obtained the frequencies according to a Ritz method whose shape functions are generated using the Gram–Schmidt process. In both of the above-mentioned references, the plate is formulated using the classical plate theory and for the sake of comparison, in the present analysis, the side-to-thickness ratio is

chosen as $a/h = 100$. It is seen that the results of our study match well with those of Liew et al. [43] and Lam et al. [44] after the adoption of $N_x = N_y = 20$ shape functions. Therefore, in the subsequent results, the number of shape functions in both directions is chosen as 20.

In Table 3, the first four frequencies of a plate with a centric cutout clamped all around is evaluated. In this study, the plate is also a square, and for the sake of comparison, the side-to-thickness ratio is chosen as $a/h = 100$. Four different square cutout sizes, $c/a = 0.1, 0.2, 0.3$ and 0.5, are considered and in each case our results are compared with those of Malekzadeh et al. [45] and Mundkur et al. [46]. Malekzadeh et al. [45] obtained the frequencies according to a three dimensional elasticity formulation and using the Chebyshev–Ritz formulation, whereas boundary characteristics of orthogonal polynomial functions are invoked into the Ritz formulation by Mundkur et al. [46] to obtain the plate frequencies. It is seen that our results are in good agreement with those of both Malekzadeh et al. [45] and Mundkur et al. [46].

Table 4 presents the frequencies of a thin square plate that is simply supported all around and contains a square cutout at the center. The cutout size is $c/a = 0.4$ and for the sake of comparison, the side-to-thickness ratio of the square plate is chosen as $a/h = 100$. The results of this study are compared with those of Liew et al. [43]. In the tabulated results, SS indicates the double-symmetric modes and AA indicates the double-antisymmetric modes. On the other hand, modes that are symmetric in one direction and antisymmetric on the other direction are denoted by AS. Again, it is seen that the results of our study are in good agreement with the available data, which verifies the accuracy of the present method.

Table 2: Convergence study on the first three frequency parameters $\hat{\omega} = \omega a^2/h\sqrt{\rho h/D}$ of SSSS isotropic homogeneous square plates with $a/h = 100$, $v = 0.3$ and two cutout ratios.

$N_x = N_y$	$c/a=0.5$			$c/a=0.3$		
	$\hat{\omega}_1$	$\hat{\omega}_2$	$\hat{\omega}_3$	$\hat{\omega}_1$	$\hat{\omega}_2$	$\hat{\omega}_3$
4	25.3219	67.0738	96.5711	21.2056	59.9002	91.5117
6	24.3337	52.4935	79.6489	20.7782	49.9952	76.7551
8	23.9120	48.0090	76.8117	20.3092	49.4326	76.0125
10	23.7717	44.2278	74.2547	19.9607	48.9185	75.6918
12	23.7394	42.6920	72.9483	19.8747	48.1375	75.3304
14	23.7177	42.1001	72.4587	19.8625	47.2216	74.9326
16	23.6514	41.6152	72.1370	19.7767	46.4394	74.6078
18	23.5996	41.2933	71.8660	19.7260	45.9450	74.3541
20	23.5641	41.0550	71.7298	19.6490	45.5670	74.2122
Liew et al. [43]	23.441	41.779	71.737	19.391	44.799	73.656
Lam et al. [44]	23.235	39.712	69.868	19.357	44.207	73.906

Table 3: First four frequency parameters $\hat{\omega} = \omega a^2 / \sqrt{\rho h / D}$ for square CCCC isotropic homogeneous plates with v = 0.3, *a/h* = 100 and various square cutout sizes.

c/a	Source	$\hat{\omega}_1$	$\hat{\omega}_2$	$\hat{\omega}_3$	$\hat{\omega}_4$
0.1	Malekzadeh et al. [45]	36.7943	73.9968	74.0389	108.1382
	Mundkur et al. [46]	36.5045	73.4142	73.4142	107.3528
	Present	36.3141	73.2476	73.2476	106.9850
0.2	Malekzadeh et al. [45]	37.9162	73.8299	73.8882	105.9458
	Mundkur et al. [46]	38.1073	73.6267	73.6267	105.4715
	Present	37.2017	72.7578	72.7578	104.7691
0.3	Malekzadeh et al. [45]	41.6279	71.2093	71.3769	103.6814
	Mundkur et al. [46]	41.7912	73.9799	73.9799	104.3388
	Present	40.9624	69.0943	69.0943	101.9502
0.5	Malekzadeh et al. [45]	66.5457	79.1407	79.2248	109.2086
	Mundkur et al. [46]	65.7150	81.6796	81.6796	110.8569
	Present	65.3050	77.7074	77.7074	107.5626

Table 4: Frequency parameters, $\hat{\omega} = \omega a^2 / \sqrt{\rho h / D}$ for square SSSS isotropic homogeneous plates with a square cutout with v = 0.3, *c/a* = 0.4 and *a/h* = 100.

Mode Type	Source	$\hat{\omega}_1$	$\hat{\omega}_2$	$\hat{\omega}_3$
SS	Liew et al. [43]	20.7240	85.4180	136.2900
	Present	20.9151	85.8040	136.1697
AS	Liew et al. [43]	41.9070	118.7200	181.7200
	Present	42.1561	119.6766	177.3160
AA	Liew et al. [43]	71.4990	189.3300	200.9000
	Present	71.9878	188.1986	198.4664

The next comparison study gives the frequency parameters of the FG-CNTRC plate with clamped boundary conditions. The frequencies are evaluated from the proposed approach of our study and compared with those given by Zhu et al. [4] based on

the finite elements method. It is worth noting that in the analysis of Zhu et al. [4], the matrix is made from PmPV with elasticity modulus E^m = 2.1 GPa, Poisson's ratio v^m = 0.34 and mass density ρ^m = 1150 kg/m³. The volume fraction of CNTs is set equal to 0.17 and the dispersion pattern of the CNTs is of the FG-V type. In such case, the efficiency parameters are obtained as η_1 = 0.149 and $\eta_2 = \eta_3$ = 1.381 [4]. Furthermore, $G_{23} = G_{13} = G_{12}$ is assumed [4]. The frequency parameter is defined as $\hat{\omega} = \omega a^2 / h \sqrt{\rho^m / E^m}$ as shown in Table 5. As can be seen, the first six frequencies are in good agreement with those obtained by Zhu et al. [4].

The next comparison study is devoted to the case of a nonsquare plate with a nonsquare cutout. A thin plate with *a/h* = 100 and CSCS boundary conditions is considered. The length-to-width ratio is equal to *a/b* = 1.125. The cutout dimensions are the same as those of Liew et al. [43], that is, *c/a* = 1/3

Table 5: First six natural frequencies $\hat{\omega} = \omega a^2 / h \sqrt{\rho^m / E^m}$ of square CCCC FG-CNTRC plates without cutout and various side-to-thickness ratios.

$\hat{\omega}$	*a/h* = 10		*a/h* = 20		*a/h* = 50	
	Present	Zhu et al. [4]	Present	Zhu et al. [4]	Present	Zhu et al. [4]
$\hat{\omega}_1$	21.4953	21.544	32.5463	32.686	41.7819	42.078
$\hat{\omega}_2$	28.4093	28.613	38.9996	39.279	47.7825	48.309
$\hat{\omega}_3$	41.2024	41.431	53.4057	54.560	62.3669	63.755
$\hat{\omega}_4$	41.2818	42.119	69.5133	70.149	86.1407	90.293
$\hat{\omega}_5$	45.5711	45.796	73.3744	73.926	104.7524	106.513
$\hat{\omega}_6$	46.9814	47.055	75.1651	78.522	108.3582	110.055

and $d/b = 1/3$. The first four frequencies of the plate are obtained and compared with the available data in the literature. It is worth noting that, in this case, the experimental results of Aksu and Ali [47] are also available. A comparison is provided in Table 6. It is seen that the results of our study match well with the available data in the literature.

Table 6: First four frequency parameters, $\hat{\omega} = \omega a^2 \sqrt{\rho h / D}$, for a CSCS, rectangular, isotropic, homogeneous plate with a rectangular cutout with v = 0.3, *c/a = d/b = 1/3, a/b = 9/8* and *a/h* = 100.

$\hat{\omega}$	Liew et al. [43]	Aksu et al. [47] (Exp.)	Aksu et al. [47]	Lam et al. [44]	Present
$\hat{\omega}_1$	32.425	33.22	33.83	34.04	31.2802
$\hat{\omega}_2$	53.426	53.01	53.99	54.57	54.2069
$\hat{\omega}_3$	62.353	61.91	62.49	65.05	60.0453
$\hat{\omega}_4$	94.839	91.87	95.03	95.38	92.0645

Table 7 presents the fundamental and second symmetric modes of the frequency parameters of a unidirectional, orthotropic plate in a square platform with a centric square cutout. The material properties of the layer are $E_{11} = 140$ GPa, $E_{22} = 3.5$ GPa, $G_{12} = 0.5$ GPa, $v_{12} = 0.25$ and $\rho = 4000$ kg/m^3. The plate is simply supported all around and a cutout size is chosen as $c/a = 0.5$. The results are provided for various side-to-thickness ratios. A comparison is made between the results of our study with those obtained by Reddy [48] based on the finite elements method and by Ovesy and Fazilati [49] based on the finite strip method. The results are provided in Table 7. It can be seen that the results of our study match well with the available data in the literature, which proves the correctness of the formulation and solution method of the present research.

Parametric studies

After validating the formulation and proposed method of the present research, the parametric studies are provided in this section. In this section, the frequency parameter is defined as

$\hat{\omega} = \omega a^2 / h \sqrt{\rho_m / D_m}$, where D_m is the flexural rigidity of a plate made from the polymeric matrix.

Tables 8–11 present the first five frequencies of CNTRC plates in a square shape and side-to-thickness ratio of $a/h = 20$. Table 8, Table 9, Table 10 and Table 11 are associated with CCCC, CFFF, SSSS and CFCF plates, respectively. The volume fraction of CNTs is chosen as $V_{CN}^* = 0.17$. In each case, the frequencies are provided for three different perforation sizes and four different graded patterns of CNTs. It is seen that, similar to the case of plates without a cutout, in plates with a hole, FG-X also has the highest fundamental frequency and FG-O has the lowest. The influence of hole size on fundamental frequency is not monotonic. For instance, in CCCC plates, the fundamental frequency of a plate increases when the hole size increases from $c/a = 0.1$ to 0.3 and 0.5. This conclusion is qualitatively compatible with the results of Malekzadeh et al. [45] for CCCC FGM plates. For SSSS and CFFF plates, on the other hand, the trend is the inverse and the fundamental frequency of a plate decreases when the hole size increases from $c/a = 0.1$ to 0.3 and 0.5. The results presented in Tables 8–11 contain both the flexural and extensional as well as coupled (in FG-V type) vibrational modes. As seen from Table 10, the fourth and fifth frequencies of SSSS plates without a cutout or with a cutout size of $c/a = 0.1$ and 0.3 are the same. These frequencies are in-plane modes and, due to the symmetry of geometry and boundary conditions, they are equal. It is seen that the in-plane frequencies of FG-X and FG-O plates are equal.

Table 12 presents the first five frequencies (including both in-plane and out-of-plane) of square plates made of FG-CNTRC with centric cutouts of various sizes. The side-to-thickness ratio is set equal to $a/h = 20$ and the plate is clamped all around. Numerical results are given for three different volume fractions of CNTs and four different graded patterns of CNTs. Similar to the case of plates without a cutout, an increase in the CNT volume fraction yields a higher natural frequency of the plate. The plates with an FG-X pattern of CNTs have higher frequencies in comparison to UD, FG-V and FG-O plates.

Table 7: Fundamental and second symmetric mode frequency parameters, $\hat{\omega} = \omega a^2 \sqrt{\rho h / D_{22}}$, for a SSSS, square, unidirectional, orthotropic plate with a square cutout with *c/a = d/b* = 1/2 and various *a/h* ratios.

	$\hat{\omega}_1$			$\hat{\omega}_2$		
h/a	Reddy [48]	Ovesy and Fazilati [49]	Present	Reddy [48]	Ovesy and Fazilati [49]	Present
0.010	51.232	51.608	51.4407	112.220	111.399	112.8712
0.040	48.907	49.049	49.0386	103.430	102.478	103.4018
0.050	47.934	47.975	47.9682	100.100	99.129	99.8877
0.100	42.693	42.108	42.0505	83.451	82.654	82.4266
0.200	34.069	32.416	32.1979	59.074	59.071	60.7709

Table 8: First five natural frequency parameters for square FG-CNTRC CCCC plates with a centric cutout. Geometrical characteristics of the plate are *a/b* = 1, *h/a* = 0.05 and various *c/a* ratios. The volume fraction of CNTs is set equal to V_{CN}^* = 0.17.

c/a	Type	$\hat{\omega}_1$	$\hat{\omega}_2$	$\hat{\omega}_3$	$\hat{\omega}_4$	$\hat{\omega}_5$
0.0	UD	104.7581	127.4624	177.3348	216.4439	229.8165
	FG-X	112.9857	136.1313	187.5684	228.1375	241.8078
	FG-O	90.1519	114.9774	166.5357	195.1187	209.9151
	FG-V	97.1637	122.2427	175.0384	205.6517	220.5951
0.1	UD	105.4667	127.4527	178.2958	210.3946	229.2000
	FG-X	114.0739	136.1672	188.9056	221.1219	241.2009
	FG-O	90.3317	114.9383	167.1189	190.7122	209.3028
	FG-V	97.5556	122.2235	175.8912	200.6315	219.9939
0.3	UD	120.4439	126.9656	169.8070	188.2571	218.9324
	FG-X	130.6054	136.3973	181.1849	199.9691	230.5113
	FG-O	102.7080	112.4737	150.9616	174.3439	199.9412
	FG-V	111.1976	120.2882	160.6058	183.8592	210.3512
0.5	UD	144.3419	145.0951	220.7844	229.0503	231.6397
	FG-X	155.3892	156.2246	233.7825	242.7781	244.6759
	FG-O	129.1618	129.9906	196.1895	205.0887	209.8574
	FG-V	137.8894	138.7569	208.3156	208.3156	217.4388

Table 9: First five natural frequency parameters for square, FG-CNTRC, CFFF plates with a centric cutout. Geometrical characteristics of the plate are *a/b* = 1, *h/a* = 0.05 with various *c/a* ratios. The volume fraction of CNTs is set equal to V_{CN}^* = 0.17.

c/a	Type	$\hat{\omega}_1$	$\hat{\omega}_2$	$\hat{\omega}_3$	$\hat{\omega}_4$	$\hat{\omega}_5$
0.0	UD	22.7727	24.3214	40.0851	69.2495	83.6431
	FG-X	27.0842	28.4568	44.0066	69.7239	89.4504
	FG-O	16.7435	18.7782	36.1389	69.7239	79.6264
	FG-V	19.1381	21.0721	38.7339	69.6796	84.0389
0.1	UD	22.6504	24.2757	40.0027	68.9550	83.8138
	FG-X	26.9308	28.4058	43.8532	69.4269	89.3451
	FG-O	16.6641	18.7287	36.0570	69.4269	79.5320
	FG-V	19.0430	21.0212	38.6399	69.3808	83.9355
0.3	UD	20.4172	24.0224	37.9453	65.3384	81.1811
	FG-X	24.0635	28.1470	41.3325	65.7754	86.5017
	FG-O	15.2671	18.4600	34.5625	65.7754	76.7925
	FG-V	17.3638	20.7497	36.9148	65.6852	81.0431
0.5	UD	16.9516	23.0500	34.9990	55.9159	75.0937
	FG-X	19.6883	27.0578	38.2949	56.2537	79.9457
	FG-O	12.9576	17.6252	31.7571	56.2537	70.7251
	FG-V	14.6594	19.8497	33.9178	56.0921	74.7579

Conclusion

The natural frequencies of carbon-nanotube-reinforced, composite laminated plates with a rectangular hole in the center was analyzed in this research. The properties of the plate were obtained according to a modified rule of mixtures, which includes the efficiency parameters to account for the size-dependent characteristics of the nanocomposite. The distribution of CNTs across the plate thickness was both uniform or functionally graded. An energy-based Ritz formulation was constructed to obtain the frequencies of the plate. The basis shape functions were obtained using the Chebyshev polynomials, suitable for arbitrary in-plane and out-of-plane boundary conditions on the

Table 10: First five natural frequency parameters for square, FG-CNTRC, SSSS plates with a centric cutout. Geometrical characteristics of the plate are *a/b* = 1, *h/a* = 0.05 with various *c/a* ratios. The volume fraction of CNTs is set equal to V_{CN}^* 0.17.

c/a	Type	$\hat{\omega}_1$	$\hat{\omega}_2$	$\hat{\omega}_3$	$\hat{\omega}_4$	$\hat{\omega}_5$
0.0	UD	63.2598	83.2741	132.0746	143.7036	143.7036
	FG-X	72.8708	92.2430	141.7590	144.7344	144.7344
	FG-O	49.4292	72.4990	123.2571	144.7344	144.7344
	FG-V	55.2524	78.2905	130.3768	144.7268	144.7268
0.1	UD	62.8020	83.1849	131.8828	144.8261	144.8261
	FG-X	72.4414	92.1454	141.5884	145.8609	145.8609
	FG-O	49.0286	72.4102	123.0916	145.8609	145.8609
	FG-V	54.8235	78.1925	130.2147	145.8510	145.8510
0.3	UD	52.8233	78.3506	111.6736	130.6302	154.9683
	FG-X	60.5716	87.1986	119.1929	139.3437	156.0783
	FG-O	41.9863	67.4468	100.7698	123.2779	156.0783
	FG-V	46.7420	73.0816	107.2829	129.9159	156.0612
0.5	UD	49.7695	72.2115	75.6430	110.4459	153.9671
	FG-X	56.2066	80.5715	80.8909	118.0424	165.6159
	FG-O	40.9160	31.2728	69.6564	103.1278	136.3056
	FG-V	45.0900	66.7584	73.9966	108.6995	146.1801

Table 11: First five natural frequency parameters for square, FG-CNTRC, CFCF plates with a centric cutout. Geometrical characteristics of the plate are *a/b* = 1, *h/a* = 0.05 with various *c/a* ratios. The volume fraction of CNTs is set equal to V_{CN}^* 0.17.

c/a	Type	$\hat{\omega}_1$	$\hat{\omega}_2$	$\hat{\omega}_3$	$\hat{\omega}_4$	$\hat{\omega}_5$
0.0	UD	100.1209	100.5478	106.0262	130.1245	142.0229
	FG-X	108.3648	108.7314	114.1163	138.8282	143.0241
	FG-O	84.7084	85.3698	92.0274	118.2125	143.0241
	FG-V	91.7731	92.3623	98.8950	125.5211	142.9107
0.1	UD	100.2534	100.3429	106.3842	129.9112	143.1875
	FG-X	108.5295	108.6060	114.7279	138.6133	144.1970
	FG-O	84.6851	85.1671	92.0179	117.9871	144.1970
	FG-V	91.8120	92.1557	99.0190	125.2861	144.0832
0.3	UD	100.7600	101.2200	118.8467	128.0103	153.1897
	FG-X	108.9985	109.4736	128.8350	137.2623	154.2720
	FG-O	85.4922	85.9562	101.4103	114.2352	151.0984
	FG-V	92.5250	93.0347	109.7041	121.8601	154.1448
0.5	UD	101.6312	101.6706	134.2600	134.9668	164.4286
	FG-X	109.8563	109.9006	144.0598	144.7920	165.5952
	FG-O	86.8830	86.5131	118.6095	119.3833	165.5945
	FG-V	93.5251	93.5551	126.8153	127.6207	165.3665

exterior and the cutout is assumed to be free. After performing comparison studies for isotropic and unidirectional plates with a centric cutout, the parametric studies were given for plates both with and without a cutout. It is shown that, similar to FG-CNTRC plates without a cutout, increasing the CNT volume fraction results in higher frequencies of the plate with a cutout. Furthermore, FG-X plates have a higher natural frequency in comparison to the other three patterns of CNTs. It was also demonstrated that the variation of fundamental frequency of a perforated plate with respect to the hole size is not monotonic and is dependent on the boundary conditions.

Table 12: First five natural frequency parameters for square, FG-CNTRC, CCCC plates with a centric cutout. The geometrical characteristics of the plate are *a/b* = 1, *h/a* = 0.05 and *c/a* = 0.5.

c/a	V^*_{CN}	Type	$\hat{\omega}_1$	$\hat{\omega}_2$	$\hat{\omega}_3$	$\hat{\omega}_4$	$\hat{\omega}_5$
0.1	0.12	UD	83.9188	100.3679	139.1968	165.6225	180.1856
		FG-X	89.8427	105.9079	145.2992	172.7141	187.9588
		FG-O	72.7097	91.3377	131.5790	151.3920	165.3920
		FG-V	78.0171	96.2557	136.8848	158.4278	173.2206
	0.17	UD	105.4667	127.4527	178.2958	210.3946	229.2000
		FG-X	114.0739	136.1672	188.9056	221.1219	241.2009
		FG-O	90.3317	114.9383	167.1189	190.7122	209.3028
		FG-V	97.5556	122.2235	175.8912	200.6315	219.9939
	0.28	UD	117.9367	139.0787	190.6561	229.2992	249.0083
		FG-X	128.1334	152.0944	210.3997	243.4859	266.0974
		FG-O	103.9972	126.0241	176.2058	214.6312	232.7102
		FG-V	111.7471	135.8179	190.8244	224.2330	244.4012
0.3	0.12	UD	95.8721	100.3370	134.1470	147.7287	172.0447
		FG-X	102.8278	106.5212	141.7684	154.5267	179.4637
		FG-O	82.7712	89.7543	120.3341	137.5941	158.4212
		FG-V	89.0013	95.2007	127.2195	143.6480	165.5769
	0.17	UD	120.4439	126.9656	169.8070	188.2571	218.9324
		FG-X	130.6054	136.3973	181.1849	199.9691	230.5113
		FG-O	102.7080	112.4737	150.9616	174.3439	199.9412
		FG-V	111.1976	120.2882	160.6058	183.8592	210.3512
	0.28	UD	134.7884	139.7667	186.8796	202.9367	237.6707
		FG-X	147.0185	152.8559	201.8094	222.8837	254.4027
		FG-O	118.3189	125.0040	169.6503	186.3970	221.8681
		FG-V	127.5548	135.0123	180.5800	201.1201	233.5064
0.5	0.12	UD	114.3763	114.9769	174.3637	180.8571	182.4758
		FG-X	121.0992	121.7038	182.9347	189.6084	190.7261
		FG-O	102.9381	103.5831	156.5728	163.3712	166.6608
		FG-V	108.9502	109.6062	165.2573	172.0949	174.7810
	0.17	UD	144.3419	145.0951	220.7844	229.0503	231.6397
		FG-X	155.3892	156.2246	233.7825	242.7781	244.6759
		FG-O	129.1618	129.9906	196.1895	205.0887	209.8574
		FG-V	137.8894	138.7569	208.3156	208.3156	217.4388
	0.28	UD	158.9989	159.7737	242.3844	251.0307	252.5998
		FG-X	173.8958	174.8389	258.3101	268.3936	270.2030
		FG-O	143.1568	143.9204	223.0877	231.1761	234.5069
		FG-V	154.2322	155.1098	234.8549	244.0462	247.0420

References

1. Kwon, H.; Bradbury, C. R.; Leparoux, M. *Adv. Eng. Mater.* **2011,** *13,* 325–329. doi:10.1002/adem.201000251
2. Liew, K. M.; Lei, Z. X.; Zhang, L. W. *Compos. Struct.* **2015,** *120,* 90–97. doi:10.1016/j.compstruct.2014.09.041
3. Shen, H.-S. *Compos. Struct.* **2009,** *91,* 9–19. doi:10.1016/j.compstruct.2009.04.026
4. Zhu, P.; Lei, Z. X.; Liew, K. M. *Compos. Struct.* **2012,** *94,* 1450–1460. doi:10.1016/j.compstruct.2011.11.010
5. Zhang, L. W.; Lei, Z. X.; Liew, K. M. *Compos. Struct.* **2015,** *122,* 172–183. doi:10.1016/j.compstruct.2014.11.070
6. Zhang, L. W.; Lei, Z. X.; Liew, K. M. *Compos. Struct.* **2015,** *120,* 189–199. doi:10.1016/j.compstruct.2014.10.009
7. Zhang, L. W.; Lei, Z. X.; Liew, K. M.; Yu, J. L. *Compos. Struct.* **2014,** *111,* 205–212. doi:10.1016/j.compstruct.2013.12.035
8. Zhang, L. W.; Lei, Z. X.; Liew, K. M. *Appl. Math. Comput.* **2015,** *256,* 488–504. doi:10.1016/j.amc.2015.01.066
9. Lei, Z. X.; Zhang, L. W.; Liew, K. M. *Compos. Struct.* **2015,** *127,* 245–259. doi:10.1016/j.compstruct.2015.03.019
10. Malekzadeh, P.; Zarei, A. R. *Thin-Walled Struct.* **2014,** *82,* 221–232. doi:10.1016/j.tws.2014.04.016

11. Malekzadeh, P.; Heydarpour, Y. *Meccanica* **2015,** *50,* 143–167.
    doi:10.1007/s11012-014-0061-4
12. Natarajan, S.; Haboussi, M.; Manickam, G. *Compos. Struct.* **2014,** *113,*
    197–207. doi:10.1016/j.compstruct.2014.03.007
13. Wang, Z.-X.; Shen, H.-S. *Comput. Mater. Sci.* **2011,** *50,* 2319–2330.
    doi:10.1016/j.commatsci.2011.03.005
14. Wang, Z.-X.; Shen, H.-S. *Composites, Part B* **2012,** *43,* 411–421.
    doi:10.1016/j.compositesb.2011.04.040
15. Wang, Z.-X.; Shen, H.-S. *Nonlinear Dyn.* **2012,** *70,* 735–754.
    doi:10.1007/s11071-012-0491-2
16. Lei, Z. X.; Zhang, L. W.; Liew, K. M. *Int. J. Mech. Sci.* **2015,** *99,*
    208–217. doi:10.1016/j.ijmecsci.2015.05.014
17. Lei, Z. X.; Zhang, L. W.; Liew, K. M.; Yu, J. M. *Compos. Struct.* **2014,**
    113, 328–338. doi:10.1016/j.compstruct.2014.03.035
18. Zhang, L. W.; Song, Z. G.; Liew, K. M. *Compos. Struct.* **2015,** *134,*
    989–1003. doi:10.1016/j.compstruct.2015.08.138
19. Zhang, L. W.; Liew, K. M. *Compos. Struct.* **2015,** *132,* 974–983.
    doi:10.1016/j.compstruct.2015.07.017
20. Zhang, L. W.; Song, Z. G.; Liew, K. M. *Compos. Struct.* **2015,** *128,*
    165–175. doi:10.1016/j.compstruct.2015.03.011
21. Zhang, L. W.; Cui, W. C.; Liew, K. M. *Int. J. Mech. Sci.* **2015,** *103,*
    9–21. doi:10.1016/j.ijmecsci.2015.08.021
22. Zhang, L. W.; Liew, K. M. *Comput. Methods Appl. Mech. Eng.* **2015,**
    295, 219–239. doi:10.1016/j.cma.2015.07.006
23. Zhang, L. W.; Lei, Z. X.; Liew, K. M. *Composites, Part B* **2015,** *75,*
    36–46. doi:10.1016/j.compositesb.2015.01.033
24. Lei, Z. X.; Zhang, L. W.; Liew, K. M. *Composites, Part B* **2016,** *84,*
    211–221. doi:10.1016/j.compositesb.2015.08.081
25. Zhang, L. W.; Liew, K. M.; Reddy, J. N.
    Comput. Methods Appl. Mech. Eng. **2016,** *298,* 1–28.
    doi:10.1016/j.cma.2015.09.016
26. Shi, D.-L.; Feng, X.-Q.; Huang, Y. Y.; Hwang, K.-C.; Gao, H.
    J. Eng. Mater. Technol. **2004,** *126,* 250–257. doi:10.1115/1.1751182
27. Fidelus, J. D.; Wiesel, E.; Gojny, F. H.; Schulte, K.; Wagner, H. D.
    Composites, Part A **2005,** *36,* 1555–1561.
    doi:10.1016/j.compositesa.2005.02.006
28. Shen, H.-S. *Compos. Struct.* **2011,** *93,* 2096–2108.
    doi:10.1016/j.compstruct.2011.02.011
29. Jam, J. E.; Kiani, Y. *Compos. Struct.* **2015,** *125,* 586–595.
    doi:10.1016/j.compstruct.2015.02.052
30. Jam, J. E.; Kiani, Y. *Compos. Struct.* **2015,** *132,* 35–43.
    doi:10.1016/j.compstruct.2015.04.045
31. Mirzaei, M.; Kiani, Y. *Compos. Struct.* **2015,** *134,* 1004–1013.
    doi:10.1016/j.compstruct.2015.09.003
32. Mirzaei, M.; Kiani, Y. *Aerosp. Sci. Technol.* **2015,** *47,* 42–53.
    doi:10.1016/j.ast.2015.09.011
33. Mirzaei, M.; Kiani, Y. *Compos. Struct.* **2016,** *142,* 45–56.
    doi:10.1016/j.compstruct.2015.12.071
34. Mirzaei, M.; Kiani, Y. *Meccanica* **2016,** 1–17.
    doi:10.1007/s11012-015-0348-0
35. Reddy, J. N. *Mechanics of Laminated Composite Plates and Shells,
    Theory and Application;* CRC Press: Boca Raton, FL, U.S.A., 2003.
36. Zhang, L. W.; Zhu, P.; Liew, K. M. *Compos. Struct.* **2014,** *108,*
    472–492. doi:10.1016/j.compstruct.2013.09.043
37. Zhu, P.; Zhang, L. W.; Liew, K. M. *Compos. Struct.* **2014,** *107,*
    298–314. doi:10.1016/j.compstruct.2013.08.001
38. Zhang, L. W.; Li, D. M.; Liew, K. M. *Eng. Anal. Boundary Elem.* **2015,**
    54, 39–46. doi:10.1016/j.enganabound.2015.01.007
39. Zhang, L. W.; Huang, D.; Liew, K. M.
    Comput. Methods Appl. Mech. Eng. **2015,** *297,* 116–139.
    doi:10.1016/j.cma.2015.08.018
40. Shen, H.-S.; Xiang, Y. *Eng. Struct.* **2013,** *56,* 698–708.
    doi:10.1016/j.engstruct.2013.06.002
41. Han, Y.; Elliott, J. *Comput. Mater. Sci.* **2007,** *39,* 315–323.
    doi:10.1016/j.commatsci.2006.06.011
42. Wang, C. Y.; Zhang, L. C. *Nanotechnology* **2008,** *19,* 075705.
    doi:10.1088/0957-4484/19/7/075705
43. Liew, K. M.; Kitipornchai, S.; Leung, A. Y. T.; Lim, C. W.
    Int. J. Mech. Sci. **2003,** *45,* 941–959.
    doi:10.1016/S0020-7403(03)00109-7
44. Lam, K. Y.; Hung, K. C.; Chow, S. T. *Appl. Acoustics* **1989,** *28,* 49–60.
    doi:10.1016/0003-682X(89)90030-3
45. Malekzadeh, P.; Bahranifard, F.; Ziaee, S. *Compos. Struct.* **2013,** *105,*
    1–13. doi:10.1016/j.compstruct.2013.05.005
46. Mundkur, G.; Bhat, R. B.; Neriya, S. *J. Sound Vib.* **1994,** *176,* 136–144.
    doi:10.1006/jsvi.1994.1364
47. Aksu, G.; Ali, R. *J. Sound Vib.* **1976,** *44,* 147–158.
    doi:10.1016/0022-460X(76)90713-6
48. Reddy, J. N. *J. Sound Vib.* **1982,** *83,* 1–10.
    doi:10.1016/S0022-460X(82)80071-0
49. Ovesy, H. R.; Fazilati, J. *Compos. Struct.* **2012,** *94,* 1250–1258.
    doi:10.1016/j.compstruct.2011.11.009

Customized MFM probes with high lateral resolution

Óscar Iglesias-Freire[*1,2], Miriam Jaafar[1], Eider Berganza[1] and Agustina Asenjo[1]

Full Research Paper

Address:
[1]Instituto de Ciencia de Materiales de Madrid (ICMM-CSIC), Calle Sor Juana Inés de la Cruz 3, 28049, Madrid, Spain and [2]Department of Physics, McGill University, 3600 rue University, H3A 2T8, Montreal, Canada

Email:
Óscar Iglesias-Freire[*] - oiglesias@physics.mcgill.ca

* Corresponding author

Abstract

Magnetic force microscopy (MFM) is a widely used technique for magnetic imaging. Besides its advantages such as the high spatial resolution and the easy use in the characterization of relevant applied materials, the main handicaps of the technique are the lack of control over the tip stray field and poor lateral resolution when working under standard conditions. In this work, we present a convenient route to prepare high-performance MFM probes with sub-10 nm (sub-25 nm) topographic (magnetic) lateral resolution by following an easy and quick low-cost approach. This allows one to not only customize the tip stray field, avoiding tip-induced changes in the sample magnetization, but also to optimize MFM imaging in vacuum (or liquid media) by choosing tips mounted on hard (or soft) cantilevers, a technology that is currently not available on the market.

Introduction

Conventional MFM probes consist of pyramidal Si or SiN tips with a ferromagnetic thin film coating (generally a CoCr alloy) mounted on a cantilever with resonance frequency and spring constant of around 75 kHz and 3 N/m, respectively, and with a final apex radius of typically tens of nanometres. Plenty of literature can be found that reports on probe engineering aiming to achieve enhanced spatial resolution. Several works focus on reducing the physical size of the magnetic material of the tip, either by using focused ion beam (FIB) milled tips [1,2], electron beam deposited tips [3,4] or stencil-deposited metal dots onto an AFM tip [5]. Following a different approach, probes with carbon nanotubes (CNTs) have been fabricated for MFM imaging either by mechanical attachment [6-8] or direct growth on commercial pyramid tips [9]. Although good control in terms of angle and position can be achieved when attaching CNTs to Si tips by using nanomanipulators [10], it requires sophisticated and time-consuming processes. Other approaches use magnetic nanowires [11] or coated carbon nanocones [12] to improve the detection of small domains. One can also find the use of nanomagnets with high anisotropy as MFM probes [13] and different approaches to control the final domain at the tip apex [14,15], seeking best sensitivity or resolution. However, the

easiest interpretation of the results is possible in the case of single-domain MFM tips with negligible influence over the domain structure of the sample [16].

In general, the aforementioned methods involve a considerable amount of time, effort and the use of advanced fabrication techniques for engineering the tips. In addition, the achievable resolution is not greatly enhanced compared to commercial tips so their applicability is limited to particular cases of interest. Intrinsically related to the lateral resolution is the magnetic sensitivity of the probe. In order to achieve better signal-to-noise ratios, one may want larger amounts of magnetic material to be deposited at the tip apex. Unfortunately, this results in larger tip radii and subsequent lower lateral resolution; furthermore, the influence over the sample magnetic state can increase. Depending on the specific properties of each sample, a balance between resolution and sensitivity must be found. For this reason, different kinds of commercial MFM probes are available for sale. Specific low-moment or side-coated probes (having lower amounts of ferromagnetic material) can be found in the market. However, best lateral resolution is achieved with super-sharp tips. All these specific probes are found in the market at higher prices than the standard ones.

The importance of choosing a proper tip becomes clear when measuring soft samples [17,18]. Often even the stray field emerging from low-moment commercial probes becomes too large for that kind of samples. Our goal herewith is to go a step further and be able to customize the tip used for each case, particularly regarding the irreversible influence the stray field might have in magnetically soft samples. Therefore, this work is not focused on pushing the limits of MFM resolution; instead, we aim to fabricate customized tips with high lateral resolution and a controlled influence in the sample by using a fast and rather accessible approach. Our method is based on easily preparing MFM probes from commercial AFM probes by using a specific coating. By doing so, we can tune the amount of magnetic material in the probe and also select the cantilever properties for each experiment, such as the spring constant, resonance frequency or the position of the tip on the lever. We have found neither in the literature nor in the market any MFM probe with cantilever characteristics far from the range of the aforementioned. Making MFM accessible to these properties in any lab is particularly useful if one wants to carry out experiments in environments such as vacuum or liquid [19].
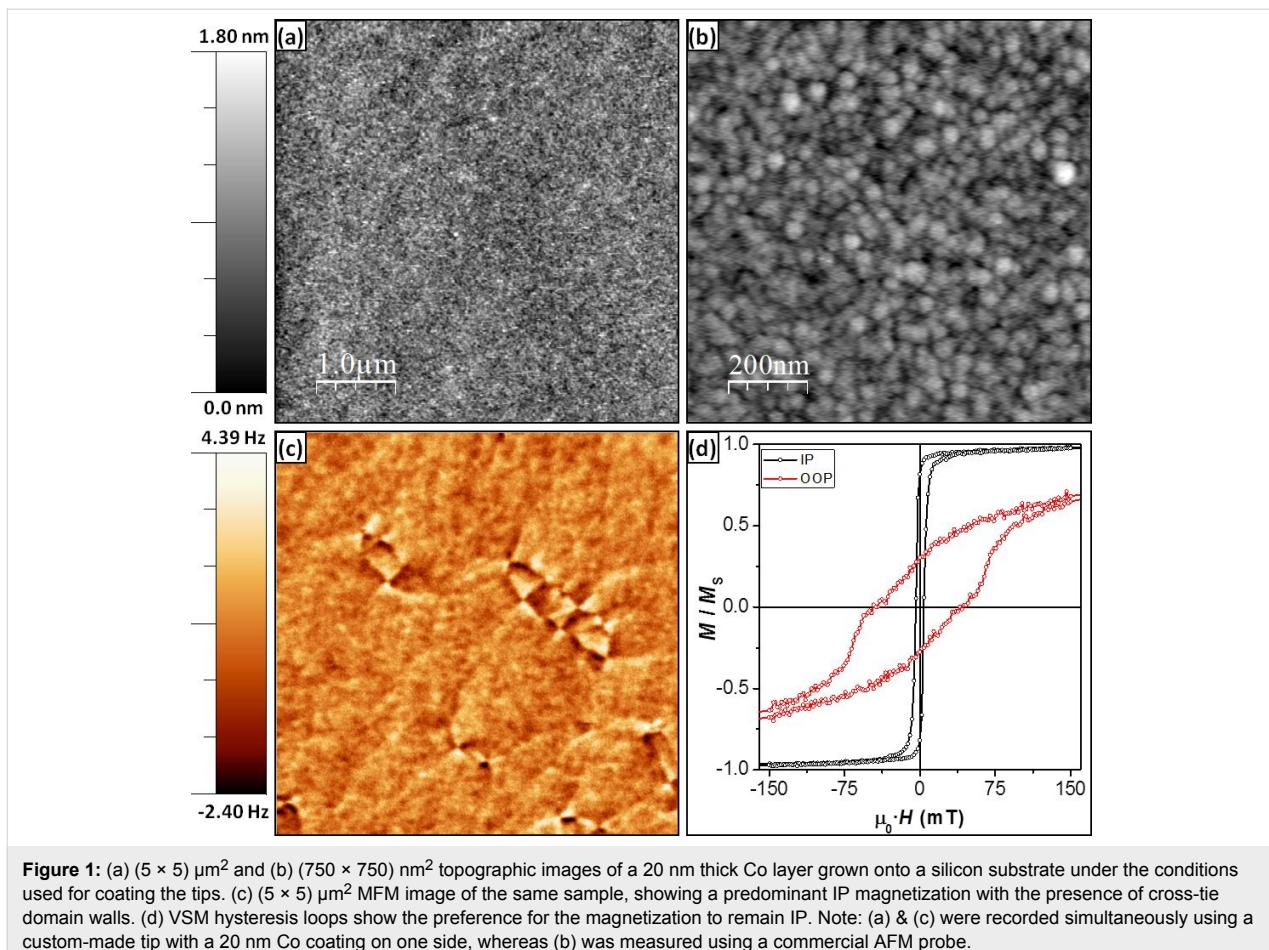
Experimental

The custom-made tips presented in this manuscript are fabricated by sputter coating commercial AFM sensors with a polycrystalline Co thin film with no buffer layer, using a custom-built AC magnetron sputtering system with a substrate holder designed on purpose to favour the growth of the magnetic layer on one side of the pyramidal tip. The deposition parameters are carefully chosen to yield highly flat surfaces with small grain size, ensuring higher lateral resolution for the MFM tips [20] (more details on the deposition parameters can be found in section 1 of Supporting Information File 1).

Even though sputtering is not a highly directional technique, there is a preferential direction of deposition. Thus, by selecting a specific incidence angle, it is possible to cover mainly one side of the tip pyramid. A residual magnetic film with sub-nanometre thickness was found on the remaining parts of the tip–cantilever system. No capping layer is subsequently deposited onto the Co film since, although the outermost atomic layers of cobalt are well known to oxidize under ambient conditions, this affects a very superficial region of the coating of around 2 nm [21]. This oxide layer does not avoid obtaining good MFM imaging results even several months after deposition, with no measured loss of sensitivity and one then avoids the undesired increase in the tip radius caused by the capping material. Magnetic layers of different thickness can be deposited depending on the characteristics of the sample under study. For clarity, we focus here on tips yielding an optimal balance between sensitivity and lateral resolution that can be used with a broad range of samples, having a nominal Co layer of either 20 or 25 nm. Single crystalline silicon substrates were placed close to the AFM tips during deposition and used as reference samples for vibrating sample magnetometry (VSM) and AFM/MFM characterization. In all the experiments shown hereafter MFM data correspond to the shift in the resonance frequency of the cantilever recorded during the retrace scan (withdrawing the sample by 10–20 nm from the topographic set point distance) by using a phase locked-loop (PLL) feedback.

The topography and the magnetic properties of the reference Co/Si sample are shown in Figure 1a–c. On the one hand, a resulting flat surface with a root mean square (RMS) roughness of (0.25 ± 0.05) nm is obtained. The mean grain size, extracted through the self-correlation function along the fast scan direction in Figure 1b, is around 20 nm (notice that such value is an overestimation due to the tip–sample convolution effect). Both parameters were not found to change in great measure for the thickness range used to coat the AFM sensors. On the other hand, the MFM analysis demonstrates that the easy axis of this thin film remains mainly in-plane (IP) due to the influence of the dominating shape anisotropy (as deduced from the cross-tie domain walls [22] seen in Figure 1c), in agreement with the macroscopic hysteresis loops measured at room temperature by VSM (Figure 1d). A high remanent magnetization of 82% of the saturation value is found when an IP field is applied. This, together with the shape anisotropy induced by the pyramidal tip,

Figure 1: (a) (5 × 5) µm² and (b) (750 × 750) nm² topographic images of a 20 nm thick Co layer grown onto a silicon substrate under the conditions used for coating the tips. (c) (5 × 5) µm² MFM image of the same sample, showing a predominant IP magnetization with the presence of cross-tie domain walls. (d) VSM hysteresis loops show the preference for the magnetization to remain IP. Note: (a) & (c) were recorded simultaneously using a custom-made tip with a 20 nm Co coating on one side, whereas (b) was measured using a commercial AFM probe.

forces the magnetic moments to remain mainly oriented along the pyramid surface. Nevertheless, the orientation of the spins at the apex will depend on the apex shape and on the way the cobalt layer covers it.

Results and Discussion
Magnetization reversal process of the custom-made probes

A non-conventional MFM-based method previously reported [23] was used to measure local hysteresis loops of the MFM probes [24,25] (see section 2 of Supporting Information File 1 for more details). This approach allows for measuring the magnetostatic tip–sample interaction as a function of the magnetic field. By assuming that the sample magnetization remains unchanged during the experiment ($H_c \gg H_{applied}$), as is commonly assumed to be the case for magnetic hard disks, one can gain insight into the evolution of the spins at the tip apex with the external field and extract the intrinsic hysteresis loop of the MFM tip [25]. Typically, a large Barkhausen jump is observed with a well-defined switching field. By doing so, the measured average switching field for the 20 nm Co homemade tip is $\mu_0 \cdot \langle H_{switch} \rangle = (31 \pm 4)$ mT, where a total of 30 experiments

was performed including three different custom-made probes. This value is within the range of those obtained for commercial probes [24] and allows for reliable MFM measurements in a wide range of applied fields.
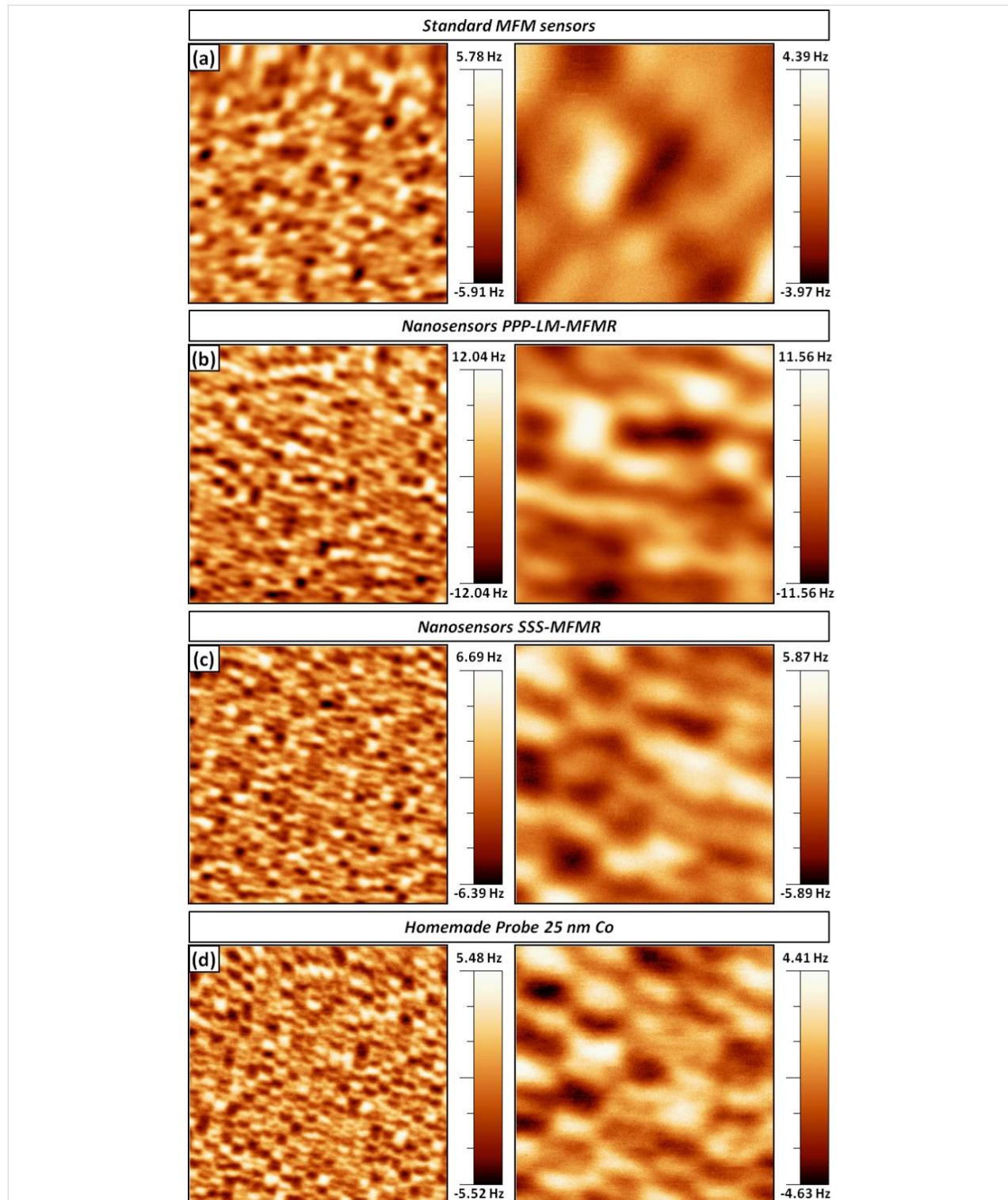
Additionally, the tip radius of the homemade probes was evaluated before and after deposition of the magnetic coating by imaging of a reference sample with carbon nanotubes. Refer to section 3 of Supporting Information File 1 for further detail.

Sensitivity and lateral resolution of the custom-made probes

In order to evaluate the lateral resolution of the probes coated on one side, we present a comparison of the MFM images obtained with four different sorts of probes: three kinds of commercial tips [26,27] and the custom-made probes described here, all of them using cantilevers of similar properties (namely resonance frequency and spring constant of around 75 kHz and 3 N/m, respectively). For these experiments, a high density hard disk with perpendicular anisotropy was used, based on a CoCrPt alloy and courtesy of Toshiba. The domain size is approximately 25 nm.

Three pristine probes of each type were chosen and standard MFM images were measured with analogous parameters (oscillation amplitude ≈ 14 nm, retrace distance from the topographic set point ≈ 15 nm); the best results obtained for each set are shown in Figure 2. The first kind of probes is a standard model with a nominal resolution of about 50 nm, thus being suitable to

Figure 2: MFM images performed to show the lateral resolution obtained with commercial (a) standard, (b) low-moment and (c) super sharp probes and (d) custom-made tips with a 25 nm thick Co coating on the front sides. Images on the left/right columns are (2 × 2) µm^2/(500 × 500) nm^2, respectively.

characterize domains hundreds of nanometers in size or for testing experiments. The second type (low moment probes) is meant for relatively soft samples and has a nominal resolution of 35 nm, showing an improved performance as compared to the previous ones. The third option is the so-called super-sharp MFM tips, which are specific for performing high resolution magnetic force microscopy measurements (with a nominal resolution of 25 nm). These tips with high aspect ratio are particularly suitable for single-pass non-contact MFM [28], a mode that becomes particularly useful when measuring soft magnetic samples with very flat surfaces under ultra-high-vacuum (UHV) conditions, as it prevents the tip from tapping the sample surface and helps preserving its sharpness.
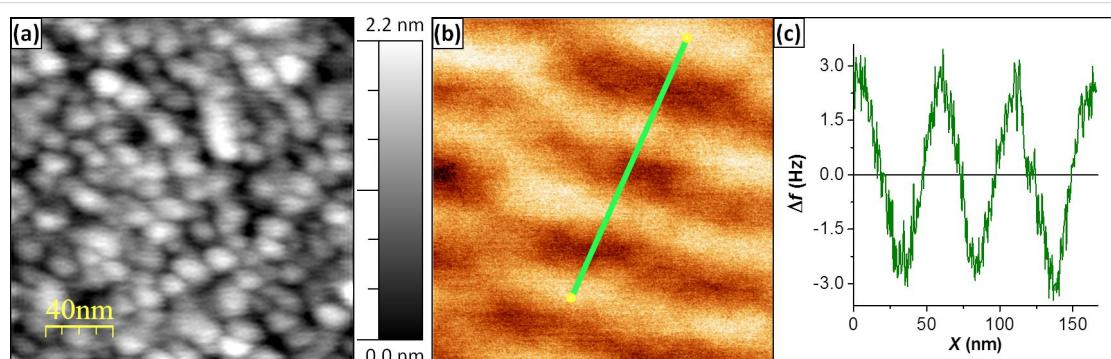
In the last row, data from a custom-made probe with a one-sided Co coating of 25 nm are shown. Having a look at the column on the left, where (2×2) μm^2 images are displayed, an intrinsic lower resolution of the first two types of commercial probes is readily deduced. On the contrary, the super-sharp and the custom-made tips seem to have comparable performances. The difference to the two first kinds of tips becomes even more evident when the image size is decreased down to (500×500) nm^2, as seen on the right column. In the first case, only large domains –composed of large series of neighbouring domains with parallel magnetization– are resolved (Figure 2a). Using low-moment MFM tips, quite better results are obtained (Figure 2b) but the lateral resolution is far from being enough to resolve individual domains. In agreement with its label name, the super-sharp tips yield the best resolved images of all commercial probes (Figure 2c). Nevertheless, at least as good results are obtained with the custom-made sensors, as observed in Figure 2d.

Depending on the sample one might need to even further increase the lateral resolution. This could be achieved by reducing the thickness deposited onto the AFM tips at the expense of reducing their magnetic sensitivity. Figure 3 displays the topography and MFM image of a different region of the same hard disk obtained by a custom-made tip with a 20 nm thick coating. Figure 3a shows grains of the order of 10 nm in size, a remarkable resolution even for non-magnetic AFM probes. The corresponding MFM image shows series of bright and dark stains associated to domains with alternate OOP magnetization (Figure 3b). The frequency shift along the profile drawn is displayed in Figure 3c and confirms the inter-domain distance to be around 25 nm. Note that no smoothing has been applied to the profile data.

In addition to the standard cantilevers typically used to perform MFM imaging, probes with non-standard mechanical properties were prepared to give a glimpse of the potential applicability that can be explored with customized MFM probes. Examples of MFM tips mounted on hard ($k \approx 40$ N/m) cantilevers, commonly used for imaging in vacuum, and soft ($k \approx 0.09$ N/m) levers, used to map soft biological samples, are given in the section 4 of Supporting Information File 1. Please refer there for further information.

The smaller amount of magnetic material deposited onto the tips shown here make them intrinsically excellent candidates for MFM imaging of soft samples. By using the method described in [24] and [29] –in which the magnetostatic influence exerted on an array of single-domain nickel nanowires embedded in an Al_2O_3 membrane was used to calibrate the stray field of the MFM tip– we can estimate the value of the stray field emerging from the custom-coated tips and compare it to the stray field of commercial tips. The axial field estimated for a custom-coated tip with a 25 nm cobalt thickness is less than 25 mT. This value is smaller than any of those reported for different commercial models, making the tips reported here optimal for imaging of soft samples. Finally, similar stray fields than those measured for standard commercial probes can be obtained by depositing


Figure 3: (a) Topography of a high-density HDD, recorded with a custom-made tip with 20 nm coating. The lateral resolution is below 10 nm. (b) Corresponding MFM image showing single domains with alternating OOP orientations. (c) Frequency shift profile along the line shown in (b) that gives an inter-domain distance of about 25 nm.

thicker films (ca. 70 nm). The in-plane (IP) component of the MFM probes can also be relevant depending on the domain structure, a good example of which is the vortex configuration. Again, lower IP field values are attributed to the custom-coated probes [18,20].

Conclusion

In this work we describe an accessible route for customizing MFM probes to desire by coating one side of standard AFM tips using sputtering. We demonstrate that the resulting probes achieve lateral resolutions at least as good as commercial super-sharp tips (10 nm and 25 nm in topographic and MFM images, respectively). A particular advantage is the possibility of coating tips mounted on hard ($k \approx 40$ N/m)/soft ($k \approx 0.09$ N/m) cantilevers to optimize imaging in vacuum/liquid environments, providing enhanced sensitivity compared to standard probes.

Supporting Information

Supporting Information File 1

Additional experimental data.
[http://www.beilstein-journals.org/bjnano/content/supplementary/2190-4286-7-100-S1.pdf]

Acknowledgements

References

1. Phillips, G. N.; Siekman, M.; Abelmann, L.; Lodder, J. C. *Appl. Phys. Lett.* **2002,** *81,* 865–867. doi:10.1063/1.1497434
2. Gao, L.; Yue, L. P.; Yokata, T.; Skomski, R.; Liou, S. H.; Takahoshi, H.; Saito, H.; Ishio, S. *IEEE Trans. Magn.* **2004,** *40,* 2194–2196. doi:10.1109/TMAG.2004.829173
3. Skidmore, G. D.; Dahlberg, E. D. *Appl. Phys. Lett.* **1997,** *71,* 3293–3295. doi:10.1063/1.120316
4. Lau, Y. M.; Chee, P. C.; Thong, J. T. L.; Ng, V. *J. Vac. Sci. Technol., A* **2002,** *20,* 1295–1302. doi:10.1116/1.1481040
5. Champagne, A. R.; Couture, A. J.; Kuemmeth, F.; Ralph, D. C. *Appl. Phys. Lett.* **2003,** *82,* 1111–1113. doi:10.1063/1.1554483
6. Yoshida, N.; Yasutake, M.; Arie, T.; Akita, S.; Nakayama, Y. *Jpn. J. Appl. Phys.* **2002,** *141,* 5013–5019. doi:10.1143/JJAP.41.5013
7. Kuramochi, H.; Uzumaki, T.; Yasutake, M.; Tanaka, A.; Akinaga, H.; Yokohama, H. *Nanotechnology* **2005,** *16,* 24–27. doi:10.1088/0957-4484/16/1/006
8. Winkler, A.; Mühl, T.; Menzel, S.; Kozhuharova-Koseva, R.; Hampel, S.; Leonhardt, A.; Büchner, B. *J. Appl. Phys.* **2006,** *99,* 104905. doi:10.1063/1.2195879
9. Deng, Z.; Yenilmez, E.; Leu, J.; Hoffman, J. E.; Straver, E. W. J.; Dai, H.; Moler, K. A. *Appl. Phys. Lett.* **2004,** *85,* 6263–6265. doi:10.1063/1.1842374
10. Song, W. Y.; Jung, K. Y.; O, B.-H.; Park, B. C. *Rev. Sci. Instrum.* **2005,** *76,* 025107. doi:10.1063/1.1852312
11. García-Martín, J. M.; Thiaville, A.; Miltat, J.; Okuno, T.; Vila, L.; Piraux, L. *J. Phys. D: Appl. Phys.* **2004,** *37,* 965–972. doi:10.1088/0022-3727/37/7/001
12. Chen, I-C.; Chen, L. H.; Gapin, A.; Jin, S.; Yuan, L.; Liou, S.-H. *Nanotechnology* **2008,** *19,* 075501. doi:10.1088/0957-4484/19/7/075501
13. Campanella, H.; Jaafar, M.; Llobet, J.; Esteve, J.; Vázquez, M.; Asenjo, A.; del Real, R. P.; Plaza, J. A. *Nanotechnology* **2011,** *22,* 505301. doi:10.1088/0957-4484/22/50/505301
14. Amos, N.; Ikkawi, R.; Haddon, R.; Litvinov, D.; Khizroev, S. *Appl. Phys. Lett.* **2008,** *93,* 203116. doi:10.1063/1.3036533
15. Iglesias-Freire, Ó.; Bates, J. R.; Miyahara, Y.; Asenjo, A.; Grütter, P. H. *Appl. Phys. Lett.* **2013,** *102,* 022417. doi:10.1063/1.4776669
16. Schwarz, A.; Wiesendanger, R. *Nano Today* **2008,** *3,* 28–39. doi:10.1016/S1748-0132(08)70013-6
17. Jaafar, M.; Yanes, R.; Perez de Lara, D.; Chubykalo-Fesenko, O.; Asenjo, A.; Gonzalez, E. M.; Anguita, J. V.; Vázquez, M.; Vicent, J. L. *Phys. Rev. B* **2010,** *81,* 054439. doi:10.1103/PhysRevB.81.054439
18. Aliev, F. G.; Dieleman, D.; Awad, A. A.; Asenjo, A.; Iglesias-Freire, O.; García-Hernández, M.; Metlushko, V. Probing ground state in circular magnetic dots: Single vs. double magnetic vortex. In *2010 International Conference on Electromagnetics in Advanced Applications (ICEAA),* Sydney, NSW, Australia, Sept 20–24, 2010; IEEE Publishing: Piscataway, NJ, U.S.A., 2010; pp 160–163. doi:10.1109/ICEAA.2010.5652137
19. Ares, P.; Jaafar, M.; Gil, A.; Gómez-Herrero, J.; Asenjo, A. *Small* **2015,** *11,* 4731–4736. doi:10.1002/smll.201500874
20. Iglesias-Freire, Ó. Advances in Magnetic Force Microscopy. Ph.D. Thesis, Autonomous University of Madrid, Spain, 2014.
21. Rosa, W. O.; Martínez, L.; Jaafar, M.; Asenjo, A.; Vázquez, M. *J. Appl. Phys.* **2009,** *106,* 103906. doi:10.1063/1.3254195
22. Hubert, A.; Schäfer, R. *Magnetic Domains;* Springer: Berlin, Germany, 1998. doi:10.1007/978-3-540-85054-0
23. Jaafar, M.; Serrano-Ramón, L.; Iglesias-Freire, O.; Fernández-Pacheco, A.; Ibarra, M. R.; de Teresa, J. M.; Asenjo, A. *Nanoscale Res. Lett.* **2011,** *6,* 407. doi:10.1186/1556-276X-6-407
24. Jaafar, M.; Asenjo, A.; Vázquez, M. *IEEE Trans. Nanotechnol.* **2008,** *7,* 245–250. doi:10.1109/TNANO.2008.917785
25. Jaafar, M.; Gómez-Herrero, J.; Gil, A.; Ares, P.; Vázquez, M.; Asenjo, A. *Ultramicroscopy* **2009,** *109,* 693–699. doi:10.1016/j.ultramic.2009.01.007
26. AFM tips, Magnetic Force Microscopy tip. http://www.budgetsensors.com/force_modulation_afm_tip_magnetic.html (accessed Dec 16, 2015).
27. Magnetic Force Microscopy (MFM) – NANOSENSORS. http://www.nanosensors.com/magnetic-force-microscopy-afm-tips (accessed Dec 16, 2015).
28. Schwenk, J.; Marioni, M.; Romer, S.; Joshi, N. R.; Hug, H. J. *Appl. Phys. Lett.* **2014,** *104,* 112412. doi:10.1063/1.4869353
29. Asenjo, A.; Jaafar, M.; Navas, D.; Vázquez, M. *J. Appl. Phys.* **2006,** *100,* 023909. doi:10.1063/1.2221519